Enhancing Diamond-Like Carbon Adhesion on AISI 316L Stainless Steel Using Chromium Nitride Interlayers

A Thesis Submitted to the College of

Graduate and Postdoctoral Studies

In Partial Fulfillment of the Requirements

For the Degree of Master of Science

In the Department of Mechanical Engineering

University of Saskatchewan

Saskatoon

By

Muhammad Irtaza Khan

PERMISSION TO USE

In presenting this thesis in partial fulfillment of the requirements for a postgraduate degree from the University of Saskatchewan, I agree that the Libraries of this University may make it freely available for inspection. I further agree that permission for copying of this thesis in any manner, in whole or in part, for scholarly purposes may be granted by the professor who supervised my thesis work or, in their absence, by the Head of the Department or the Dean of the College in which my thesis work was done. It is understood that any copying or publication or use of this thesis or parts thereof for financial gain shall not be allowed without my written permission. It is also understood that due recognition shall be given to me and to the University of Saskatchewan in any scholarly use which may be made of any material in my thesis.

Requests for permission to copy or to make other uses of materials in this thesis/dissertation in whole or part should be addressed to:

Head of the Department of Mechanical Engineering
57 Campus Drive,
University of Saskatchewan
Saskatoon, Saskatchewan, S7N 5A9 Canada

OR

Dean
College of Graduate and Postdoctoral Studies
University of Saskatchewan
116 Thorvaldson Building, 110 Science Place
Saskatoon, Saskatchewan S7N 5C9 Canada

ABSTRACT

Energy losses in moving components due to high friction and wear are one of the biggest challenges faced by industries. AISI 316L stainless steel (SS) is one of the most widely used alloyed steel for moving parts in corrosive environments. However, its poor tribological properties result in limited longevity and performance. As lubrication is not an option for food processing and biomedical devices, surface modification of the SS is usually required. Nitriding and carburizing can enhance its wear resistance but result in a high coefficient of friction (COF) and poor corrosion resistance. Coating Diamond-like carbon (DLC) films are very promising to lower its COF and increase its wear and corrosion resistance as well as biocompatibility. However, the application has been limited due to its poor adhesion to SS substrates.

The present thesis work aims to use a chromium nitride (CrN) thin film as an interlayer to enhance DLC adhesion on the SS substrate. CrN thin films with various microstructures and thicknesses were first deposited onto the SS substrate using radio frequency magnetron sputtering under different deposition conditions. DLC coatings were then deposited on the CrN interlayered SS substrates using ion beam deposition (IBD). The deposited CrN interlayers and DLC coatings were then characterized by various techniques including grazing incidence X-ray diffraction, Raman spectroscopy, X-ray photoelectron spectroscopy (XPS), field emission scanning electron microscopy, optical profilometry, nanoindentation, Rockwell C indentation, and ball-on-disc tribological testing.

The results show that the microstructure and the corresponding mechanical properties of the sputtered CrN thin films can be tailored by changing deposition parameters. CrN films deposited at 470 °C and 10 mTorr pressure had a dense, net-like structure with a hardness of 8 GPa, and significantly enhanced DLC adhesion on the steel. The interlayer, deposited with a thickness ranging from 0.4 to 2.1 µm, was found to play an important role in improving DLC adhesion. The thicker the interlayer, the better the adhesion. Furthermore, good DLC adhesion on the steel was achieved by doping DLC with nitrogen at a thinner CrN interlayer of 1.1 µm because of the reduced intrinsic stress in nitrogen doped DLC coatings. Finally, wear testing results showed that DLC coating can decrease COF and wear rate of the steel when sliding with AISI 302 ball.

ACKNOWLEDGMENTS

I would like to express my deepest appreciation to my supervisor, Professor Qiaoqin Yang, for her irreplaceable guidance and support throughout my graduate studies. I will be always grateful.

I would also like to express my sincere gratitude to my committee members, Professor Akindele G. Odeshi and Professor Ikechukwuka N. Oguocha, for their invaluable suggestions. I am grateful to Mr. Zhao Nanfang and Mr. Robert Peace for their assistance.

Special thanks to Dr. Jason Maley, Dr. Jianfeng Zhu and Dr. Danielle Covelli, Saskatchewan Structural Sciences Center (SSSC), and Dr. Eiko Kawamura, Western College of Veterinary Medicine (WCVM Imaging Centre), for their technical assistance in coatings characterization. I am also grateful to my colleagues Masoud Mohammadthari, Sheida Shiri and Jesus Corona Gomez for their support and advice.

Finally, the financial support provided by the Natural Sciences and Engineering Research Council of Canada (NSERC), Canada Foundation for Innovation (CFI) and the University of Saskatchewan is highly appreciated.

DEDICATION

To my parents, Tahira and Hashim, my siblings, Zoya and Ahmad, and to Shifa.

TABLE OF CONTENTS

LIST OF TABLES

LIST OF FIGURES

LIST OF ABBREVIATIONS

a-C:H	Hydrogenated amorphous carbon
AISI	American iron and steel institute
BWF	Breit-Wigner-Fano
COF	Coefficient of friction
CrC	Chromium carbide
CrN	Chromium nitride
CVD	Chemical vapor deposition
d	Lattice spacing
DC	Direct current
DLC	Diamond-like carbon
E	Young's modulus
E*	Effective elastic modulus
E_b	Binding energy
E_B	Binding energy
E_d	Displacement threshold
EDS	Energy-dispersive X-ray spectroscopy
E_f	Film elastic modulus
E-H	End-Hall
E_k	Kinetic energy
E_p	Penetration threshold
F	Total load
fcc	Face-centered cubic
FCVA	Filtered cathodic vacuum arc
FESEM	Field emission scanning electron microscope
GIXRD	Grazing incident X-ray diffraction
H	Hardness
h_f	Film thickness
h_{max}	Maximum indent
h_p	Plastic deformation

$h\upsilon$	Photon energy
HV	Vickers pyramid number
IBD	Ion beam deposition
ISE	Indentation size effect
K	Wear rate
L_{max}	Maximum load
MSIB	Mass selected ion beam
NDLC	Nitrogen-doped DLC
PECVD	Plasma enhanced chemical vapor deposition
PLD	Pulsed laser deposition
PVD	Physical vapor deposition
RF	Radio frequency
RMS	Root mean squared
S	Total sliding distance
SS	Stainless Steel
SZM	Structural zone model
ta-C	Tetragonal amorphous carbon
T_m	Target melting temperature
T_s	Substrate temperature
UMT	Universal machine testing
V	Wear volume
VDI	Verein Deutscher Ingenieure
XPS	X-ray photoelectron spectroscopy
XRD	X-ray diffraction
γ	Surface fracture energy
σ_f	Compressive stress
ω	Incident angle
λ	Wavelength
ν	Poisson's ratio

CHAPTER 1
INTRODUCTION

1.1 Motivation

Industries, of any kind, involve complex mechanical systems with moving components. The study of contacting surfaces in relative motion is called tribology, a term first introduced by Jost in 1966 [1]. According to a study by Holmberg, tribological contacts alone results in consumption of about 23% (119 EJ) of the world's total energy [2]. In another study by Lee and Carpick, the significance of understanding tribology and surface modification was identified that could result in saving of 20 EJ (2.1% of the gross national product-GNP) of energy annually [3]. Chemical and petrochemical industry is the biggest energy consumer and together with the iron and steel industry, they account for half of the total energy consumed in the industrial sector [2,4]. Although the energy consumption is higher due to friction, wear is more crucial, for it results in operational breakdowns and catastrophic failures that not only impacts the productivity but also results in human loss [5].

AISI 316L stainless steel (SS) is one of the most widely used alloyed steel and has been widely used in petrochemical, food processing, off-shore, power generation, and mining industries because of its superior corrosion resistance and high mechanical strength [6-8]. Its corrosion resistance originates from the formation of an adherent and self-healing passive film on its surface in corrosive environments [9-12]. In addition, because of its proven biocompatibility [13], it has been also widely used in biomedical implants [14,15]. However, its low hardness and poor tribological properties limit its longevity and durability as moving parts in equipment [16,17]. Especially, the wear rate of the SS is quite high when subjected to both corrosive and erosive conditions, such as slurry pumps and valves in chemical plants [18], which results in the complete removal of the protective passive film from the surfaces under contact and thus accelerates material dissolution and increases wear.

To solve this problem of friction and wear, over the past few decades, several surface modification techniques have been employed. Thermal diffusion processes including nitriding, carburizing, carbonitriding and boriding are the most common techniques used to enhance the surface properties to reduce wear losses [19-24]. However, thermal diffusion processes are slow, which

requires extended period which may be up to a day to achieve the desired thickness, with attendant drawbacks of high coefficient of friction (COF) and reduced corrosion resistance.

Surface coatings, however, have proved to be a promising solution to address the problem. It involves adding a thin layer of another material with desired properties. The layer is usually deposited by a physical or a chemical vapor deposition technique [25].

Diamond-like carbon (DLC) coatings are the focus of many studies because of their high hardness, low COF, excellent biocompatibility, and high wear and corrosion resistance [26-29]. However, DLC has poor adhesion on steel substrates which limits its use. Researchers have concluded that the huge mismatch in mechanical properties and the lack of chemical interaction between the substrate and the thin films are responsible for the failure [30-32]. To overcome this problem, researchers have tried surface treatments like surface nitriding and carburizing to modify the surface properties of the steel prior to DLC deposition. However, this method has not been successful because of the reduced corrosion resistance of the steel substrate due to the formation of unstable chromium nitride and carbide precipitates during surface nitriding and carburizing, respectively [33-35]. Employing metallic and ceramic interlayers is another approach to increase DLC adhesion to the steel substrate.

In this study, chromium nitride (CrN) was chosen as an interlayer to enhance DLC adhesion to AISI 316L SS. CrN thin films have superior wear and corrosion resistant properties with mechanical properties in between that of hard DLC and SS [36-39]. Furthermore, it can have a net-like structure to interlock with DLC coatings.

1.2 Objectives

The overall objective of the present work is to develop an appropriate CrN interlayer to achieve high adhesion of DLC onto AISI 316L SS substrate. To accomplish the desired goal, the following specific objectives were established:

1. Investigate the effect of deposition parameters on the microstructure and mechanical properties of CrN thin films.

2. Develop a CrN interlayer with appropriate microstructure and thickness to make DLC adherent to the steel substrate.
3. Investigate the adhesion of nitrogen doped DLC (NDLC) on the steel with CrN as an interlayer.
4. Evaluate the mechanical and tribological properties of DLC-coated SS samples.

1.3 Thesis Organization

In chapter 1 the motivation for the present research work is covered and the objectives to accomplish the desired goal were defined.

In chapter 2 a comprehensive review of AISI 316L SS, DLC and CrN thin films is given. In this chapter, I have summarized the approaches previously applied to improve the wear resistance of the SS 316L and their limitations and explains the advantages of using DLC films. The deposition and characterization techniques for DLC and CrN thin films are also described.

Chapter 3 is about the experimental techniques and deposition parameters used for DLC and CrN thin film deposition and their characterization techniques.

In Chapter 4 I have presented the results of the performed experiments and discussed the reasons responsible for those results. The chapter is divided into four sections. The first section is on the effect of deposition parameters on the properties of CrN thin films, the second one is about the DLC adhesion on these CrN interlayers, the third one shows the effect of CrN interlayer thickness on the adhesion of DLC and NDLC coatings, and the fourth section reports the tribological results of the bare SS and coated SS.

Finally, I conclude with the results presented in previous chapters and gives recommendations for future work on this topic in Chapter 5.

CHAPTER 2
LITERATURE REVIEW

2.1 Overview of AISI 316L Stainless Steel (SS 316L)

Before a stainless steel (SS) is selected as a material for a particular application in industry, it is assessed based on its mechanical properties, corrosion resistance, fabricability, and cost. Material selection for mechanical equipment like pumps, bearings, valves, and seals, however, require additional tribological properties, e.g. high wear resistance and low COF, as in these equipment the metal surfaces rub against each other. Materials for pharmaceutical and food processing and biomedical implants would be more challenging where the materials in moving contact not only face wear and corrosion but also require biocompatibility and limited use of lubricants [40].

SS 316L is an iron-based alloy which has a face-centered cubic structure and is formed by alloying with Ni, Mn, and N as austenizing elements. The alloy is usually formulated with low carbon to avoid chromium carbide formation, which results in depletion of chromium from the austenite matrix and reduces corrosion resistance [41]. The 'L' in AISI 316L represents low carbon and makes it different from the standard AISI 316. Table 2.1 shows its composition and Table 2.2 shows the selected properties of the 316L SS used in this work, which was provided by McMaster-Carr®.

Table 2.1. Composition of AISI 316L stainless steel [McMaster-Carr®].

Grade		Fe	C	Cr	Ni	Mn	Cu	Mo	P	S	Ti
AISI 316L	Min %	58.23	-	16	10	-	-	-	-	-	-
	Max %	73.61	0.08	18.5	15	2	1	3	0.045	0.35	0.7

Table 2.2. Properties of AISI 316L stainless steel [McMaster-Carr®].

Property	Value
Yield Strength	206.8 MPa
Hardness	Rockwell B95 (Medium)
Heat treatable	No
Maximum temperature	815.5 °C (1500° F)
Specifications met	ASTM A240, MIL-S-5059
Density	0.29 lbs./cu. in.
Melting point temperature	1371 °C (2500° F)
Modulus of elasticity	193 GPa
Thermal conductivity	110 Btu/hr. × in./sq. ft./°F @ 212° F
Elongation	39%

AISI 316L SS has been widely used in highly corrosive environments ranging from chemical, fertilizer to food processing, petrochemical, and power generation industries. The steel components in these industries are subjected to abrasion, erosion, scratching and other forms of wear damages in a corrosive environment. Thus, continuous degradation of steel happens because of the passive film removal from the surface due to accelerated wear [42]. This material is known well for its superior corrosion resistance and mechanical properties over other 300 series stainless steels like 304 and 321 [43]. However, this steel grade is relatively soft that makes it susceptible to multiple wears and surface contact damages. This poor tribological performance limits its usage in applications which requires low COF and high wear resistance to avoid unwanted wear induced failures of the equipment.

Since it has an austenitic structure and cannot be hardened by heat treatment [44], it is impossible to improve its wear resistance by heat treatment. This urges us to enhance the surface properties of AISI 316L SS with other methods.

Moreover, 316L SS is one of the most common orthopedic implants material because of its good load-bearing property, high corrosion resistance and low cost [45]. However, the surface degradation due to wear results in the release of chromium and nickel ions, causing potential chronic inflammatory and toxicity, and reduced biocompatibility [46], which requires the steel surface to be modified to obtain desirable surface properties.

One approach to enhance the surface property is surface treatment. Surface treatment accounts for a very broad range of processes that alter the surface of a material to enhance its properties. The most common surface treatments applied include surface melting, carburization, nitriding, carbonitriding and boriding [47-50].

Carburization is usually carried out at a high temperature of 900 °C. Although it can increase the wear resistance by hardening the surface to 380-450 HV [48], the formation of chromium carbides results in the reduction of corrosion resistance [42].

Nitriding is a case hardening process in which nitrogen is introduced into the steel surface in a nitrogen-containing environment at a temperature of 496-566 °C. It results in a compound layer that consists of iron nitrides and chromium nitride. Although nitriding enhances wear resistance by increasing surface hardness, it decreases corrosion resistance by the formation of chromium nitrides. Moreover, due to an elevated temperature in nitriding, the occurrence of carbide precipitation in the steel leads to intergranular corrosion, causing uncertainty in the life of nitrided SS steels in the acidic environment [51]. In addition, the nitrided surface layer is found to be brittle [52] with residual stress [53] and non-homogenous [54] with inconsistency in hardness [55].

Another approach to enhance surface properties is surface coating. A wide range of coatings is available, each owning a unique property. Figure 2.1 shows various coating options with their hardness and COF values. Since hydrogenated DLC coatings show low COF and high wear resistance, it has been chosen for this thesis research. Following sections briefly describes the composition and properties of DLC coatings.

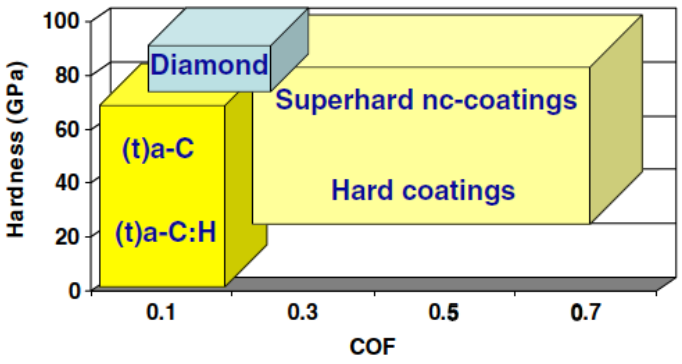

Figure 2.1. A schematic representation of hardness with coefficients of friction (COF) of carbon-based and other hard coatings [31].

2.2 Carbon Materials

Carbon is considered as one of the most remarkable elements for existing in more than 90% of all known chemical materials. It has the biggest number of allotropes that possess exceptional properties that range from the extremely hard diamond to soft and highly lubricative graphite. Apart from these, carbon-based allotropes include carbon nanotubes, fullerenes, carbon nanofibers and glassy carbons [29] as shown in Figure 2.2 [56].

Carbon has four valence electrons in 2s and 2p orbitals and can form different covalent bonds based on different orbital hybridization including *sp*, sp^2, and sp^3. Figure 2.3 shows the electron configuration of the carbon atom and the *sp*, sp^2 and sp^3 hybridization resulting from orbital mixing. When the 2s orbital hybridizes with one 2p orbital, two *sp* orbitals forms, allowing the formation of triple bonds with other carbons of the same configuration as seen in alkynes. The structure formed is linear with a bond angle of 180°. The linear overlap of hybridized orbitals results in a single σ bond while the remaining two unhybridized orbitals parallelly overlap to form two π bonds.

In sp^2 hybridization, the 2s orbital hybridizes with two 2p orbitals to form three sp^2 orbitals and leaving one $2p_z$ orbital unhybridized. All the 3 sp^2 orbitals lie in the same trigonal plane with an angle of 120° separating them and linearly overlap to form 3 σ bonds. The remaining 2p orbitals parallelly overlap to form a single π bond. This π bond is weaker than the σ bond since there is no

preference in the bonding of $2p_z$ orbital electron with all three neighbours, this electron is freer and results in electric conduction in graphite [57,58].

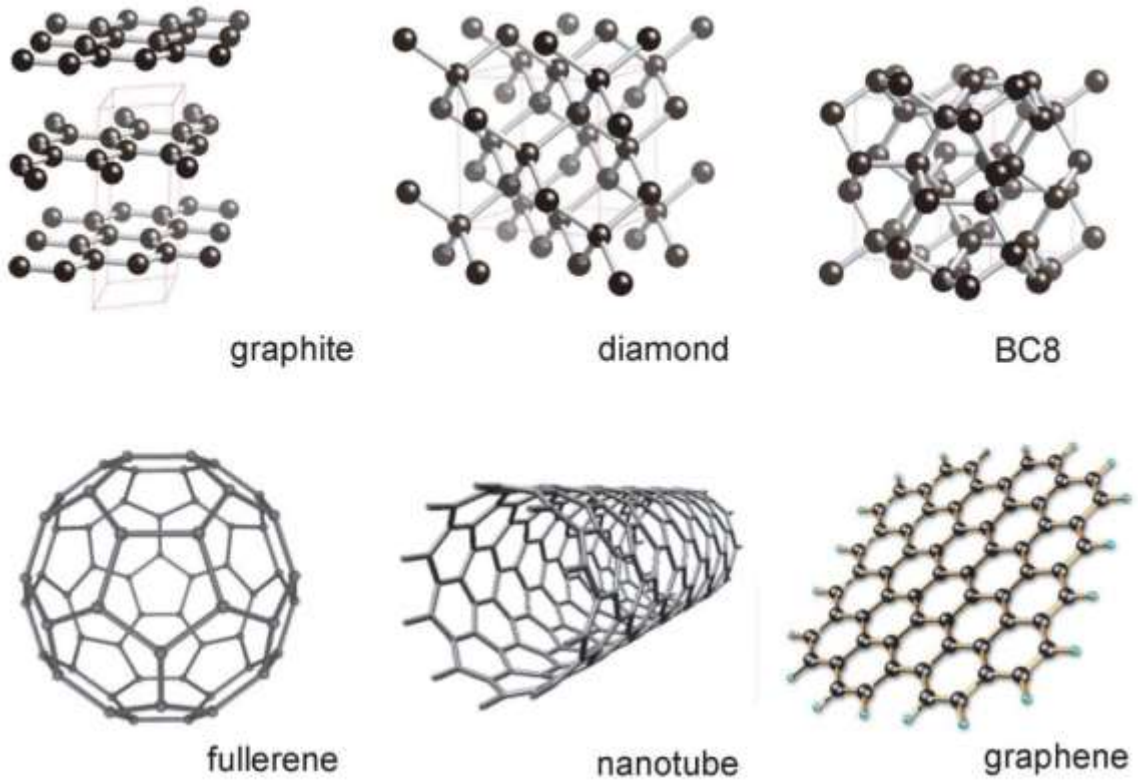

Figure 2.2. Structures of allotropes of carbon [56].

When the 2s orbital hybridizes with all the three 2p orbitals, four sp^3 orbitals with a tetrahedral geometry form with a bond angle of 109.5°, resulting in σ bonds among adjacent atoms, as in diamond. The σ bonds are extremely strong and account for the super hardness of diamond [59].

The variety in chemical bonds and their combinations result in a variety of different atomic structures with different unique properties. Fullerenes and carbon nanotubes result from sp^2 hybridization of carbon orbitals while diamond results from sp^3 orbitals hybridization. Amorphous carbon, however, consists of a mixture of σ and π bonds resulting from both sp^2 and sp^3 orbitals hybridization and is characterized based on the relative percentages of the two different bonds [29].

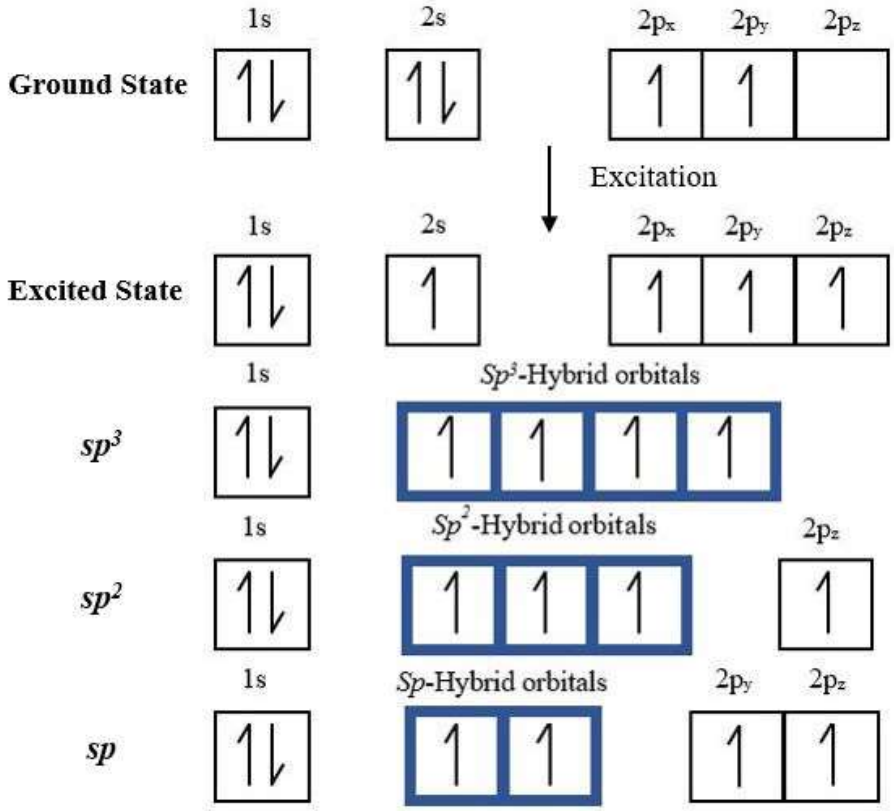

Figure 2.3. Carbon electronic configuration and sp^3, sp^2, sp^1 hybridization

2.3 Diamond-Like Carbon Coatings

Diamond-like-carbon (DLC) materials are amorphous composed of a combination of both sp^2 and sp^3 hybridized carbon atoms with a high percentage of sp^3 hybridized bonds. Their properties are like those of diamond although they are a function of the relative percentage of sp^2 (graphite-like) and sp^3 (diamond-like) bonds present [60]. The general term "DLC" is used to define them and accounts for both hydrogenated and hydrogen-free metastable amorphous carbon that is prepared using a wide range of PVD and CVD techniques. It is generally prepared in a process involving energetic ions. The hydrogen content and the relative amount of sp^2 and sp^3 carbon hybridization determine the film structure and properties. Hydrogen in DLC plays important role in stabilizing the random network and preventing the domination of the graphite phase [61].

Figure 2.4 shows the ternary phase diagram for DLC as proposed by Robertson in 1998. The left corner represents amorphous carbon with sp^2 bonding. The right corner is for very high H content

that is in gas or liquid phase because of no formation of the interconnected network. Sputtered amorphous C, dominated by sp^2, and tetragonal amorphous c (ta-C), dominated by sp^3, represents nonhydrogenated films. Hydrogenated a-CH films are, however, the most common type of DLC with a moderate percentage of sp^3 bonds and a high hydrogen content of up to 50 at% [62].

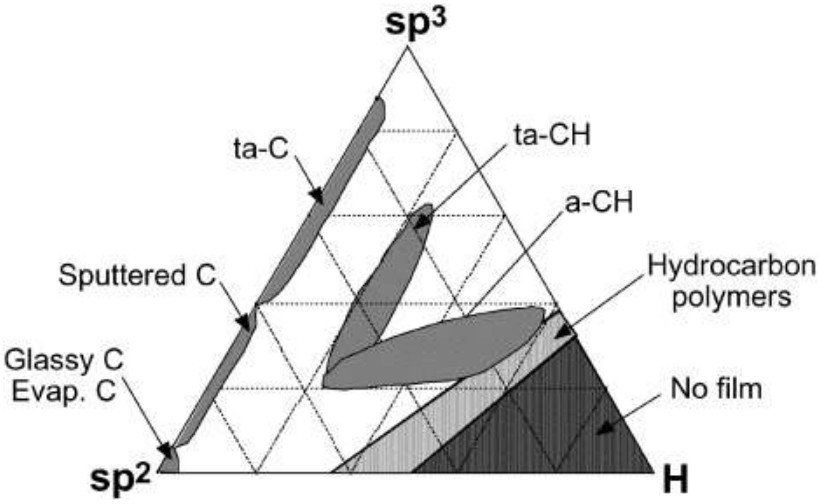

Figure 2.4. Ternary phase diagram for various DLC coatings with respect to their sp^2, sp^3 and hydrogen contents [31].

Diversity in DLC structure and composition has made it possible to tailor the film structure over a wide range to get desired properties according to specific needs and applications. In the present study, hydrogenated DLC was chosen because of its low COF and moderate hardness.

Hardness and stiffness play the most important role in deciding a material's ability to carry a load and to resistant to wear. Generally, materials with high hardness and stiffness values demonstrate high wear resistance. Hydrogenated DLC is composed of C-C sp^3, C=C sp^2, and C-H bonds. Figure 2.5 shows the atomic structure of hydrogenated DLC films [31]. C-C sp^3 bonds are responsible for the 'diamond-like' character in DLC. The mechanical properties of DLC are a function of their relative amount. A high percentage of C-C sp^3 results in high Young's modulus and high hardness of DLC coatings, whereas a high percentage of sp^2 bonds results in low COF due to its lubricative properties.

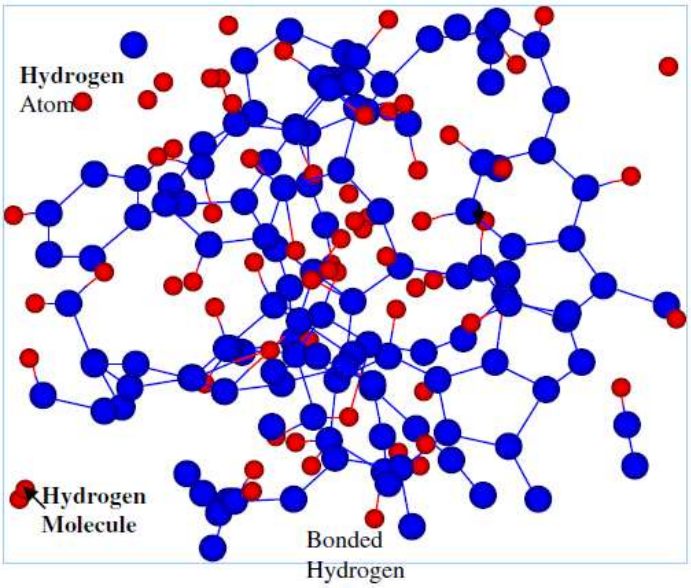

Figure 2.5. Atomic structure of a hydrogenated DLC coatings [31].

2.3.1 Deposition Techniques

Since the first DLC deposition in 1971 by ion beam deposition, DLC coatings can now be deposited at temperatures ranging from sub-zero to 400°C over a broad range of deposition pressure using several kinds of PVD and CVD techniques. The films can be deposited over substrates of all types, however, the ability to demonstrate good adhesion depends on the chemical nature and mechanical bonding involved. Figure 2.6 shows the schematics for some of the widely used plasma-based DLC deposition methods [31]. They include mass selected ion beam (MISB), pulsed laser deposition (PLD), and plasma enhanced vapor deposition.

DLC deposition by sputtering is one of the most widely used industrial technique [60]. It has the advantage of being easy to control over deposition conditions by changing plasma power and gas pressure. In this process depositing carbon atoms is sputtered from a pure carbon target by energetic ions. The energy source can be DC or radio frequency (RF), each having unique advantages. The disadvantage of DLC synthesis using this method is that the DLC synthesized has a high percentage of sp^2 bonds and thus low hardness.

In gas discharge plasmas processes, a hydrocarbon gas (such as methane) is used as a precursor for carbon. In this case, the films produced contain a significant amount of hydrogen.

In an ion beam deposition system, carbon ions are produced either by plasma sputtering of graphite target or by using precursor hydrocarbon gas like methane that is ionized by an ion source. These carbon species are then accelerated in a vacuum chamber in form of an ion beam with high ion energy.

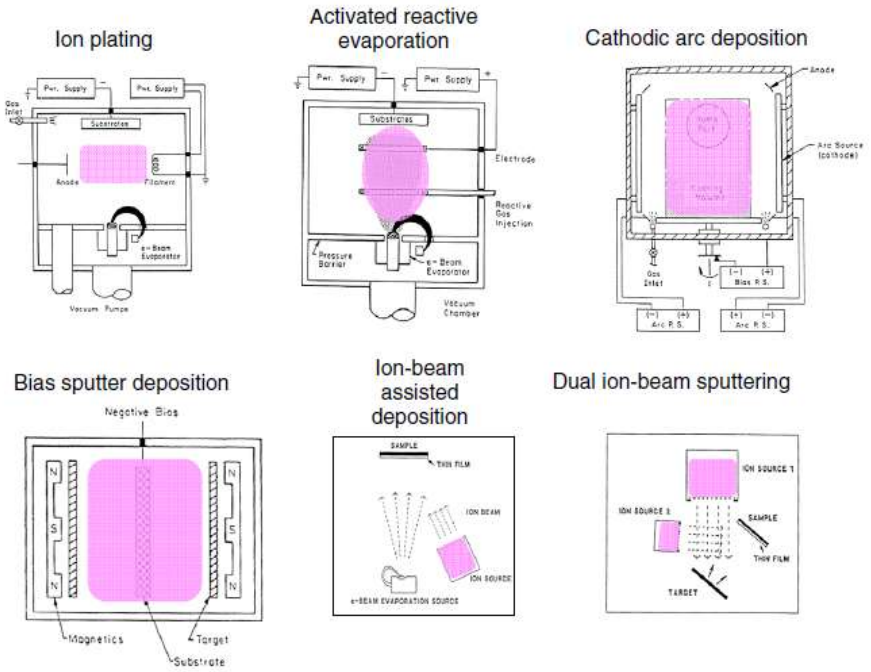

Figure 2.6. Schematic representation of various deposition processes for DLC films deposition [31].

2.3.2 Deposition Mechanism

The sp^3 bond percentage in DLC is a function of ion energy during deposition [62]. It has been observed for both hydrogenated and hydrogen free DLC film deposition that sp^3 bond percentage increases to a maximum value with the increase in ion energy till 100 eV. A further increase in ion energy, sp^2 content increases making the film more graphitic [63, 64]. Moreover, the precursor hydrocarbon molecules used to play an important role in case of a-C:H film depositions. H content in DLC films is lower than the precursor as H is lost during ion bombardment, therefore is again a function of ion energy.

DLC grows by subplantation process. During DLC deposition, the incoming C ion has enough energy to pass the outer substrate layer resulting in a subsurface growth. Therefore, sp^3 content

depends on the ion energy. A lower ion energy prevents subplantation and carbon sticks to the surface as sp^2. Similarly, at very high ion energy the atomic relaxation occurs causing a reduction in sp^3 percentage [65]. In the case of hydrogenated DLC deposition, an additional process of H loss with ion bombardment happens.

Penetration threshold, E_p, is the energy required by the carbon atoms to penetrate the substrate surface. A minimum energy is required by every ion to displace surface atom in order to create a stable vacancy-interstitial pair. This minimum energy is defined by displacement threshold, E_d. Moreover, the binding energy that keeps the surface atoms together is defined as E_b. They are related to each other by the following equation:

$$E_p \sim E_d - E_b \tag{2.1}$$

An ion can never penetrate the substrate surface if it does not possess this energy. For this reason, a high ion energy is required during DLC deposition.

This sub-plantation growth mechanism consists of four stages [66]. Figure 2.7 shows DLC growth by subplantation [67].

1. Carbon implantation in the sub-surface layers.
2. Local stresses induction by high carbon atoms density in sub-surface.
3. Target atoms dilution till the evolution of pure carbon layer.
4. Gradual carbon layer growth due to successive bombardment.

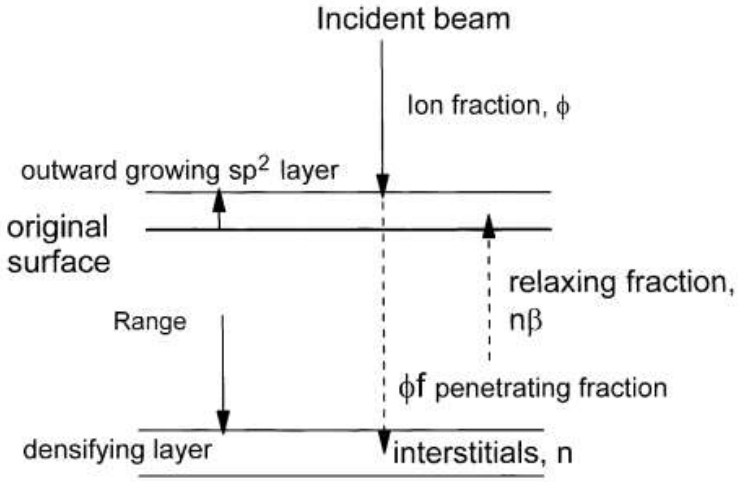

Figure 2.7. Schematic diagram of densification by subplantation [67].

2.3.3 Stresses in DLC Coatings

Stresses in DLC include intrinsic stress, thermal stress, and extrinsic stress. Thermal stress that results from thermal expansion coefficient mismatch between DLC and the substrate; can be eliminated easily by room temperature deposition or by reducing thermal expansion coefficient mismatch using an interlayer [68]. Extrinsic stresses, generated by film interaction with external factors, can be reduced by eliminating impurities like oxygen that leads to lattice deformation and expansion of film volume. Intrinsic stress is further classified as compressive and tensile intrinsic stresses. Voids and vacancies in the films as a result of low energy deposition are responsible for tensile intrinsic stresses [69]. Compressive stress, on the other hand, is induced during DLC deposition due to high energy ion bombardment and increases with the increase of the impact energy per atom [70]. DLC coatings usually have large intrinsic compressive stress and this stress causes delamination in thick coatings [26], making depositing a thick DLC coating a big challenge. Nevertheless, this stress is a function of deposition parameters.

2.4 DLC on 316L Stainless Steel

As previously described, the service life of 316L SS components for many applications is quite low due to their poor tribological performance. Moreover, ion release accompanied with wear degradation in food processing and pharmaceutical industries and biomedical implants demands the steel surface under contact to be coated with a more suitable material. Surface characteristics and tribological performance can be enhanced to a great degree by coating the surface with a material possessing better tribological properties. DLC shows high hardness, extreme smoothness, low COF, and excellent biocompatibility and have attracted the most interest [27]. However, DLC coatings show poor adhesion on steels, which leads to shorter service life as expected. There are several reasons accounting for this poor adhesion: (1) high intrinsic stress in DLC induced during its deposition; (2) lack of chemical or mechanical bonding between the DLC and the steel substrate; and (3) huge mechanical property mismatch between the two materials [71,72]. Figure 2.8 shows the mechanisms involved behind DLC coating failure upon the application of a load.

By hardening the SS substrate surface, the load-bearing capacity of the substrate increases and thus the tribological performance of DLC on the treated SS improves [74].

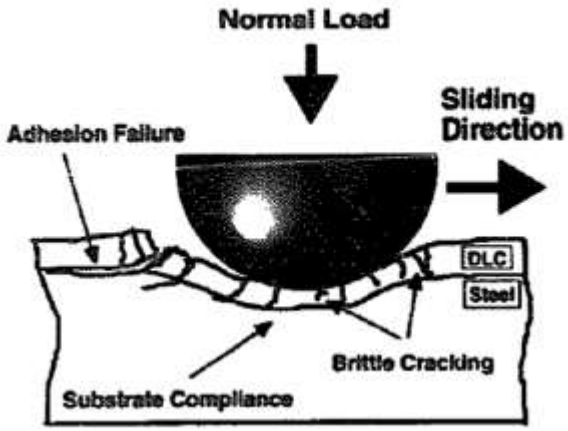

Figure 2.8. The mechanism involved in the failure of DLC films under a high contact load [73].

Boromei coated DLC on a carburized steel and found that the coated steel showed better adhesion because of the increased load-bearing capacity of the carburized steel, and enhanced wear resistance, however, had a higher COF because of the increased roughness due to carburizing [75].

Dalibón deposited a thick soft DLC coating with a hardness of 6 GPa on nitridized 316L SS. The results showed enhanced DLC adhesion and increased wear resistance [76].

Voevodin suggested a multilayered structured coating to enhance DLC adhesion based on the following three concepts [73]:

1) Using an underlayer with mechanical properties varying gradually from the substrate to the DLC that will support the load and increase adhesion.
2) Employing soft interlayers to reduce stress and brake cracks.
3) Allowing dislocation operation for relaxation of stress and cross-sectional crack deflection by using a crystalline interlayer with a sufficient thickness.

Researchers have investigated using interlayers to enhance DLC adhesion to steel substrate [77-80]. Various metallic and ceramic interlayers have proved to be beneficial in DLC adhesion enhancement as they reduce the compressive stress in DLC films and increases the load carrying capacity of the substrate. For example, Chen studied the effect of Cr interlayer on DLC adhesion

enhancement on SS substrate [80]. The Cr interlayer deposited by magnetron sputtering proved to be beneficial because of its similar thermal expansion coefficient with the steel. Moreover, it possesses sufficient toughness to support the DLC film. Nevertheless, the enhancement of adhesion is very limited and only HF3 adhesion has been achieved based on Rockwell C indentation testing.

Chang and Wang used multiple Ti-based interlayers of Ti/TiN/TiCN to increase DLC adhesion on M2 steel and enhanced adhesion has been achieved [81]. Similarly, Silicon-based interlayers have been reported to show increased DLC adhesion on various substrates [82,83]. In these cases, complicated multilayers were used as an interlayer. However, the complex coating system limits its practical use.

In the present study, a single chromium Nitride (CrN) layer is chosen as an interlayer for DLC adhesion enhancement, the results show a high adhesion of DLC on the SS.

2.5 Chromium Nitride

Transition metal nitride coatings, such as titanium nitride and chromium nitride, due to their excellent wear and corrosion resistance are widely used to coat various components to increase their service lifetime resisting tribocorrosion [84-87]. Out of the two, chromium nitride coatings are of special importance because of its superior corrosion resistance [88,89], due to the formation of an oxide passivation layer [90], and a lower COF [91]. Moreover, CrN coatings are less brittle, yet hard, than TiN coatings.

A wide range of deposition methods have been used to deposit CrN coatings including magnetron sputtering, arc ion plating, ion-beam enhanced deposition and e-beam evaporation [92-96]. However, magnetron sputtering is the most widely used method for its deposition because of high deposition rates and high controllability of the deposition.

Deposition parameters like the partial pressure of N_2 during deposition, total working pressure, substrate temperature, and bias greatly affect the chemical composition, microstructure, and stresses in CrN films and consequently the mechanical properties of the coatings. Therefore, the microstructure, thus the properties of the film, can be tailored to be desirable for a specific application by adjusting the deposition parameters.

Lots of researches have been done to investigate the effect of different deposition parameters on the microstructure of CrN coatings in order to understand their relationship.

The effect of nitrogen partial pressure on the chemical composition and the microstructure has been extensively studied. With increasing N_2 flow rate, coating structure evolves from pure cubic Cr to Cr with N interstitial Cr(N) + hexagonal Cr_2N to pure hexagonal Cr_2N to a mixture of Cr_2N + cubic CrN and finally pure fcc-CrN [97-99].

In another study, CrN films were produced over a wide Ar/N_2 ratio. It was noted that low Ar/N_2 ratio resulted in decreased deposition rate due to the target poisoning. Dense films were produced at relatively high deposition temperature [100].

With the same N_2 flow rate, RF sputtered CrN shows higher hardness values compared to DC sputtered CrN. This is because CrN deposited by RF sputtering has a dense structure whereas porous structure forms by DC sputtering. Moreover, CrN coatings showed much better adhesion to the substrate when deposited using RF sputtering [101].

2.5.1 Magnetron Sputtering

Sputtering technique is the most commonly used technique to deposit coatings ranging from pure metals to ceramic coatings, with designs as simple as applying DC diode between the substrate and target. By connecting the substrate to anode and target to the cathode and applying a high voltage, Ar ions are discharged and accelerated towards the target. The sputtered atoms then move through the high vacuum chamber and deposit on the substrate surface. Advantages of sputtering include reasonable deposition rate, ease of sputtering any metal or alloy, high purity of films, high adhesion of the films to the substrate, excellent coverage of small features and steps and uniformity over a large area [102]. DC sputtering has limitations of low deposition rate and high surface temperature; therefore, radio frequency power is used [103].

Magnetron sputtering applies a magnetic field of special shape to diode target. The surface of the cathode is submerged in a magnetic field to create electron traps. These primary and secondary electrons are trapped in a region localized and close to the cathode in an endless racetrack. This results in the increased possibility of an ionizing collision with a gas atom and hence increased ionizing efficiency. The plasma impedance drops and makes it possible to operate the magnetron

source at much lower voltages. The ion current density onto the target also increases resulting in increased erosion of the target.

RF magnetron, operating on high-frequency alternating current, is an alternate to DC magnetron to sputter insulating targets. The operational mechanism of RF magnetron is almost the same as DC magnetron with an additional feature of sputtering insulating materials.

In a sputtering system, together with Ar, any precursor gas can be introduced to react with the sputtered material. This is known as reactive sputtering. The resulting compound is formed on both the surfaces of the target and the substrate. The structure and properties of the growing film can be controlled by controlling the reactive gas flow rate.

Figure 2.9 is a flow diagram summarizing the literature review for a better understanding of the problem addressed and the proposed solution.

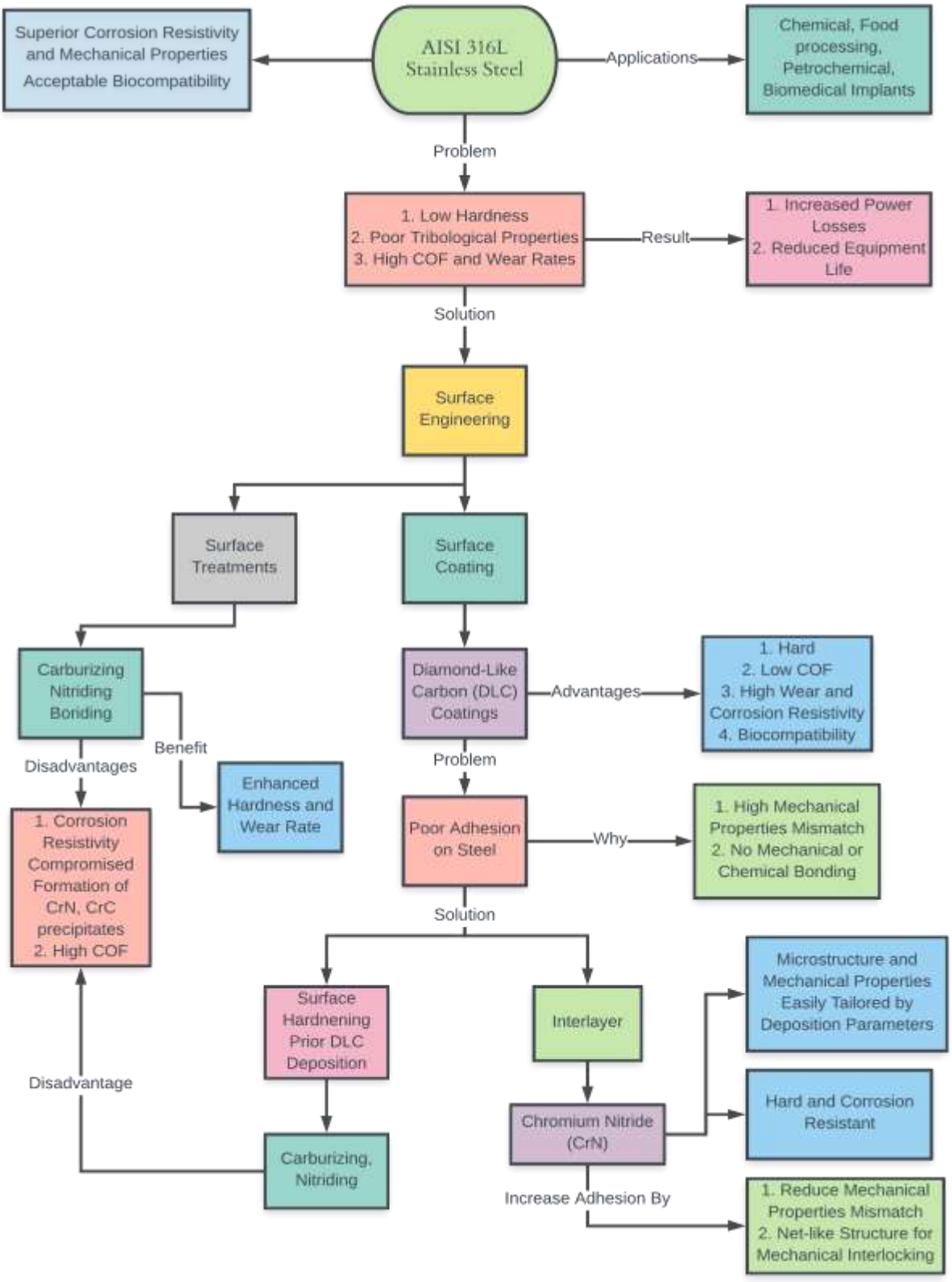

Figure 2.9. Flow diagram summarizing the problem and solution.

2.6 Deposition Parameters and Microstructure

It is important to understand the effect of deposition parameters on the film growth and mechanisms involved in deciding film microstructure, the preferred orientation, and the surface morphology.

2.6.1 The Structural Zone Model (SZM)

For years researchers are trying to understand the influence of different deposition parameters, deposition temperature, working pressure, power, and bias, on the resulting interactions between the target surface and the charged particles, chemical reactions on the substrate and the resulting adherence of deposited material on the substrate surface [104].

The mobility of the adatoms during growth decides the microstructure of the thin films. Different mechanisms, thermal effect, ionic bombarding and chemical reactions at the substrate, are taking place during film growth by sputtering that provide energy to the atoms. A structural zone model (SZM) summarizes the effects of these mechanisms. The microstructure and the resulting morphology of any film can be explained using this SZM. The substrate temperature, working pressure, substrate bias, and the target thermal characteristics are the main parameters of SZM. Normalized temperature is used in this SZM which is the ratio of substrate temperature, T_s, to the melting temperature of the target, T_m [104].

SZM by Movchan is divided into three well-defined zones [105]. Ts/Tm < 0.3 is the first zone. The grains forming the columnar structure in this zone are small and elongated with weak binding and porosity. The structure is a result of low mobile atoms adsorbed by substrate surface with low diffusivity. Moreover, the growth rates of the columns are different, as atoms arrive on the substrate surface from various incidence angles. This is called the atomic shadow effect.

The second zone is defined by $0.3 \leq T_s/T_m \leq 0.45$. Because of the increased substrate temperature, the atom diffusivity increases, resulting in a dense and highly bonded structure. The grain size also increases, and the grain grows from the substrate-film interface to the film surface in equiaxed form.

Finally, the third zone is defined by $T_s/T_m > 0.45$. In this region, the surface morphology is greatly defined by the volumetric diffusion that increases the diffusion into the grains. This results in grain growth and re-crystallization are observed, resulting in a highly crystalline structure.

In addition to these SZM zones, Thorton in 1974, considered the final working pressure effect, that changes the mean free path and the kinetic energy of the ions and added another zone as shown in Figure 2.10 [106]. The final working pressure, therefore, decides the microstructure growth by controlling the adatoms mobility in the surface. In his model, Thorton added a transitional zone, T zone, between the first and second zone. This region is formed by grains with less porosity, resulting in a much dense surface and so smoother surface.

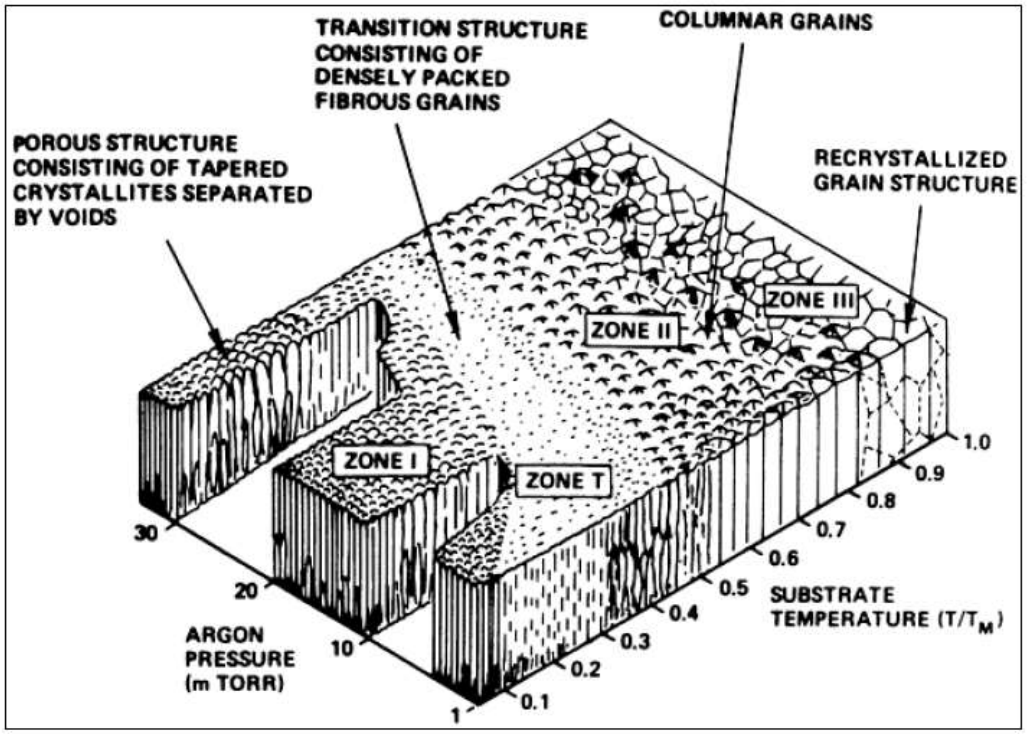

Figure 2.10. Thorton zone model [106].

2.6.2 Growth Models

With too many deposition parameters influencing the growth direction and orientation of the crystalline film, it is very difficult to develop a relationship and thus, an explanation for the preferential crystal growth in metal nitrides. Different models are developed to explain the crystal

growth in a preferential direction includes, kinetic model [107], thermodynamic model [108] and the atomic model [109].

The kinetic model related the preferential growth with the kinetic energies of the ions. The limited mobility of the adatoms results in the film to grow in a particular orientation. This limited mobility can be due to low deposition temperature or due to energy loss and the resulting reduced mean free path. An increase in the adatoms mobility by changing either can result in the changed orientation of the growing film.

The thermodynamic model operates on the thermodynamic equilibrium. The growth orientation is produced at this equilibrium state that is achieved when the substrate-film systems total energy is at the minimum level. Therefore, the preferred orientation is proposed to be determined by the result of a competition between the planes with the least deformation energy, and planes with the least surface energy. Moreover, it was also found that in TiN films, the thickness of the film has no effect on the surface energy, the deformation energy, however, has a direct relation with the thickness [104].

Finally, according to the atomistic model, the thermodynamic parameters are responsible for the preferred orientation in films grown at higher temperatures. The planes with lower energies and with higher diffusivity are more favorable.

2.6.3 Shadowing and Re-emission Effects

Frictional and wear properties of a coating, together with many other important chemical and physical properties, are controlled by the surface morphology of thin-films. This surface morphology can be adjusted by changing the deposition conditions and this requires an understanding of the surface morphology evolution during the film growth [110].

Two dominating processes have been used to understand the film growth. They are shadowing and re-emission [111-116]. Shadowing results in surface roughening while re-emission causes smoothening of the film surface. Atoms arrive on the substrate surface from every different angle and are captured by higher surface points also known as hills, due to the shadowing effect. This results in the formation of columnar structures with rough surfaces. These particles either stick or re-emit based on their kinetic energy or sticking coefficient. The sticking coefficient tells the

degree to which the particle is likely to get stuck to the surface which depends on the complicated physical and chemical processes involved in the particle and the substrate interaction. Moreover, the sticking coefficient is a function of the film deposition parameters like deposition temperature, incident particle energy and the angle of incident flux, and local surface morphology. For example, if the ion energy is too high, re-emission results from a resputtering process that is the knocking off the surface atom by momentum transfer from a highly energetic incident particle followed by the particle redeposition on surface valley [115,116]. Figure 2.11 below shows the shadowing effect and re-emission. Particles sticking to the hills results in surface roughening, while re-emission of the particles make them redeposit on the valleys, resulting in surface smoothing. A low surface diffusion results in clustering of random atoms causing island growth on a wide area that is followed by side-wall growth of the clusters [111,112]. This would result in a rough morphology and is observed in Zone 1 of SZM.

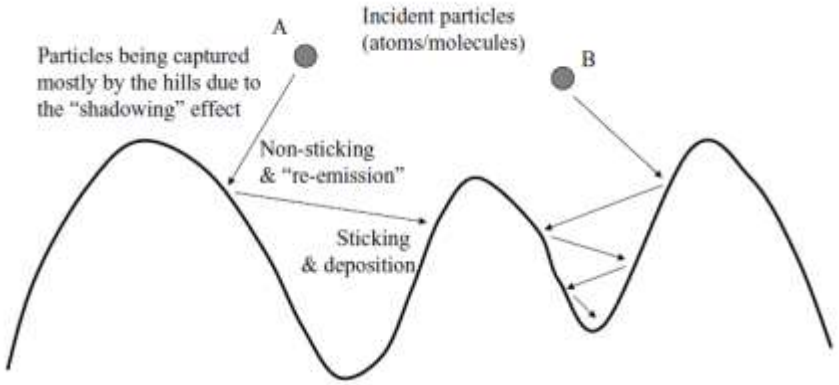

Figure 2.11. Shadowing and re-emission effects during film growth [117].

2.7 Nitrogen Doping of DLC

The incorporation of elements to modify the structural and mechanical properties of films is known as doping. The amorphous structure of DLC makes the incorporation of elements quite easily. A lot of researchers have tried doping different elements to DLC films and investigate their effects, especially with the aim to reduce the compressive stresses without compromising the desirable DLC properties [27]. Different chemical bondings introduced by adding different elements results

in the enhancement of a specific property for a particular application. Before the introduction of a dopant, one must consider the amount of dopant to be introduced, its dispersion and chemical nature in order to achieve the desired features [27]. Researchers have investigated doping DLC with light elements like silicon, boron, and nitrogen, and heavy metallic elements like titanium, cobalt and tungsten, to enhance a particular property as shown in Figure 2.12.

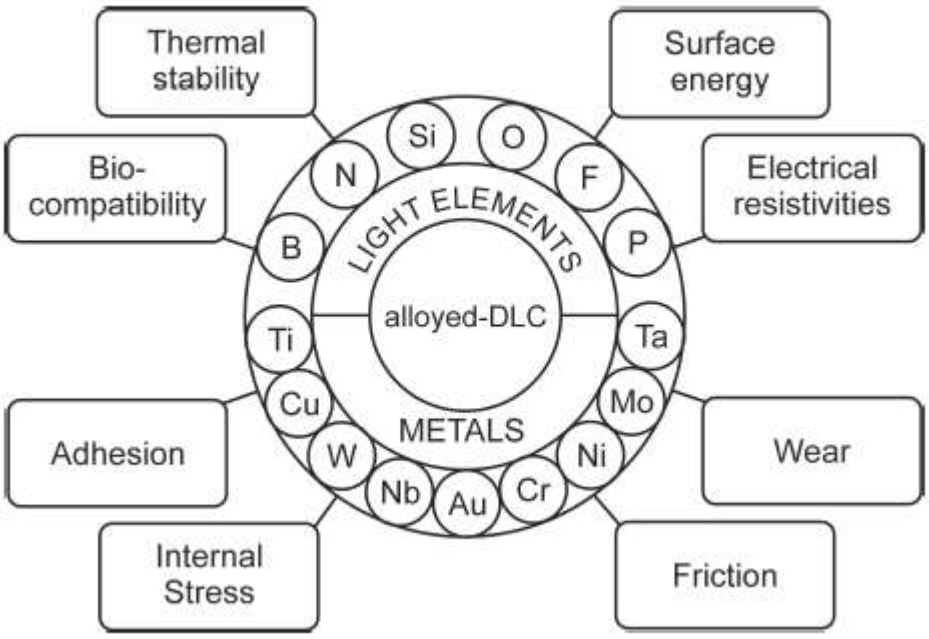

Figure 2.12. DLC doping with different elements [118].

Nitrogen has been widely investigated as a dopant for DLC films due to its versatile bonding configurations with carbon [119]. On addition of nitrogen, pentagonal rings might form to promote cross-linking between graphitic planes, resulting in enhanced toughness [120,121]. Nitrogen-doped DLC (NDLC) usually show better tribological properties than undoped DLC [122-124]. Adding nitrogen may increase sp^2 content in DLC film, decrease its residual stress, and thus improve its adhesion [67,125]. Although many studies have been conducted on nitrogen doped DLC films, not much work has been done on NDLC to 316L SS with a chromium nitride interlayer.

CHAPTER 3
MATERIALS AND EXPERIMENTAL METHODS

In the present research, reactive radio frequency (RF) magnetron sputtering was used to deposit chromium nitride interlayers and ion beam deposition was used to prepare DLC and NDLC coatings. After deposition, the interlayers and films were characterized using grazing incidence XRD, EDS, XPS, Raman spectroscopy, SEM, nanoindentation, Rockwell C indentation, and ball-on-disk tribological testing. The principles and descriptions of these techniques are given in this chapter.

3.1 Substrate Material Preparation

316L stainless steel sheet with a Rockwell hardness of B95 and a thickness of 4.78 mm was purchased from McMaster-Carr® and used as a substrate for CrN, DLC/CrN, and NDLC/CrN deposition. The sheet was cut into 1"×1" square samples and ground using #180 and #320 sandpapers. After that, the samples were further polished using diamond paste with a grain size of 9 μm, 3 μm, and 1 μm, respectively, to get a mirror-like surface. Finally, the samples were ultrasonically cleaned in water and ethanol.

3.2 Thin Film Deposition

3. 2.1 CrN deposition by radio frequency magnetron sputtering

Chromium nitride films were deposited using RF magnetron sputtering in a Hybrid Thin Film Deposition System, Model SPLD620-FLR, made by Plasmaionique Inc. A picture and a schematic of the deposition system is shown in Figure 3.1. It consists of an 8-inch diameter x 30 inches long vacuum chamber, a turbo pump and a mechanical pump, a throttling gate valve for pressure control and isolation, and two sputtering magnetrons for 3" targets with a maximum power of 300 W. The substrate holder can be heated up to 850 °C and allows motorized rotation, RF biasing, and translation of four-inch diameter substrates.

In the present thesis work, pure chromium (99.95%) target was sputtered using Ar (99.99%). Nitrogen (N_2) was introduced during chromium sputtering. The deposition parameters used are listed on Table 3.1. The base pressure was 6×10^{-7} torr for all the depositions. The working pressure was 10, 5 and 3 mTorr. The substrate temperature was room temperature, 100 °C, and 470 °C. The

substrate was rotated at a speed of 3 rpm for better film coverage and the substrate to target distance was kept 50 mm. All the films were deposited for a period of 4 hours.

Table 3.1. Deposition parameters for making CrN thin films.

Sample	**Ar Flowrate (sccm)**	**N_2 Flowrate (sccm)**	**Deposition Pressure (mTorr)**	**Power (W)**	**Voltage (V)**	**Temperature (°C)**	**Deposition Time (hours)**
CrN-1	30	15	10	300	182	23	4
CrN-2	30	15	3		220	23	
CrN-3	30	15	3		212	100	
CrN-4	30	15	10		179	470	
CrN-5	40	20	10		163		
CrN-6	30	15	5		194		
CrN-7	30	15	10	150	182		
CrN-8	30	15	3		222		

Table 3.2 shows the deposition parameters of CrN films with different deposition durations in order to investigate the effect of CrN interlayer thickness on the adhesion of DLC and NDLC thin films.

Table 3.2. Deposition parameters for CrN thin films with varying deposition time.

Sample	**Ar Flowrate (sccm)**	**N_2 Flowrate (sccm)**	**Deposition Pressure (mTorr)**	**Power (W)**	**Voltage (V)**	**Temp. (°C)**	**Deposition Time (hours)**
CrN-7.1	30	15	10	150	182	470	1
CrN-7.2							2
CrN-7.3							4
CrN-7.4							6
CrN-7.5							10

3.2.2 DLC and NDLC coatings deposition by ion beam deposition

A dual ion beam deposition (IBD) system that is manufactured by 4Wave Inc. was used to synthesize DLC and NDLC coatings on silicon and 316L SS substrates with CrN as an interlayer. Figure 3.2 shows a picture and a schematic of the IBD system. The system consists of a high vacuum chamber, a pumping system comprising of turbo pump and a mechanical pump, a substrate holder that can be tilted from 0°-90°, a target assembly, and two End-Hall (EH) low energy ion sources. One source is used for direct ion beam deposition while the other source is used for sputtering. The substrate holder, tilted at 45°, is 300 mm away from the deposition ion source. The system is cable of performing numerous tasks that include ion beam etching, ion beam deposition, and ion beam sputtering. Hydrogenated DLC could be synthesized from hydrocarbon gases using the deposition ion source while hydrogen free DLC coatings can be deposited by sputtering a graphite target particle using the other ion source.

(a)

(b)

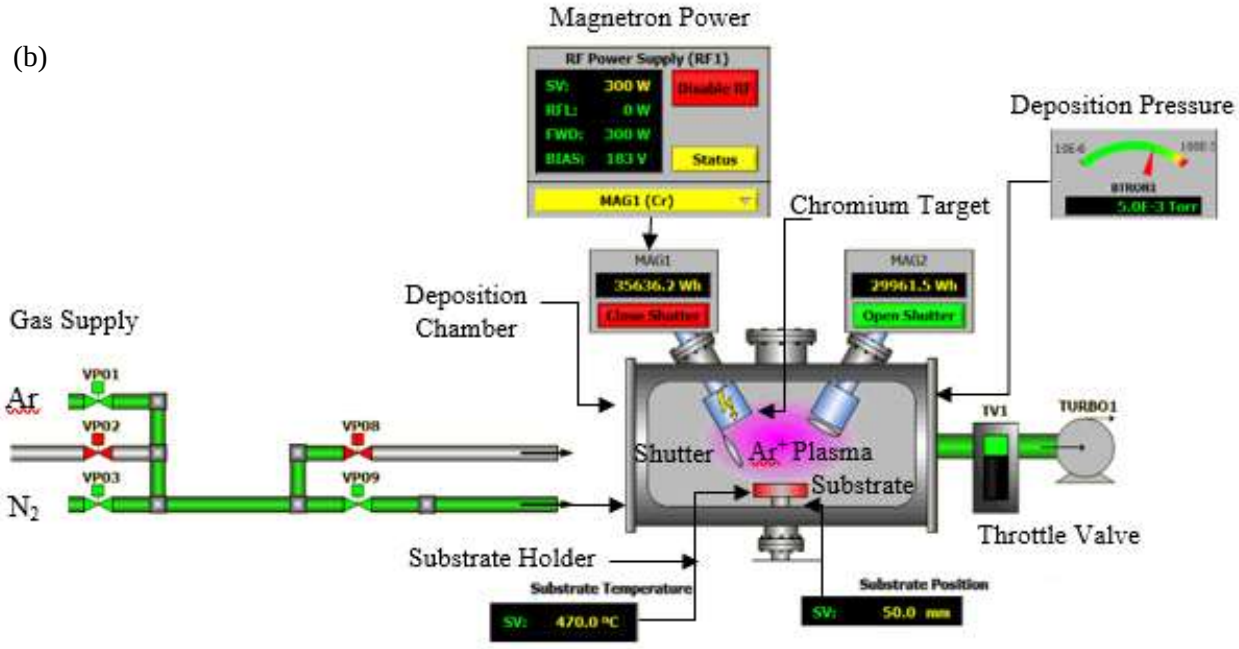

Figure 3.1. (a) Photograph of the Hybrid Thin Film Deposition System for Preparation of CrN films (b) its schematic structure.

In the present work, hydrogenated DLC and nitrogen doped DLC coatings were synthesized using direct ion beam deposition with an argon flow rate of 12 sccm and a methane flow rate of 5 sccm, optimum conditions found based on previous research conducted in our group. In addition to argon (Ar) and methane (CH_4), nitrogen (N_2) was introduced as a precursor gas for NDLC coating deposition. For NDLC deposition, N_2 gas was kept at 1 sccm. The mean ion energy during deposition was kept in between 80-85 eV and the beam current was kept 2 A. All the depositions were performed at room temperature for a period of 8 hours with substrate holder inclined at an angle of 45° to the incident beam. The base pressure was 1.3×10^{-7} torr and the deposition pressure was kept at 4.5×10^{-4} torr. Table 3.3 summarizes the deposition parameters for both DLC and NDLC coatings.

Table 3.3. Deposition parameters for DLC and NDLC coatings by IBD.

Sample	**Working Pressure ($\times10^{-4}$ torr)**	**Gas Flow Rate (sccm)**			**Ion Energy (eV)**	**Temperature (°C)**	
		Ar	**CH_4**	**N_2**		**Initial**	**Final**
DLC	4.46	12	5	-	80-85	12.6	38.5
NDLC	4.52	12	5	1	78-80	12.6	37.4

(a)

(b)

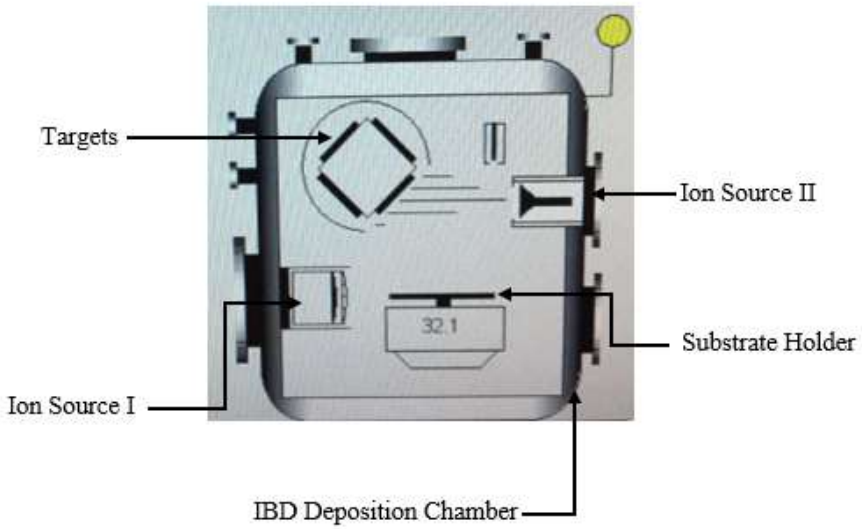

Figure 3.2. (a) Photograph of IBD system and (b) its schematic for DLC and NDLC coatings deposition.

3.3 Structural Characterization

3.3.1 X-Ray diffraction

X-ray diffraction (XRD) is the most commonly used technique to characterize and identify the phases in crystalline materials and to obtain their crystallographic structural information including preferred orientation, grain size, stress, and lattice parameters. As the name suggests, XRD uses X-rays as the incident beam. The X-rays are usually produced by metals like Cu, Co, and Fe upon bombardment with high energy electrons and are a continuous distribution of energies and wavelengths. A filter, that absorbs the unwanted X-ray photons, is usually installed to get desirable monochromatic X-rays, that is further converged into a narrow X-ray beam. This X-ray beam when comes in contact with the specimen is diffracted by the atoms. When the wavelength of the X-ray and the lattice spacing meet a specific condition, constructive interference occurs between the incident and diffracted X-ray beams. This condition is referred to as Bragg's Law and is given by:

$$n\lambda=2dsin\theta \tag{3.1}$$

where n is integral, λ is the X-ray wavelength, d being the lattice spacing and θ is the angle of incidence of X-rays. The X-rays can penetrate deep into the material up to a few millimeters and thus tradition XRD is good for bulk material identification. When it comes to thin film samples, the resulting X-ray diffraction signals would mainly come from the substrate and the diffraction intensity from the film would be too weak to be observed. In this case, grazing incidence XRD (GIXRD) is needed in order to eliminate the effect of the substrate. As most materials have a refractive index less than 1.0, when an incidence angle is a small enough, completely external reflection can be observed. An evanescent X-ray penetration in the material and its scattering results in highest intensity at the surface [132]. Therefore, even the incident X-ray is set at a small angle, the diffracted X-ray can be detected at any angle (2θ). In GIXRD, the X-ray penetration depth can be adjusted to a desirable value by changing the incidence angle (ω) to characterize crystalline thin films with various thickness from as low as a hundred nanometer to several micrometers.

A Rigaku Ultima IV X-Ray diffractometer equipped with a Cu source (a wavelength of 1.541 Å), shown in Fig. 3.3, was used to perform XRD on CrN thin films. The measurements were carried out on the Multipurpose Attachment in parallel beam mode. A PSA slit and a K_β filter (Ni foils)

were placed at the receiving end. 2θ was scanned from 30° to 90° with a scan rate of 4° per minute. A grazing angle of 3° was used to obtain GIXRD that is greater than the critical angle for CrN thin films in order to avoid total external reflection that results in no X-rays penetration in the thin films.

Figure 3.3. Rigaku Ultima IV X-Ray diffractometer.

3.3.2 Raman spectroscopy

Raman spectroscopy is a non-destructive structural characterization technique that uses Raman (inelastic) scattering of light [126]. The incident radiations, monochromatic light, are inelastically scattered by the atoms or molecules in the material for testing, causing a combination of molecular rotational, electronic or vibrational transition and are then collected [127]. A Raman spectrum is a plot of the inelastically scattered light as a function of a shift in radiation wavelength (Raman shift). Each resulting Raman spectrum of a material serves as a fingerprint of its interatomic and intermolecular bonds. Unlike X-ray diffraction, that cannot provide information on amorphous materials, Raman spectroscopy provides detailed information on the structure of amorphous materials like DLC [128] and thus has been widely used to characterize the bonding structure of DLC.

The Raman spectrum of diamond has a single sharp peak at 1332 cm^{-1} while that of a single crystal graphite has a sharp peak at 1580cm^{-1}, known as the 'G' peak. The Raman spectrum of disordered graphite shows a second mode at around 1350 cm^{-1} and is characterized as disorder 'D' peak [129,130]. The D and G modes of graphite are a result of stretching vibration of sp^2 C=C bonds. The relative ratios of sp^2 and sp^3 bonding present in a DLC coating can be determined by the deconvolution of D and G peaks in a Raman spectrum using Breit-Wigner-Fano (BWF) to fit G peak while Lorentzian to fit D peak [131]. Typical Raman spectra from different carbon structures are given in Figure 3.4.

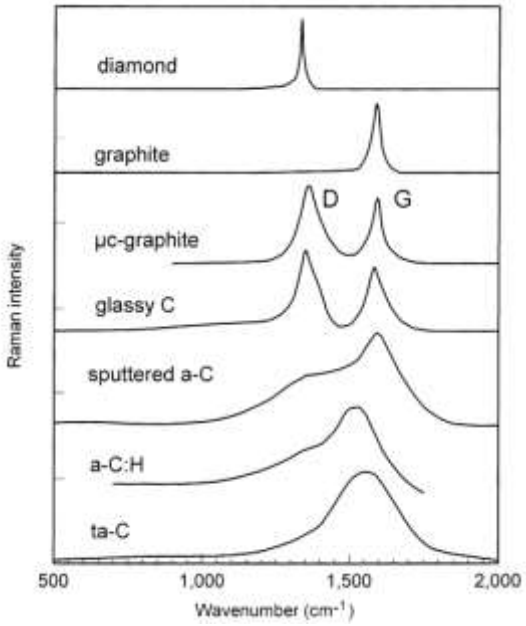

Figure 3.4. Typical Raman spectra of carbons [26].

Renishaw 2000 Raman spectroscope was used to chemically characterize DLC and NDLC coatings. The equipment is located at Saskatchewan Structural Science Center (SSSC), University of Saskatchewan. The measurements were taken using Ar ion laser, 514.5 nm wavelength, in a 1.5 μm spot size. Silicon was used as a standard for internal calibration before every measurement. The exposure time was 30 s. The data for each spectrum was accumulated with cosmic rays removal mode activated to reduce noise. The background of the spectra was removed first, and the spectra were then analyzed using Renishaw's WiRE (Windows-based Raman Environment) software.

3.3.3 X-ray Photoelectron Spectroscopy

X-ray Photoelectron spectroscopy (XPS), as the name suggests, works on the principle of photoelectric effect that utilizes X-rays of a characteristic wavelength to excite electrons from the orbitals of the material in testing. The emitted photoelectrons are then collected as a function of their kinetic energy. Thus, the XPS spectrum is a plot of electron counts versus electron kinetic energy in eV [133]. Figure 3.5 illustrates a schematic of the photoemission process.

The energy conservation takes place in the photon absorption process and is given by the following equation:

$$E_k = h\upsilon - E_B \quad (3.2)$$

Where E_k is the kinetic energy, incident photon energy is given by $h\upsilon$ and E_B is the initial binding energy of the electron. The values of binding energy E_B, characteristics to each element, can then be obtained using equation 3.2. As the bonding energies of outer-shell electrons are affected by the chemical bonds present in the material, chemical bonds can be identified by the relative position of the XPS peaks and elemental composition can be quantified based on the peak areas that are proportional to the number of orbitals in the volume under analysis. Therefore, information like the chemical state of the constituent elements, oxidation state, partial charge, and hybridization states can be known based on the position and shape of the peaks in an XPS spectrum.

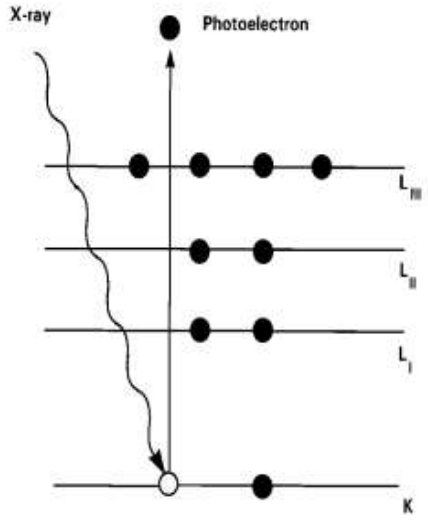

Figure 3.5. The photoelectron emission process [134].

Monoenergetic soft X-rays, Aluminum Kα X-rays (1486.6 eV) or magnesium Kα X-rays (1253.6 eV), are widely used as the incident radiation. These photons have the tendency to penetrate 1-10 μm into the solid material to produce photoelectrons. Nevertheless, the mean free path of the emitted electrons is between 0.5 to 5 nm, and thus the detected photoelectrons are emitted from a few atomic layers on the material surface [134]. This makes XPS a surface sensitive technique. XPS has been widely used to understand the hybridization bonding states of carbon [135-136].

XPS measurements were performed on a Kratos (Manchester, UK) AXIS Supra system at the Saskatchewan Structural Sciences Centre (SSSC). This system is equipped with a 500 mm Rowland circle monochromated Al Kα (1486.6 eV) source and combined hemispherical analyzer (HSA) and spherical mirror analyzer (SMA). An accelerating voltage of 15 keV and an emission current of 15 mA were used for most of the measurements. A spot size of hybrid slot (300x700 microns) was used for most of the samples but a spot size with a diameter of 110 microns was used for characterizing Rockwell C indents. All survey spectra were collected in binding energy ranging from 5 to 1200 eV with a step size of 1 eV and a pass energy of 160 eV. High-resolution scans of specific regions were conducted using a step size of 0.05 eV with a pass energy of 20 eV. For Rockwell C indents, C1s data was collected with a pass energy of 40 eV, a step size of 0.1 eV steps, an acceleration voltage of 15 keV, and an emission current of 25 mA. CasaXPS software was used to process and analyze the obtained data.

3.4 Surface Topography and Morphology

3.4.1 Optical profilometry

Profilometers, stylus and optical, are used to characterize coating thickness and surface topography. In stylus profilometer, a stylus, while being pressed on the specimen surface, is moved across the surface to trace the height variance and record the surface topographical image. Similarly, the thickness of the coating is directly measured by tracing the height drop at the film/substrate step. Disadvantages of a stylus profilometer include the limited accuracy to the stylus dimensions and the scratching of film surface during the scan.

Optical profilometer, on the other hand, is a non-contact profilometer that is based on interferometry and has higher accuracy compared to the stylus profilometer. In this, the beam from

the light source is split into two. One beam is reflected from the reference mirror inside the objective while the other is reflected from the specimen surface. The combination of these two beams results in constructive and destructive interferences that produce bright and dark bands in the fringe on the surface. When the optical path difference between the light reflected from the specimen surface and that reflected from the reference mirror is equal to the integral number of the wavelength of light, constructive interference happens. This optical path difference originates due to the variance in height of specimen surface as the reference mirror is close to perfect. The accuracy of the optical profilometer can be as high as 1 nm [156]. Figure 3.6 is an illustration of an optical profilometer structure.

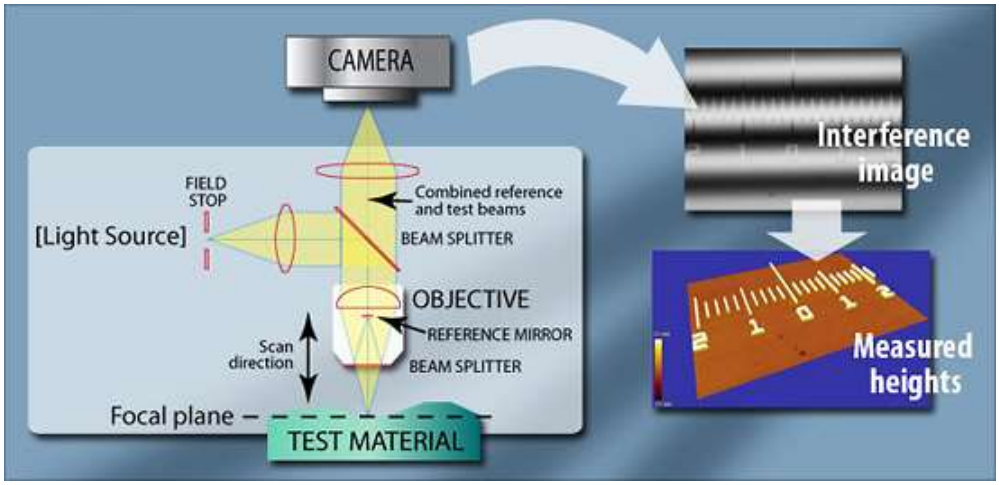

Figure 3.6. Schematic of an optical profilometer (Zygo Co.).

Zygo NewView 8000 optical profilometer, located in OC19, was used to investigate the film thickness and the film topography. Figure 3.7 is a picture of the optical profilometer used. A refractive index of 2 was used for DLC and NDLC analysis since optical transparency is inherited by DLC coatings with high sp^3 bonding.

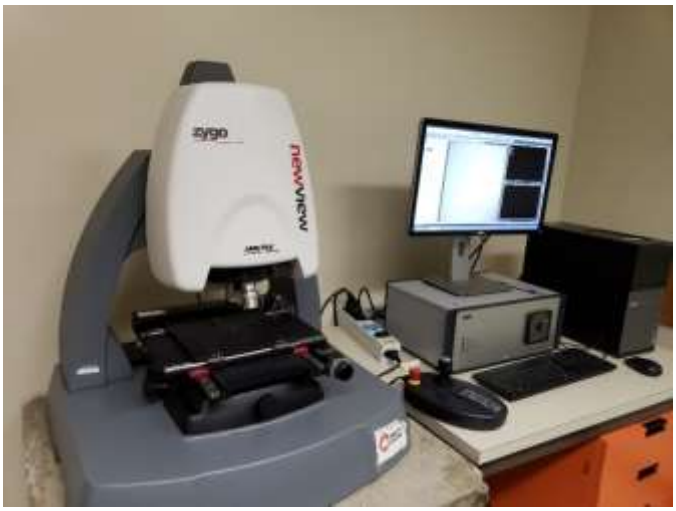

Figure 3.7. Photograph of Zygo NewView optical profilometer.

3.4.2 Scanning electron microscopy (SEM)

Scanning electron microscopy (SEM) is a widely used technique to characterize the surface morphology and chemical composition of materials. The electrons are generated by the electron source either thermionically from a tungsten filament cathode or by field emission. These electrons are then accelerated and focused into a fine beam, typically 10 Å in diameter, using electrical and magnetic field optics. The highly focused beam of electrons with a typical energy of 30 keV is then made to hit the specimen and the interaction results in different effects that include backward scattering of high energy electrons, knocking out of secondary electrons from the specimen surface with an energy of less than 50 eV and the emission of X-rays from the specimen in all directions. Figure 3.8 is an illustration of secondary signals generated resulting from the interaction of the electron beam with the specimen. The signals are then picked by X-ray detector and are processed and amplified by various amplifiers. The SEM image observed is a distribution map of the signal intensities that provide details of the specimen are scanned. The specimen needs to be an electrical conductor to avoid charge accumulation on the surface and so an insulator requires coated with a conductive coating [156].

Imaging at much higher magnification and the ability to provide with extra details apart from topographic information makes SEM superior over an optical microscope.

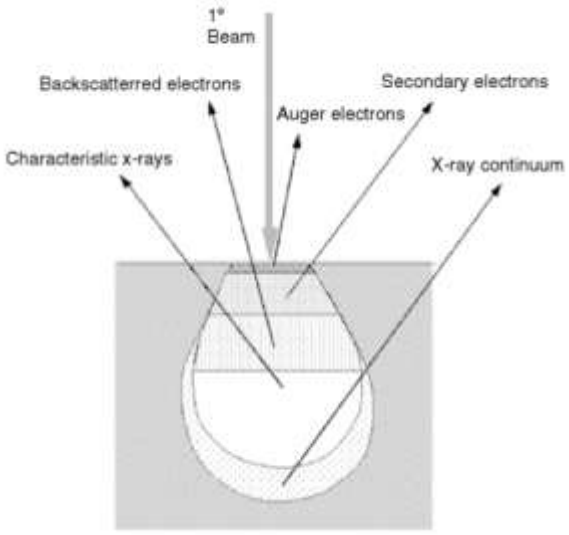

Figure 3.8. Illustration of several signs generated resulting from beam-specimen interaction [157].

A HITACHI UHR SU8000 Series field-emission scanning electron microscope (FE-SEM) with high resolution at the Western College of Veterinary Medicine (WCVM) Imaging Centre, University of Saskatchewan, was used to observe the cross-sectional and surface morphology of the films. Joel JSM-6010LV SEM was used to observe the imprint after Rockwell C indentations. Figure 3.9 shows the picture of the SEM used.

Figure 3.9. Joel JSM-6010LV scanning electron microscope.

3.5 Mechanical Property Testing

3.5.1 Nanoindentation for hardness and Young's modulus measurements

When measuring thin films hardness, the indenter penetration depth must be kept less than one-tenth of the film thickness to avoid the effect of the substrate [137]. Conventional hardness measurement techniques, Vickers and Rockwell, cannot be used to investigate the mechanical properties of the thin films as in these methods the indenter penetration depth is quite high and can not eliminate the effect of the substrate. To get reliable hardness values of thin films, nanoindentation is usually used.

Two methods are generally used for hardness measurement of thin films: direct measurement and theoretical modeling. In the case of direct hardness measurement, a range of different loads are applied, and hardness value is directly determined by using the right load to keep the penetration depth less than one-tenth of the film thickness with a fixed indentation size of 10 µm. On the other hand, when the penetration depth is over one-tenth of the film thickness, the measured hardness value is a combination of film and substrate hardness. In this case, a modeling approach is used to find the hardness value of film based on the film thickness and the mechanical properties of the substrate [138]. In order to get film hardness value by direct measurement, specialized instruments with ultra-low load, called nanoindenters, have been developed.

Figure 3.10 gives a typical loading unloading nanoindentation plot for a tetrahedral hydrogenated DLC sample [139]. Hardness and Young's modulus values are obtained by drawing a tangent to the unloading curve and extrapolating it to zero. The hardness is then calculated using the following equation:

$$H=0.0378(L_{max}/h_p^2) \tag{3.3}$$

where H is the hardness while plastic deformation is given by h_p and L_{max} is the maximum load. The Young's modulus E is calculated by:

$$E = 0.179\frac{(1-v^2)Lmax}{(hmax-hp)hp} \tag{3.4}$$

where h_{max} is the maximum depth of the indent.

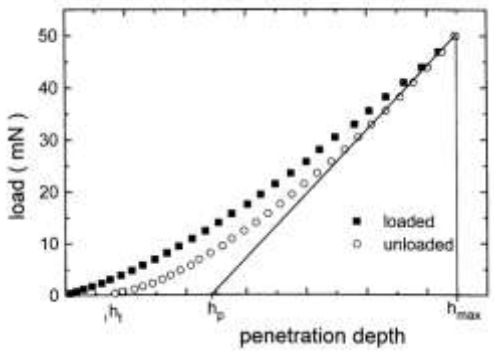

Figure 3.10. Loading unloading graph for ta-C:H during nano-hardness testing [139].

The accuracy of the measurements is a function of both the indentation depth and the film thickness. In addition, the tester is very sensitive to vibrations and sample roughness, thus, special care needs to be taken care during each measurement.

A nanohead mounted in a Universal Mechanical Tester (UMT) was used to carry out nanoindentation tests to measure the hardness and Young's modulus of the films. A 100 nm Berkovich indenter tip, inserted perpendicularly, was left at the desired load for 60s to minimize any effects on the measurements due to possible creep of the material. In the present work, to ensure the reproducibility of the hardness data, a scan test with 50 indentations was done from 3 to 21 mN load. A right load was then chosen so that the indentation depth was less than 10% of the total coating thickness, eliminating any substrate effect on the hardness value, and to rule out surface morphology influence, the indentation depth was kept more than surface roughness characteristic size. Figure 3.11 displays a picture of the UMT used for nanoindentation.

Figure 3.11. Picture of the UMT for nanoindentation.

3.5.2 Rockwell C indentation for adhesion evaluation

Sufficient adhesion strength is critical for film applications. There are several ways to evaluate the adhesive strength of films to substrates, including peel tests, scratching, indentation, and tape tests. Peel and tape tests are not able to evaluate hard films for applications requiring high adhesion. Scratching and indentation are the main methods to evaluate adhesion of hard thin films. Rockwell C indentation tests, developed by the Union of German Engineers (Verein Deutscher Ingenieure, VDI), is a cost-effective and an easy technique to qualitatively investigate indirect adhesion of hard thin films [137,140]. In the testing, a diamond 'C' indenter is used and applied perpendicularly with a load of 1471 N. The indents are then examined using a microscope and the extent of the damage surrounding the indents is compared with VDI guidelines 3198, Figure 3.12, to determine the adhesion qualitatively [141]. When the damage after Rockwell C indentation is similar to or less than HF4, the adhesion is classified as acceptable. However, if the damage is similar to HF5 or HF6, the adhesion is considered insufficient. Figure 3.12 shows the degree of damage for HF1 to HF6 adhesion strength [143]. In addition to adhesion, film brittleness can also be evaluated by the type and volume of film failure zone [143].

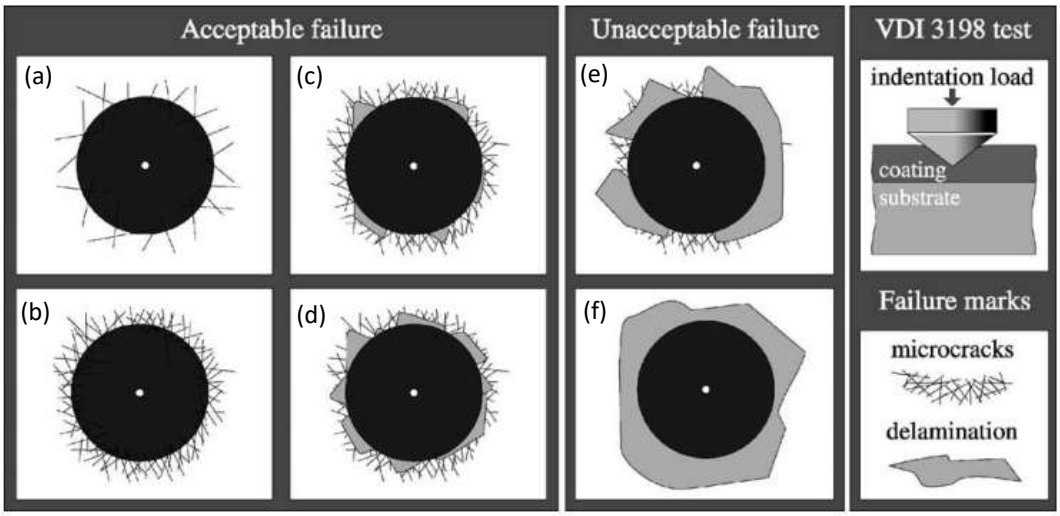

Figure 3.12. The principle of the VDI 3198 indentation test. (a) HF1, (b) HF2, (c) HF3, (d) HF4, (e) HF5 and (f) HF6 [143].

The adhesion strength of the film was evaluated using Rockwell C indenting testing. Three different areas on the film surface for each sample were indented to ensure consistency. The

indents were then analyzed using SEM. Figure 3.13 shows an image of the Rockwell C indenter used.

Figure 3.13. Rockwell C hardness tester.

3.6 Tribological Characterization

As friction and wear in moving parts accounts for a large amount of power consumption, the measurement of the tribological behavior of a thin film is very important before it can be used for tribological applications. Friction is measured by moving the surfaces in contact with a load applied over them. The application of load accounts for the static friction, while dynamic friction is analyzed during their motion. COF is defined as the ratio of the resistant force for movement to the applied normal load. As COF is not a fundamental material property, it is strongly affected by the conditions during the testing and is sensitive to surface chemistry, hardness and morphology of the surfaces in contact. This result gives the value of the coefficient of friction

Another extrinsic property that is essential for contacting materials in motion is wear. It is defined the loss of a material caused by a dynamic contact with another surface. It can be classified as lubricated and non-lubricated wear. The mechanisms involved behind wear are quite complicated with several mechanisms, including abrasive, adhesive, fatigue, fretting and polishing, might involve in a single one. The wear mechanisms and their interrelation are summarized in Figure 3.14 [144]. Wear rate describes how quickly the material degrades under given conditions

and can be determined by measuring weight loss or wear volume. Like COF, wear rate is also condition sensitive [144].

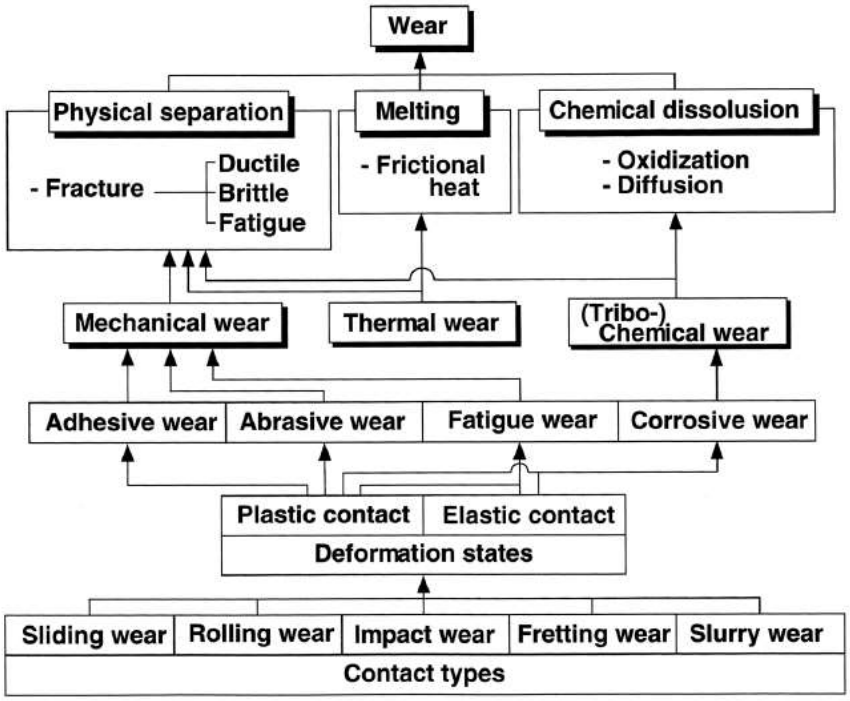

Figure 3.14. Wear mechanisms and their interrelation [144].

Friction and wear testing of the films with good adhesion was conducted using CETR UMT tribometer with a ball-on-disk configuration in the reciprocating movement mode. The testing was carried out in a room temperature saline solution (0.90% w/v of NaCl in distilled water). Saline solution maintains a stable pH and therefore is used in many biological applications [159]. Also, since 316L SS is widely used in a chloride environment, NaCl solution was used. AISI 302 stainless steel balls of 4 mm diameter were used as sliding counter material against the film (DLC and NDLC) coated 1"×1" square steel samples. This steel counter material was used in tribology testing because 316L SS showed very poor tribological properties when in contact with this steel. A constant load of 5 N was used for all the tests. The sliding displacement length was 2.5 mm and each test was carried out for 5000 cycles. The testing conditions were set based on the equipment capabilities and the sample size. The wear volume of the specimen surface was then measured

using the optical profilometer described in 3.4.1. Figure 3.15 shows the UTM used for tribological tests.

Figure 3.15. The UMT used for tribological tests with a ball-on-disk configuration.

CHAPTER 4
RESULTS AND DISCUSSION

This chapter is divided into four parts. in section 4.1 I report the effect of deposition parameters on the structure and properties of CrN thin films. In section 4.2 the effect of the structures and properties of CrN interlayers on DLC adhesion to 316L SS substrate were presented. In section 4.3 I describe the effect of CrN interlayer thickness on the adhesion of DLC to 316L SS substrate and show a comparison of DLC and NDLC adhesion when using the similar thickness of CrN interlayer. Finally, in section 4.4 the tribological behavior of bare 316L SS, DLC, and NDLC thin film-coated 316L SS is discussed.

4.1 Effects of Deposition Parameters on CrN Film Structure and Properties

CrN thin films were fabricated on single crystal silicon and 316L SS substrate simultaneously by reactive radio frequency magnetron sputtering. The effects of deposition parameters on the phase and chemical composition, deposition rate, surface roughness, surface and cross-sectional morphologies, hardness and adhesion of the films were investigated using XRD, EDS, XPS, optical profilometry, SEM, nanoindentation, and Rockwell C indentation. The structure of CrN films was found to be controlled by the deposition pressure and substrate temperature.

4.1.1 Phase and chemical composition

4.1.1.1 XRD

The XRD patterns of CrN thin films deposited using different deposition parameters are shown in Figure 4.1. Only one crystalline phase, fcc-CrN, was detected in the thin films and no Cr_2N peaks were observed. In addition, most of the films exhibited preferred orientations as the relative intensity of the peaks varies.

For CrN-1, deposited at room temperature and 10 mTorr, only (111) and (222) peaks showed up. Both peaks are broadened, which might be due to the grain size effect. However, in the case of GIXRD, there is instrumental broadening which makes XRD features more difficult to interpret [160]. When the deposition pressure was decreased to 3 mTorr while keeping the same deposition temperature, a peak corresponding to (220) plane appears, as seen in the XRD pattern of CrN-2. When the deposition temperature increased to 470 °C, five peaks corresponding to (111), (200),

(220), (311) and (222) planes appear with a very strong (111) peak. Films deposited at a high working pressure of 10 mTorr (CrN-1, 4, 5 and 7) show a very strong (111) peak, whereas, in case of a low deposition pressure of 3 mTorr (CrN- 3 and 8), the (220) peak becomes very strong. When the sputtering power reduces from 300 W to 150 W (CrN-7) while keeping the same deposition temperature and pressure, (222) peak disappears.

The change in preferred orientation with reducing gas pressure from 10 mTorr to 5 mTorr and finally to 3 mTorr is because lowering the pressure reduces collisions of sputtered atoms with the gas molecules and subsequently reduces energy loss. These energetic particles bombard the film surface with more energy resulting in the atoms relaxing to an energetically more favorable site. Therefore, this formation of the (220) preferential orientation can be attributed to the low surface energy [145]. Similarly, high deposition temperature enhances the surface diffusion of atoms to sites of low surface energy, similar to the case of lowering pressure.

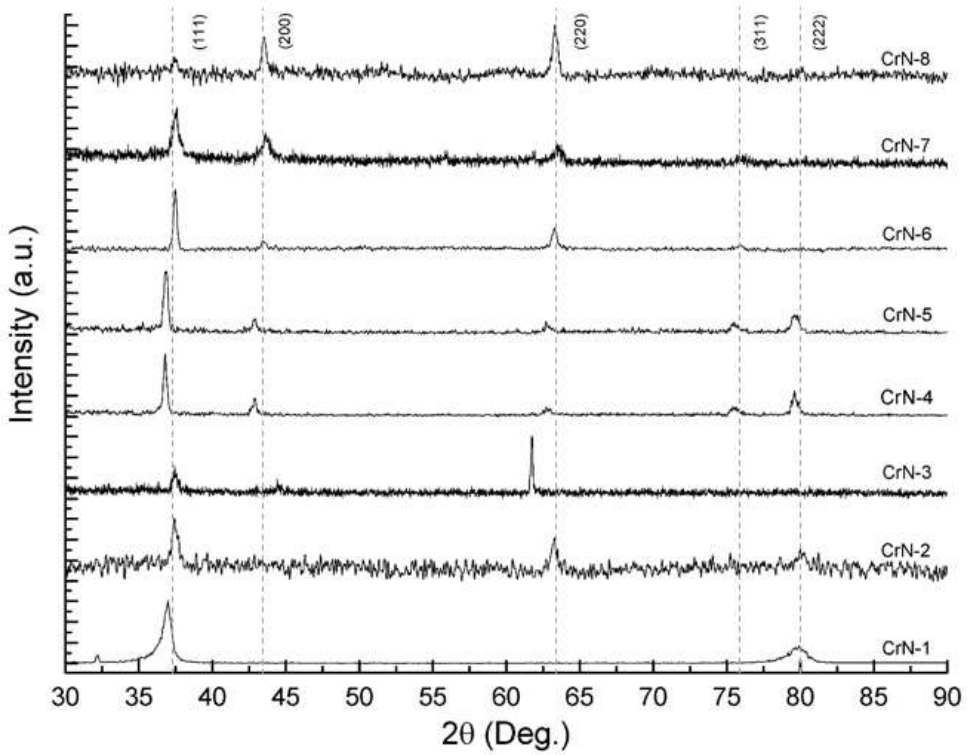

Figure 4.1. GIXRD patterns of CrN films deposited under different parameters.

Furthermore, a left-shift in peak positions was observed for CrN-4 and CrN-5. The left-shift indicates decreased lattice parameters, which is probably due to the compressive stress in the films.

The results show that CrN thin films with different preferred orientations can be produced by changing deposition temperature and pressure.

4.1.1.2 Energy Dispersive Spectroscopy (EDS)

An EDAX analyzer attached to the FESEM was used to get the EDS spectra of the CrN thin film samples. Based on the spectra, a semiquantitative chemical composition of the CrN thin films can be obtained. Figure 4.2 displays an EDS spectrum for CrN-4 and based on the spectrum, we calculated the composition and the result shows that the atomic percentage of nitrogen and chromium is 45 at.% and 55 at.%, respectively, and the atomic ratio of N to Cr is close to 1. The results from EDS analysis are similar for all the samples, confirming that all the samples having a CrN structure.

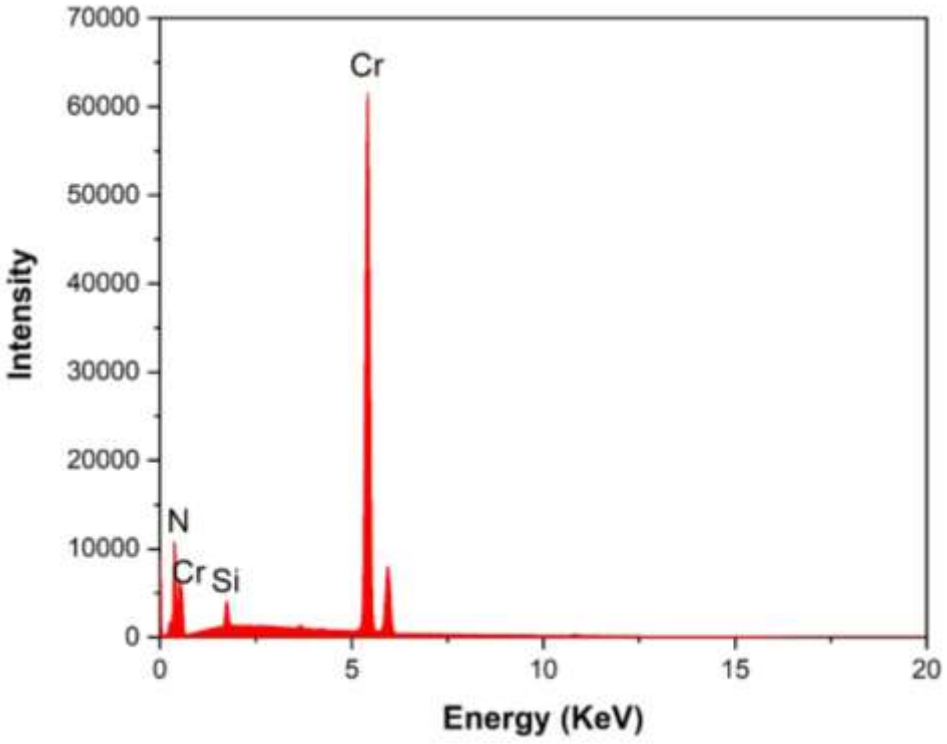

Figure 4.2. EDS analysis of CrN-4.

4.1.1.3 X-ray Photoelectron Spectroscopy (XPS)

XPS survey spectra of the CrN thin film surfaces show peaks of Cr, N, O and C. O and C are probably due to the surface contamination from exposing to atmosphere. For all the spectra, C 1s peak at 284.6 eV was used as a reference to calibrate the XPS spectra [146]. In order to obtain more detailed chemical information, high-resolution Cr 2p and N 1s spectra were also taken for the samples. Figure 4.3 shows the typical XPS spectra of Cr 2p and N 1s taken on the surface of CrN-4 thin films. The spectrum of Cr 2p shows two strong peaks at binding energies of 575.6 eV and 585.6 eV, corresponding to Cr $2p^{3/2}$ and Cr $2p^{1/2}$, respectively. The Cr $2p^{3/2}$ peak at 575.6 eV can be attributed to CrN [146]. Peaks corresponding to metallic chromium at 574.3 eV and to Cr_2N at 574.5 eV were not observed. Based on the intensity of the peaks, the atomic ratio of N to Cr is approximately 0.9, which is close to the stoichiometric ratio of CrN.

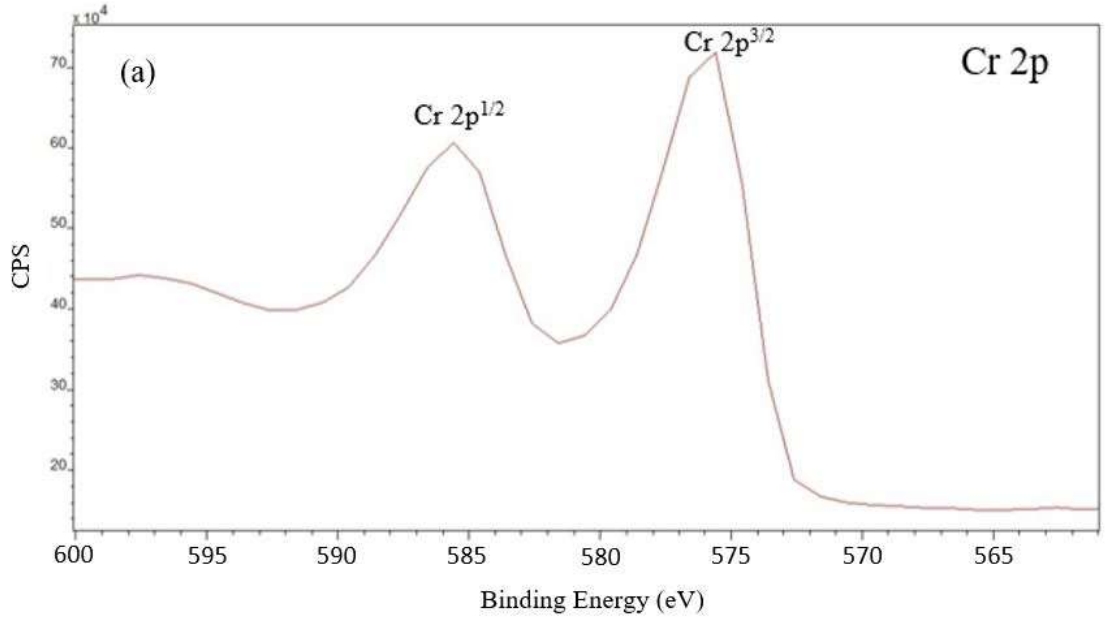

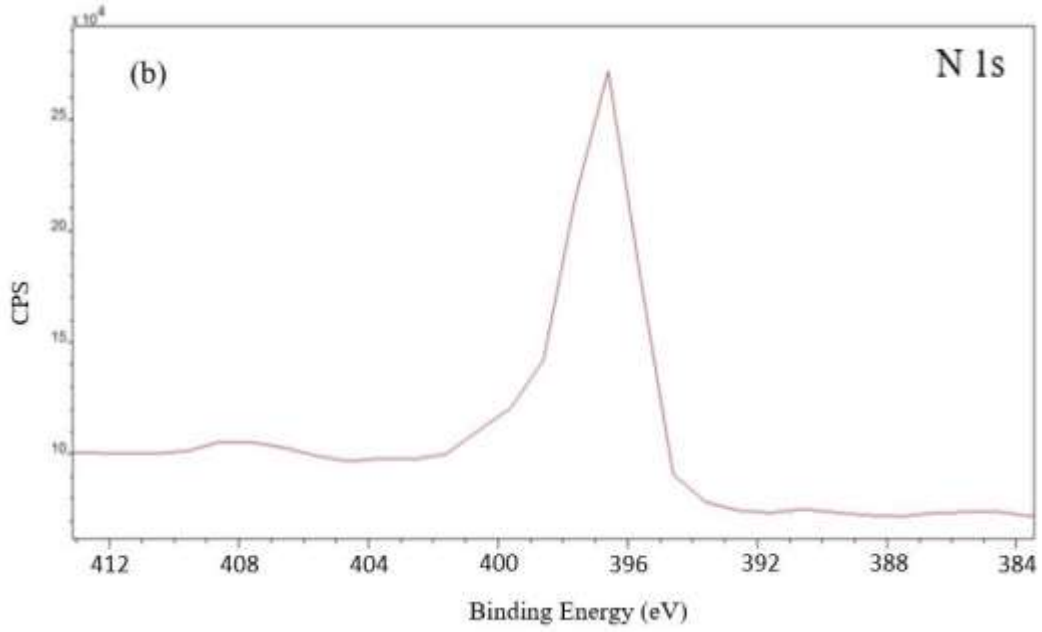

Figure 4.3. Survey XPS analysis of CrN-4 (a) Cr 2p and (b) N 1s.

The chemical state of nitride films can be determined by the binding energy of N 1s peak. The N1s peak of Cr nitrides is usually between 396 and 397 eV [147]. The N1s spectrum of the films consists of only one main peak at 396.6 eV, corresponding to CrN, whereas it is 397.5 eV for Cr_2N [147].

Furthermore, the 1:1 stoichiometry of CrN was not entirely reached because of impurities. Since Ar etching was not done, the film in the as-deposited condition showed oxygen and carbon peaks along with Cr and N. The formation of oxides and carbides is associated to the impurities in the chamber and when the sample was removed from the vacuum chamber and exposed to the atmosphere.

4.1.2 Deposition Rate

The thickness of the deposited CrN thin films was measured using an optical profilometer and further confirmed using SEM. Figure 4.4 shows the thickness of CrN films deposited for 4 hours.

When the deposition pressure was kept the same, e.g. CrN-1 & CrN-4, the deposition rate was not affected by the substrate temperature ranging room temperature to 470 °C. This can be explained by understanding the effect of substrate temperature on sticking coefficients of Cr atoms. The

sticking coefficients of sputtered atoms are near unity regardless of the substrate temperature as the sputtered atoms possess high energy in the order a few eV [104].

When keeping substrate temperature constant, the rate of deposition was found to decrease with the reduction of working pressure. This is evident by comparing the thickness of CrN-1 (2.1 μm) with that of CrN-2 (1.8 μm) where the pressure decreased from 10 mTorr to 3 mTorr. This is understandable by considering the phenomenon of resputtering caused by the momentum transfer from the incoming energetic particles. The deposited atoms on growing film surface could be remitted when obtaining sufficient energy from the bombarding atoms. Decreasing gas pressure reduces the collision probability of the sputtered atoms, causing less energy loss. Therefore, the particles possess higher energy, which re-sputter the deposited atoms on the surface, decreasing the film deposition rate.

The decrease in thickness with decreasing sputtering power from 300 W (CrN-4) to 150 W (CrN-7) is attributed to the fact that less Cr particles (atoms and clusters) are sputtered at lower sputtering power to form the CrN thin films.

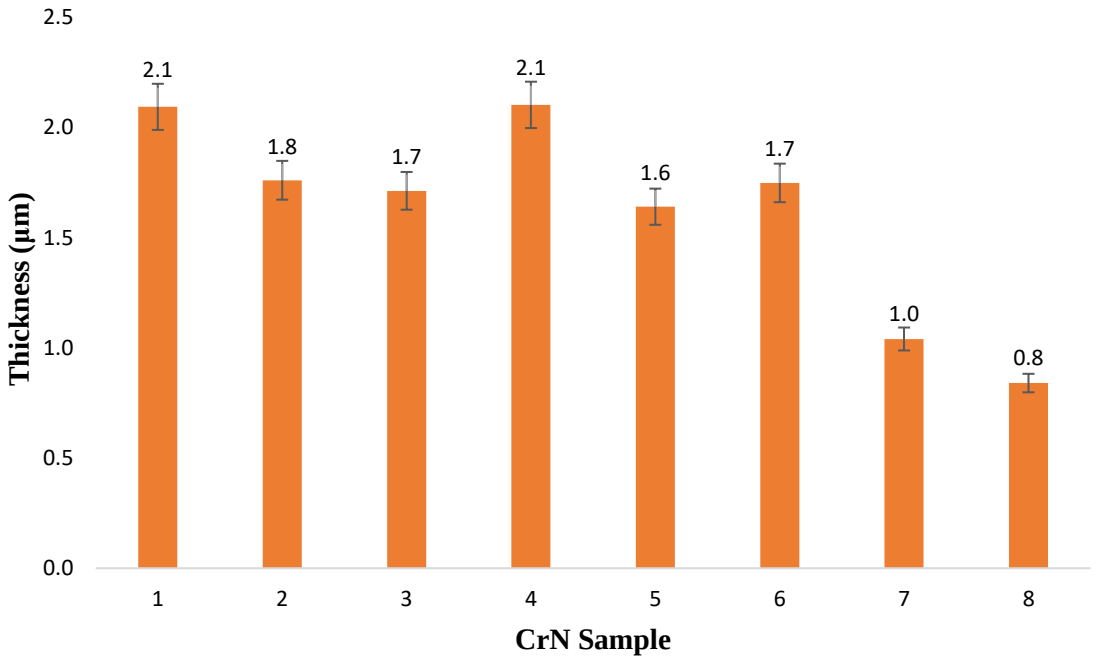

Figure 4.4. The thickness of CrN thin films deposited for 4 hours.

4.1.3 Surface roughness

The root mean squared (RMS) roughness of CrN thin film was measured by an optical profilometer. Figure 4.5 shows the images with the corresponding RMS roughness values. It is observed that CrN-4 deposited at elevated temperature (470 °C) has similar surface roughness as CrN-1 deposited at room temperature. This result shows that the enhanced surface diffusion at a higher temperature plays little role in smoothing the surface.

CrN thin films deposited at low deposition pressure (CrN-2, 3, 6 and 8) show much smoother surfaces than those deposited at higher pressures. This can be explained by the mean free path of depositing particles [100]. The lower the pressure, the longer the mean free path, and the higher the energy of the depositing particles, which enhances surface diffuse and results in smoother films. One can also note that the surface becomes smoother with the increase of substrate temperature at a low working pressure, indicating surface diffusion plays an important role in smoothening the thin films deposited at low working pressures. The enhanced re-emission caused by higher energy of sputtered atoms would be the dominant mechanism of this surface smoothing.

The highest surface roughness was seen in CrN-5, which is 2.6 nm. This is probably due to the fact that the samples were deposited with high gas flow rates (Ar: 40 sccm and N_2:20 sccm), which might cause more collisions before reaching the substrate surface.

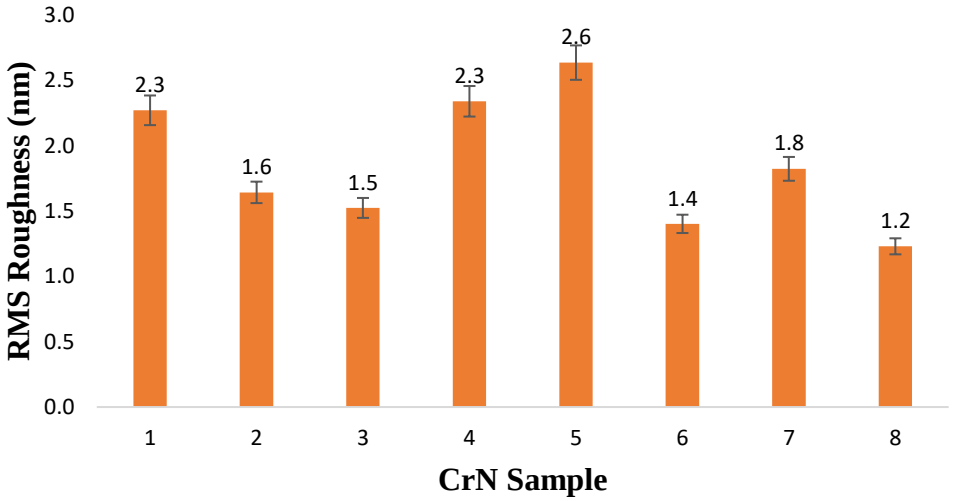

Figure 4.5. The surface roughness of as-deposited CrN films with varying deposition parameters.

4.1.4 Surface and Cross-Sectional Morphology

Surface and cross-sectional morphology of CrN thin films deposited under different process parameters was studied by FESEM. Figure 4.6 and 4.7 shows the cross-sectional and surface morphology of CrN thin films, respectively.

The SEM images show that the fcc CrN films exhibit columnar grain structure, in which the grains grow in the direction perpendicular to the substrate. The films prepared at low pressure and elevated temperature exhibit smooth and dense morphologies whereas the films deposited at room temperature show a porous structure. CrN-1 & 2 deposited at low working temperature demonstrate primary features of Zone 1 structure described in structure zone model (SZM) [106]. The reason for this porous structure is that the particles emitted from the target undergo a series of collisions and lose most of their energy before they deposit on the surface. The low energy of depositing particles and the low temperature make them difficult to diffuse on the surface of the growing films, and thus the pores and microholes cannot be filled, leading to the formation of porous films [100].

With increasing substrate temperature (CrN-3, 4, 5, 8), the porous structure changes to a denser and less permeable structure with fine grains near the substrate and V-shaped columns on the top of the films like Zone T structure in SZM [106]. This formation of a denser structure with increasing deposition temperature can be explained from following two aspects. Firstly, increasing deposition temperature increases the temperature of the gases involved and decreases the gas density that leads to the increase of the mean free path and thus, the decrease of energy loss of the sputtered atoms. Therefore, the depositing atoms possess higher energy to be able to diffuse on the growing surface to fill the pores to make the films dense. Secondly, increasing substrate temperature promotes the diffusion of adatoms on the thin films surface and therefore makes the film denser [100].

The most notable change in the structure was seen by changing the working pressure. The films deposited at a high deposition pressure of 10 mTorr (CrN-1 and 4) show columns perpendicular to the substrate surface whereas films deposited at low pressure of 3 mTorr (CrN-2, 3, and 8) show columns at an angle inclined to the substrate. One possible explanation to this angular growth of columns is the less interaction of particles coming from target to the substrate surface. With

decreased deposition pressure there are fewer particles and hence a smaller number of collisions of atoms from target to substrate. This results in atoms reaching the substrate surface with a fixed angle instead of depositing randomly, resulting in grain growth at an inclined angle, that is the same as that of the target to the substrate. However, in case of increased working pressure, the particles ejected from the target undergo a series of collisions with other particles and deposit on the substrate surface from all different angles.

The surface morphological images illustrated in Figure 4.7 show that the CrN films deposited at room temperature have a pyramidal-like structure with pores as seen in Fig. 4.7 (a) for CrN-1. With an increase of the deposition temperature, the surface morphology changes from triangular structure to a more faceted structure as seen in Fig, 4-7 (d) for CrN-4. Both the sticking coefficient and mobility are important for the grain growth. Increasing deposition temperature decreases the sticking coefficient and increases mobility. The balance of these two factors makes the deposition temperature have a little effect on the grain size of the thin films.

By decreasing the deposition pressure (CrN-2, 3 and 8), the grain columns incline to an angle and the pores were filled up because of the higher energy induced enhanced diffusion. Therefore, the smoother surface was observed for the samples.

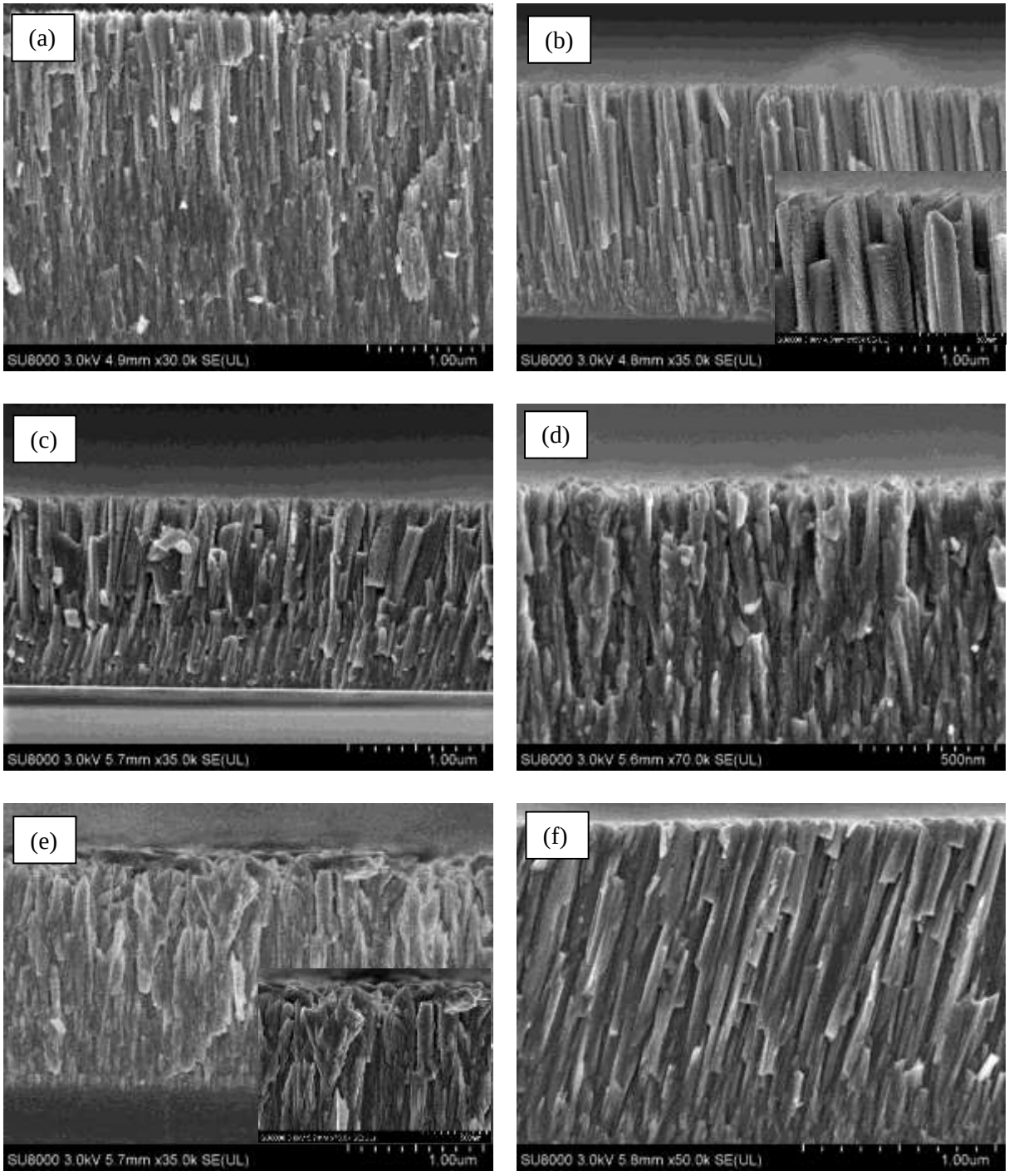

Figure 4.6. Cross-sectional FESEM images of (a) CrN-1, (b) CrN-2, (c) CrN-3 (d) CrN-4, (e) CrN-5 and (f) CrN-8.

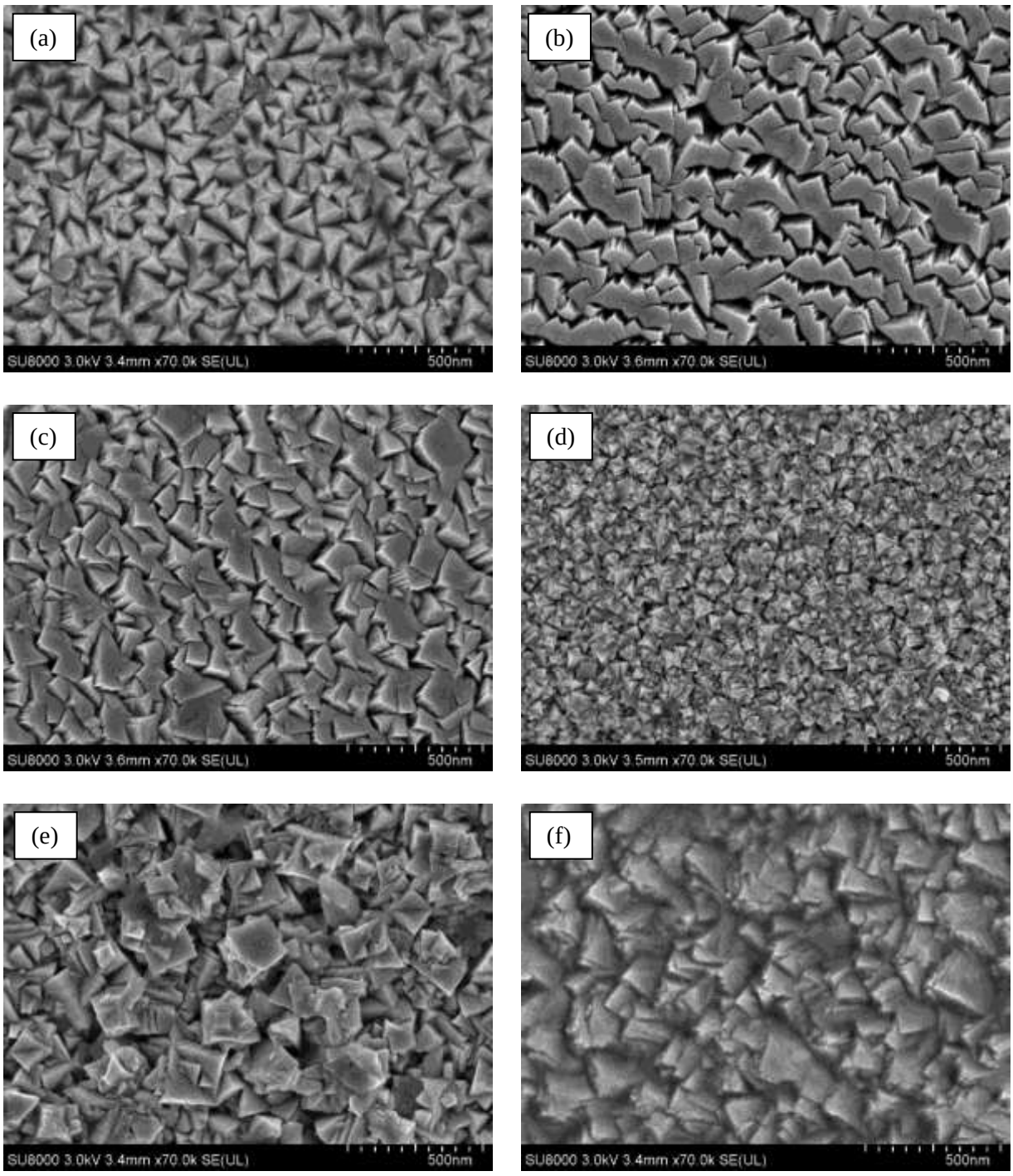

Figure 4.7. Surface FESEM images of (a) CrN-1, (b) CrN-2, (c) CrN-3 (d) CrN-4, (e) CrN-5 and (f) CrN-8.

4.1.5 Hardness

Hardness and Young's modulus values of the CrN samples are summarized in Table 4.1. In addition to that, H/E* and H^3/E^{*2} values are also included. Where E* is the effective elastic modulus and is equal to $E/(1-\nu^2)$, and ν being the Poisson's ratio. Instead of hardness value alone, these ratios have been recently found to be more useful to predict the wear and plastic deformation resistance of coatings. It has been reported that hard coatings with higher H/E* and H^3/E^{*2} values have a higher tendency to distribute the applied load to the coating over a wider area, resulting in enhanced resistance to cracking and plastic deformation [148]. The value of ν for CrN taken for the calculation was 0.28 [149].

The lowest hardness value 2.4 GPa was observed for CrN-1, which was deposited at room temperature and a high pressure of 10 mTorr. Decreasing the working pressure increases the hardness significantly. The hardness value increases to 3.1 GPa when reducing the pressure to 3 mTorr while keeping the deposition at room temperature. Increasing deposition temperature can also increase the hardness of the films. The highest hardness value and the highest corresponding H/E* and H^3/E^{*2} ratios were observed for CrN-8, which was deposited at a high temperature of 470 °C and a low pressure of 3 mTorr. Since CrN-4 and 7 were deposited under similar conditions, they showed similar hardness values and thus only CrN-4 is reported here.

It is not difficult to understand why decreasing deposition pressure and increasing deposition temperature can increase the hardness of films. As discussed in section 4.1.4, decreasing working pressure increases the energy of depositing particles and thus the mobility of the adatoms, which results in decreased grain size and increased film density. In a similar way, increasing deposition temperature increases the mobility of adatoms and thus increases the film density. In addition, this increased energetic bombardment at low deposition pressure can also induce high compressive stresses [145]. Reduced grain size, denser thin film structure and increased compressive stresses all contribute to increased hardness values.

Table 4.1. Hardness and Youngs's modulus of CrN thin films.

Sample	**Hardness-H (GPa)**	**Young's Modulus-E (GPa)**	**H/E***	**H^3/E^{*2} (GPa)**
CrN-1	2.4 ± 0.3	59.2 ± 2.6	0.037	0.0034
CrN-2	3.1 ± 0.1	118.8 ± 5.8	0.024	0.0019
CrN-3	5.8 ± 0.2	139.4 ± 16.2	0.039	0.0087
CrN-4	8.0 ± 0.2	165.4 ± 9.5	0.045	0.016
CrN-5	4.6 ± 0.5	148.5 ± 5.3	0.028	0.0037
CrN-6	10.9 ± 0.6	202.6 ± 17.8	0.049	0.026
CrN-8	12.3 ± 0.2	216.9 ± 18.1	0.052	0.033

4.1.6 Adhesion

Figure 4.8 shows the SEM images of CrN thin films deposited on 316L SS after Rockwell C indentation testing. We can see that all the CrN samples have good adhesion with no spallation or cracking of the films surround the imprint except for CrN-6 & 8, which were deposited at low pressure and high temperature and show high hardness.

One main reason for the poor adhesion of CrN-6 and 8 samples is the high residual stresses in them. Multiple factors that induce this high residual stress include the thermal stress caused by the thermal expansion coefficient mismatch between the thin film and the substrate when cooling down from elevated deposition temperature and the intrinsic stresses caused by gas entrapment and energetic particle bombardment [150].

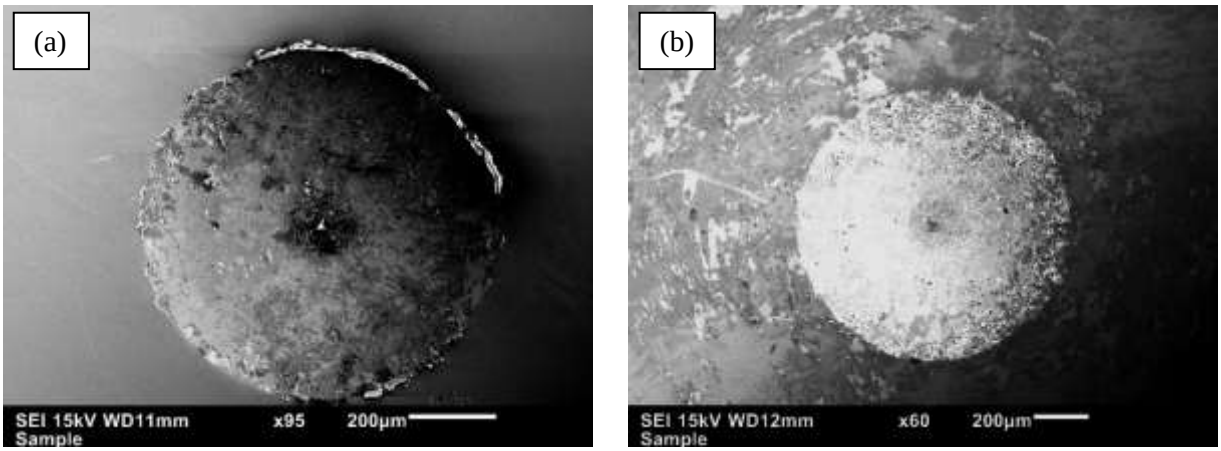

Figure 4.8. SEM images of the CrN thin films on stainless steel substrate after Rockwell C indentation (a) CrN-4 and (b) CrN-8.

4.2 DLC coatings on 316L SS with a CrN interlayer

In this section, DLC coatings were deposited on 316L SS substrate with CrN as interlayers. The effect of the structure and properties of CrN interlayer on the adhesion of DLC was investigated. The DLC coatings were characterized using Raman spectroscopy, SEM, X-Ray Photoelectron Spectroscopy, nanoindentation testing and Rockwell C indentation testing. The results show that CrN interlayer having a net-like structure with a hardness between DLC and SS can significantly improve the adhesion of DLC on SS.

4.2.1 Structural Characterization

4.2.1.1 Raman Spectra of DLC

The Raman spectra obtained from the as-deposited DLC on silicon wafers and CrN interlayered SS substrate are shown in Figure 4.9. The characteristic amorphous nature of the coating is confirmed by the broad Raman peaks. The disordered D peak at around 1310 cm^{-1} and the graphitic G peak at around 1530 cm^{-1} are typical peaks of DLC [131]. sp^2/sp^3 bonding ratio in the DLC coatings can be estimated by the intensity ratio of D and G peak (I_D/I_G) and they are inversely proportional. A decrease in the I_D/I_G ratio represents an increase in sp^3 bonding percentage in the

DLC coatings [135]. I_D/I_G ratios of 0.48 and 0.65 were observed on silicon and steel substrate, respectively. This indicates a higher sp^3 bonding percentage in the DLC coatings with Si as substrate.

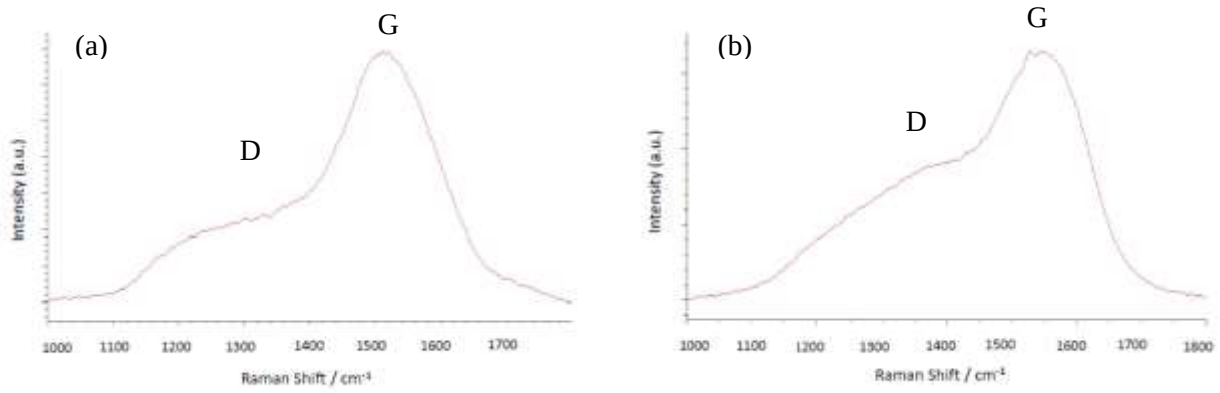

Figure 4.9. Raman Spectra of DLC coatings on (a) silicon and (b) CrN interlayered 316L SS.

4.2.1.2 XPS results

Figure 4.10 shows the curve-fitted C1s XPS spectrum of DLC. CasaXPS software was used to deconvolute the XPS spectra using the Gausian-Lorentzian function. The highest peak is seen at 285.17 eV corresponds to sp^3 C-C bonding, indicating a high sp^3 concentration in the DLC coating. The peak at 284.82 eV corresponds to sp^2 C=C bonding. Accordingly, the sp^2 to the sp^3 ratio of the DLC coatings can be estimated based on the relative intensity of C=C and C-C bondings. The sp^2/sp^3 ratio of the DLC coatings is estimated to be 0.54, sp^3 bonding percentage of 65%, close to the estimated value based on Raman spectra. The shoulder with a binding energy of 286.97 eV is from C-O bonding [151,152], indicating the coating surface is contaminated with oxygen.

The presence of sp^3 bonding in DLC can also be verified via XPS spectrum at low-bonding energy regime, shown in Figure 4.11. Mansour, A, et al. 1991 report that the XPS peak around 15 eV is of s and p character and is mainly from sp^3 carbon bonds. The intensity of this peak is very weak for graphite and totally absent for graphitic amorphous carbon [152]. Figure 4.11 shows a strong peak around 15 eV, confirming the presence of high percentage of sp^3 bonds.

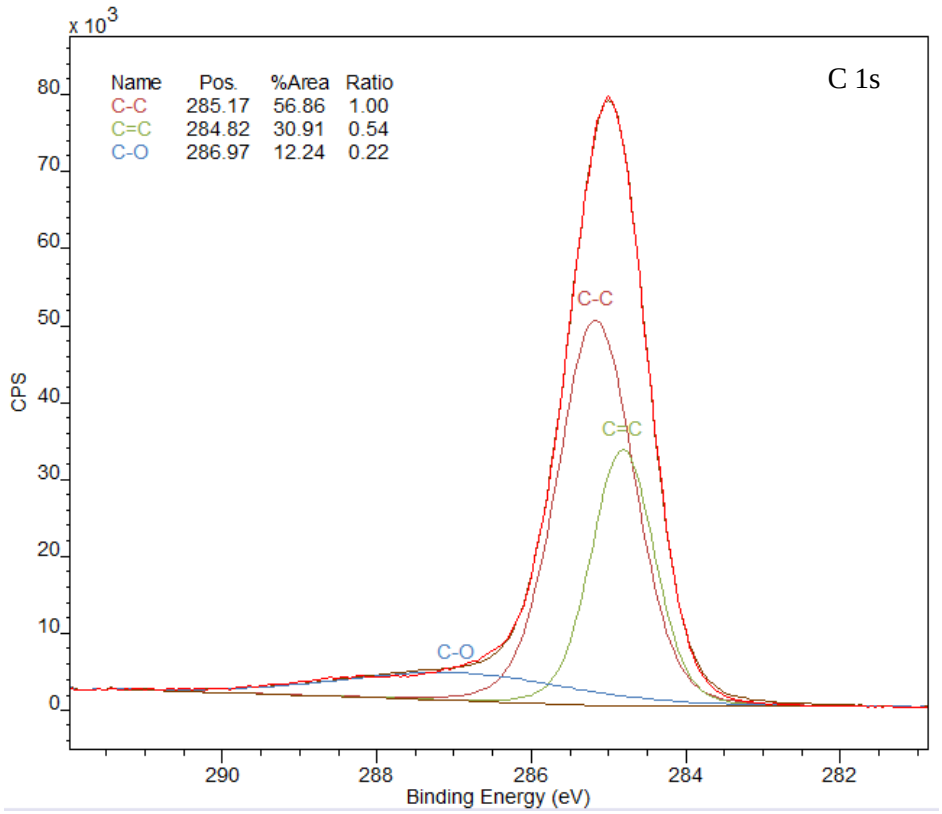

Figure 4.10. Deconvolution of C1s XPS spectrum of DLC coating.

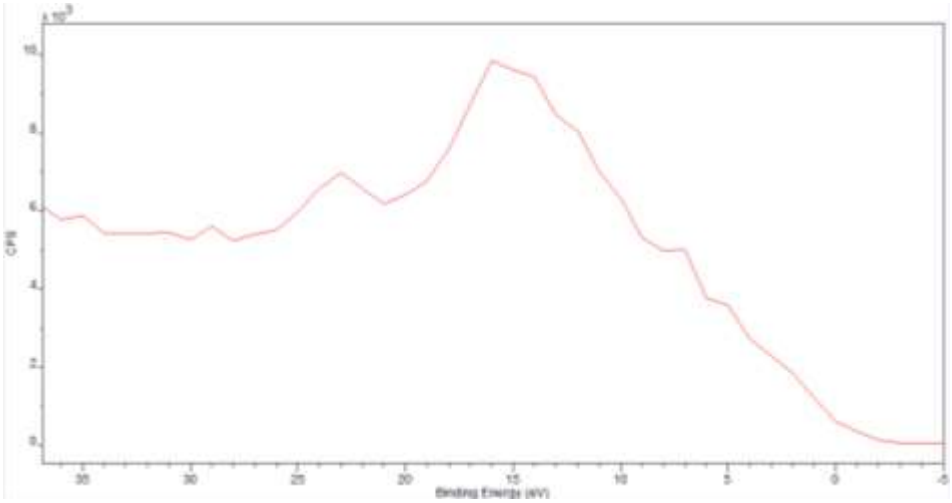

Figure 4.11. XPS spectrum of DLC coating at low-binding energy regime.

4.2.2 Mechanical Properties

The hardness and Young's modulus values of the DLC coatings are shown in Table 4.2. The value of ν was taken as 0.30 [153]. The DLC coatings shows high hardness and high H/E* and H^3/E^{*2} ratios. This is because of its relatively high percentage of sp^3 bonding.

Table 4.2. Hardness and Young's modulus of DLC coatings.

Sample	**Hardness-H (GPa)**	**Young's Modulus-E (GPa)**	**H/E***	**H^3/E^{*2} (GPa)**
DLC	15.8 ± 0.1	138.7 ± 10.4	0.10	0.17

4.2.3 Cross-Sectional Morphology

The cross-sectional images of the DLC coatings deposited on CrN interlayers observed by FESEM are shown in Figure 4.12. Figure 4.12 (a) shows DLC on CrN-1 while Figure 4.12 (b) shows DLC on CrN-4. It can be seen that the DLC coatings on CrN-4 is more connected and better diffused into the CrN layer as compared to DLC on CrN-1.

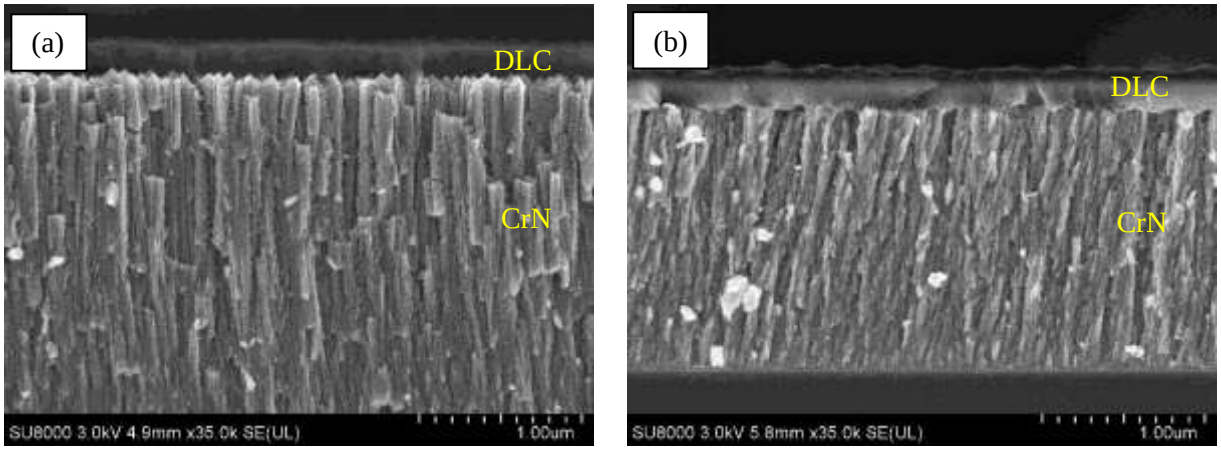

Figure 4.12. Cross-sectional FESEM images of DLC coatings on (a) CrN-1, (b) CrN-4.

4.2.4 Adhesion

Figure 4.13 shows the SEM images of DLC on SS substrate with CrN interlayers after Rockwell C indentation testing. Spallation and cracking of the coatings are observed around the imprint in all of the samples except DLC on CrN-4, indicating DLC has the highest adhesion to CrN-4. DLC coatings on CrN interlayers deposited at a low pressure of 3 mTorr (CrN-2, 3, 6 and 8) show the worst adhesion. As CrN-4 and CrN-7 were deposited under similar deposition conditions with similar thickness except for different sputtering power, DLC on both samples show good adhesion and therefore, DLC on CrN-7 is not shown here.

The effect of the structure and properties of CrN interlayers on DLC adhesion to CrN interlayered SS substrates can be explained by the mechanical properties and structural characteristics of the CrN interlayers.

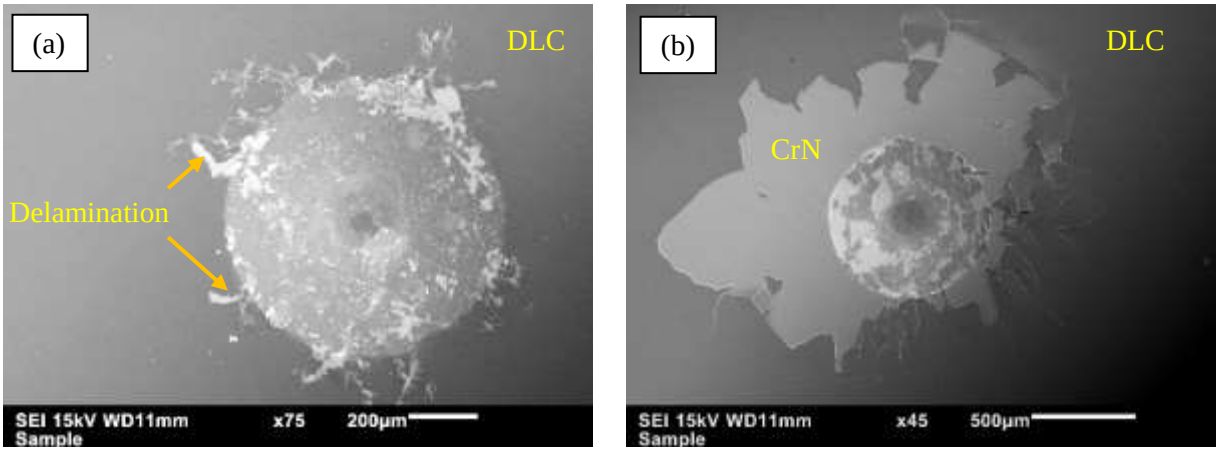

Figure 4.13. SEM images after Rockwell C indentation of DLC on SS substrate with (a) CrN-1, (b) CrN-2, (c) CrN-3, (d) CrN-4, (e) CrN-5, (f) CrN-6 and (g) CrN-8 as an interlayer.

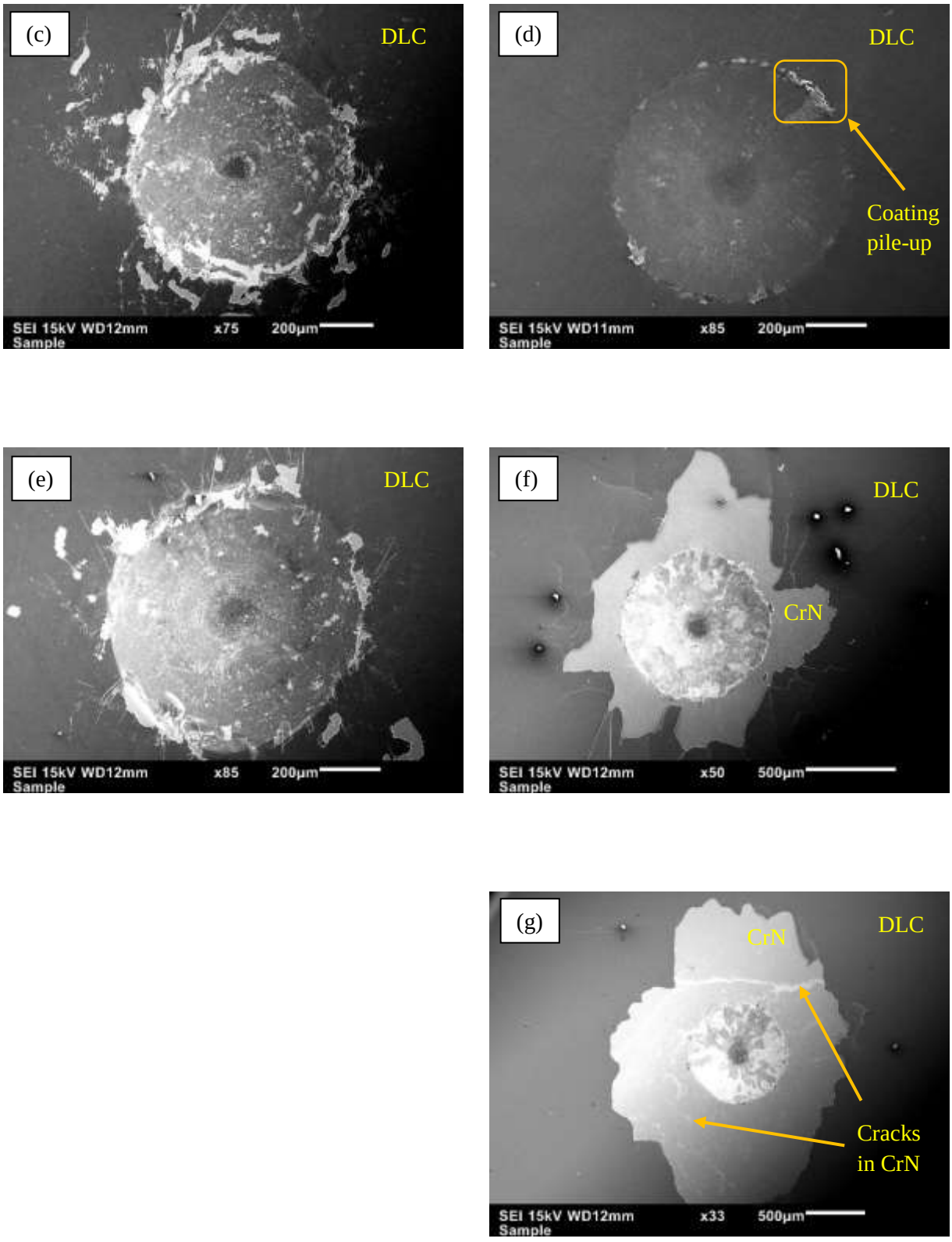

Figure 4.13. SEM images after Rockwell C indentation of DLC on SS substrate with (a) CrN-1, (b) CrN-2, (c) CrN-3, (d) CrN-4, (e) CrN-5, (f) CrN-6 and (g) CrN-8 as an interlayer.

4.2.4.1 Mechanical Properties

The DLC shows very poor adhesion to bare SS substrate. This is because of the huge mismatch of their mechanical properties. The SS is soft with a hardness of about 4 GPa. When a load is applied to the hard DLC coated SS, the SS deforms significantly while the DLC coating with a high hardness of about 16 GPa has little deformation, inducing high stress at the interface and resulting in coating delamination or severe cracking. To reduce this huge mechanical mismatch, a CrN interlayer is incorporated. In order to reduce the mechanical mismatch, the deposited CrN interlayer should have a hardness between the DLC coating and the SS substrate. However, the CrN layers deposited under different parameters show different structures and hence different mechanical properties. CrN interlayers deposited at room temperature (CrN-1 and 2) have a porous structure and are very soft, and thus cannot reduce the interfacial stress induced by the mechanical property mismatch when a load is applied. Similarly, CrN layers deposited at high temperatures and low working pressures such as CrN-6 and CrN-8 have a high hardness of 12 GPa, close to that of DLC, and high compressive stresses. When a load is applied, the interface between the CrN and SS would fail, resulting in poor adhesion. CrN-4 and CrN-7 demonstrate a hardness of approximately 8 GPa, which is between DLC and the SS, and thus the DLC coating on them shows much improved-adhesion.

Another reason for poor DLC adhesion on the SS is the absence of any kind of mechanical or chemical interaction between the two. A porous CrN interlayer can solve this problem by providing a mechanical interlocking. CrN-4 shows a net-like porous structure as shown in Fig. 4.7 (d), which results in a strong mechanical interlocking with DLC coating as shown above in Figure 4.12 (b). This interlocking enhances the interfacial adhesion between DLC and CrN, further increase the adhesion strength of DLC to the CrN interlayered SS substrate.

Figure 4.14 shows the XPS survey spectrum of DLC on CrN interlayer at the point of Rockwell C indent. Four elements were identified: carbon from DLC coating, Cr and N from the interlayer, and O due to the surface contamination. Figure 4.15 further shows the curve-fitted deconvoluted C1s XPS spectrum. Apart from C-C, C=C and C-O bondings as observed in DLC surface analysis, C-N bonding was also observed at 286.42 eV. The formation of this C-N bonds should be during DLC coating deposition. Carbon atoms, during the film growth, hit the surface with high energy. As a result, nitrogen from the CrN interlayer forms C-N bonds with the highly energetic carbon

atoms. This C-N bonding would further enhance the interfacial adhesion between DLC and the CrN interlayer.

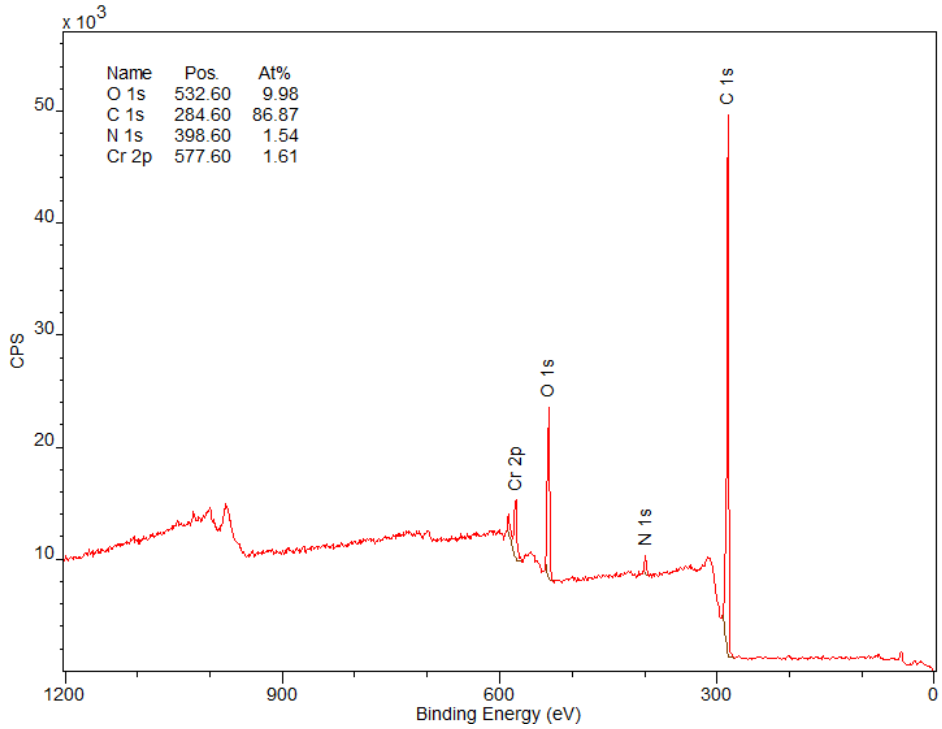

Figure 4.14. XPS survey spectrum of DLC surface at the point of Rockwell C indent.

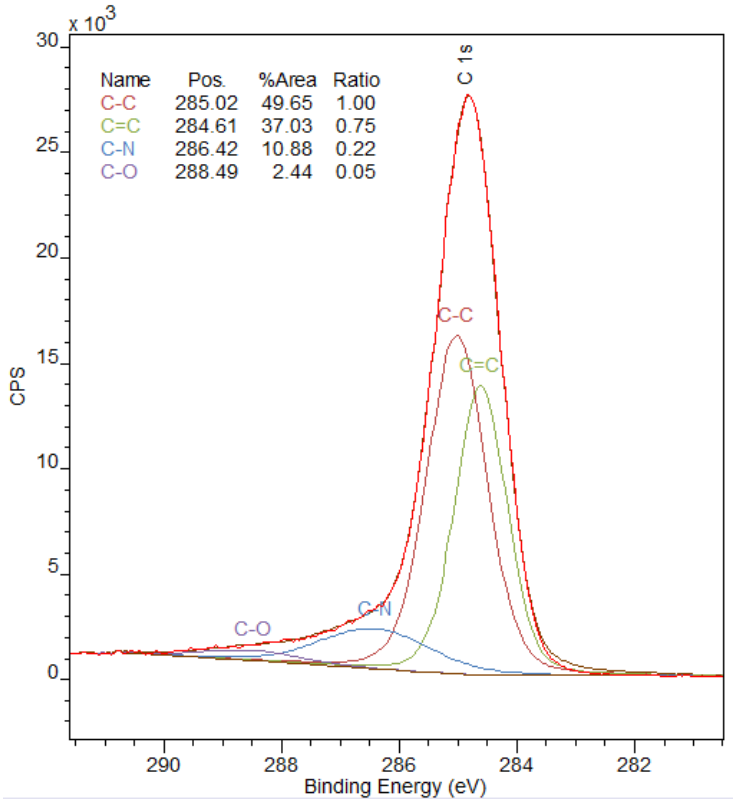

Figure 4.15. Deconvolution of C1s XPS spectrum of DLC coating at Rockwell C indent.

4.3 CrN Interlayer Thickness effect on DLC and NDLC Adhesion to 316L SS

This section is divided into two parts. The first section reports the effect of CrN interlayer thickness on DLC adhesion to 316L SS. The second section reports the effect of CrN interlayer thickness on NDLC adhesion to the SS. In this research, CrN-4 that showed the best adhesion for DLC was deposited on SS for different durations as an interlayer followed by the deposition of DLC and NDLC coatings. Rockwell C indentation tests were then done to the DLC samples and the imprints were observed using SEM to evaluate the adhesion.

4.3.1 CrN Interlayers

CrN-4 was deposited for 1, 2, 4, 6 and 10 hours on 316L SS. The thickness was measured using optical profilometer and was confirmed by SEM. Moreover, surface profilometry was done to measure the RMS roughness values of the as-deposited CrN interlayers. The chemical, structural and mechanical characterization of the CrN interlayers is shown in section 4.1.

Figure 4.16 shows the thickness of CrN interlayers deposited by RF magnetron sputtering for 1, 2, 4, 6 and 10 hours. The thickness increases from 400 nm to 2 μm when increasing the deposition time from 1 to 10 hours.

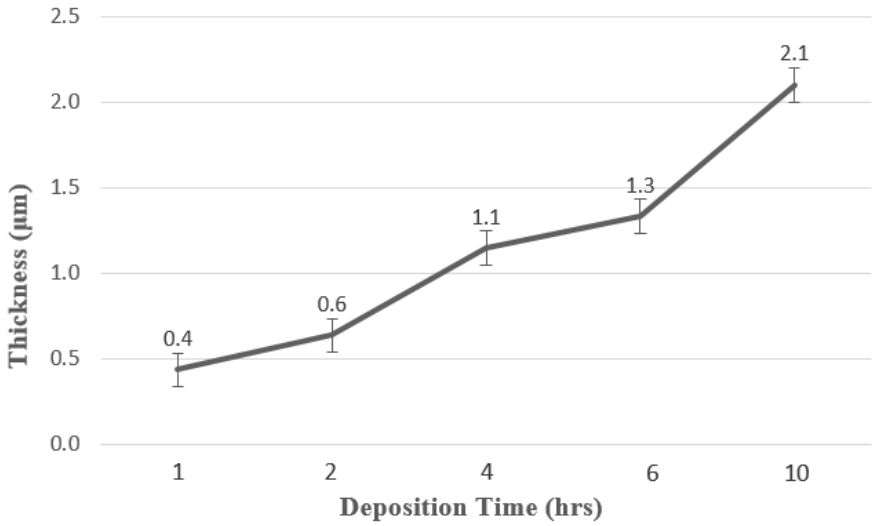

Figure 4.16. The thickness of CrN interlayers deposited for different durations.

The root mean squared (RMS) roughness values of the CrN interlayers deposited for different durations is shown in Figure 4.17. The RMS roughness increases from 4.9 nm to 14 nm with the film thickness increasing from 0.4 to 2.1 μm.

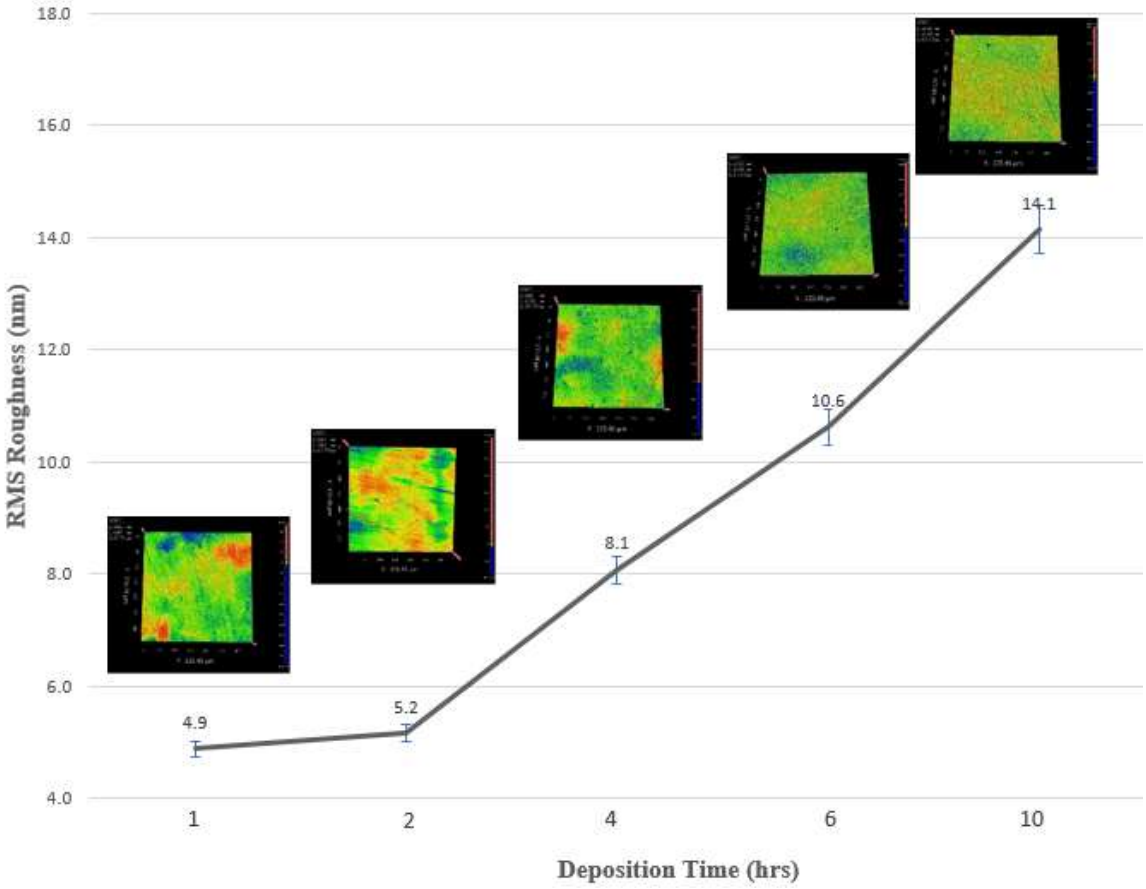

Figure 4.17. RMS Surface Roughness of CrN interlayers on AISI 316L substrate.

4.3.2 DLC Adhesion on CrN Interlayered SS

Following the CrN interlayer deposition, DLC was deposited on the interlayered SS with an approximate thickness of 500 nm. An optical profilometer was used to measure the RMS surface roughness after DLC coating deposition and is shown in Figure 4.18. It can be seen that the RMS roughness increases after DLC deposition and also increases with the increase of CrN interlayer thickness. This increase in surface roughness is due to the increased roughness of the CrN interlayers and the existence of C-H dangling bonds on the surface in DLC. The chemical and mechanical characterization of as-deposited DLC coatings is similar to that of the DLC investigated in the previous section.

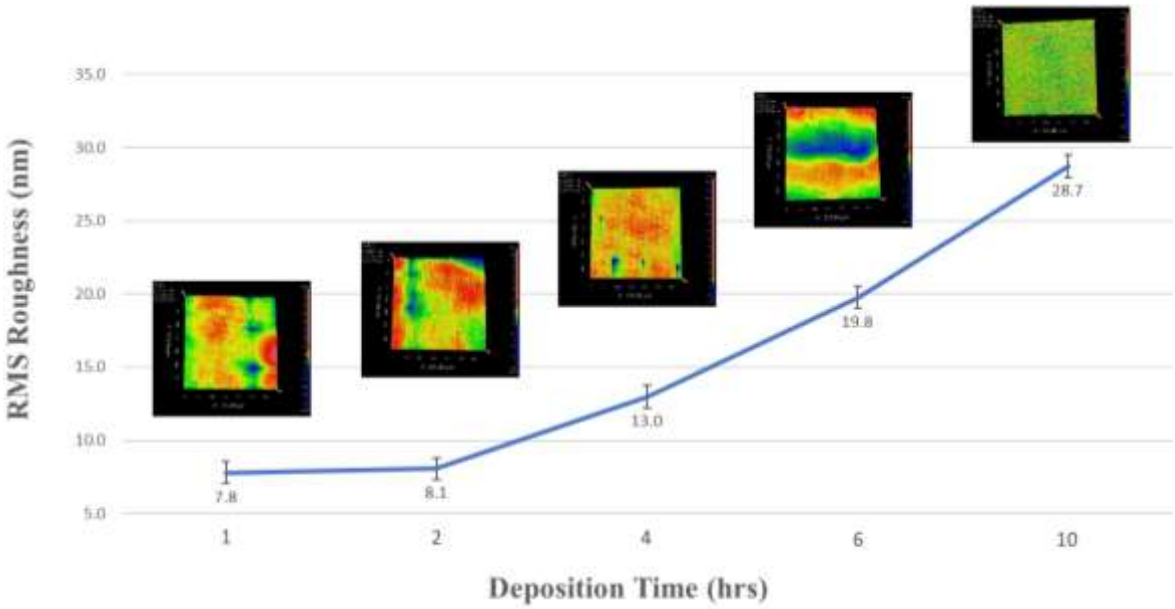

Figure 4.18. RMS surface roughness of DLC coatings deposited on SS with CrN interlayer of varying thicknesses.

Figure 4.19 shows the SEM images of DLC on SS with CrN interlayers of different thicknesses after Rockwell C indentation testing. Spallation on a large area can be seen for interlayer with 400 nm thickness. The spallation area reduces as the interlayer thickness increases and the best adhesion was seen for a 2.1 μm thick CrN interlayer in which no spallation nor cracks have been observed. This result indicates that the interlayer needs sufficient thickness in order to strongly support the DLC coating.

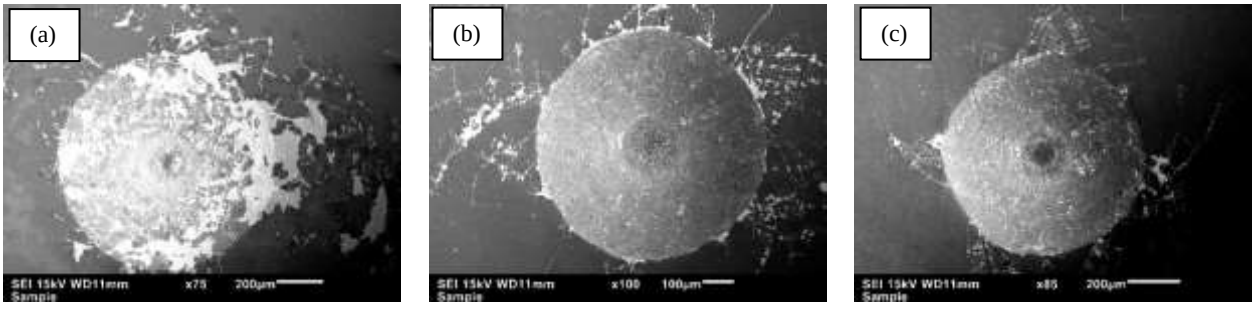

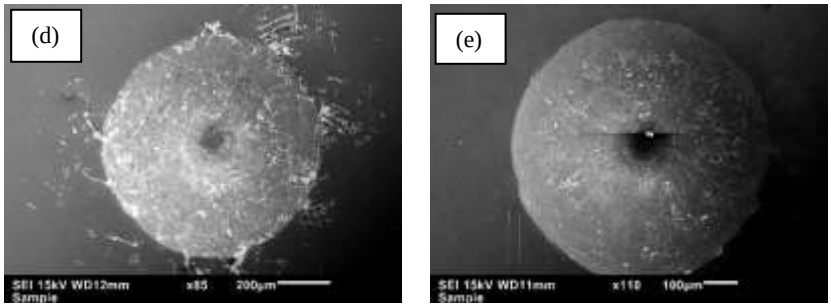

Figure 4.19. SEM images after Rockwell C indentation of DLC coatings on stainless substrate with CrN interlayer deposited for (a) 1, (b) 2, (c) 4, (d) 6 and (e) 10 hours.

4.3.3 NDLC on 316L SS with CrN Interlayer of Different Thicknesses

The CrN interlayers for NDLC deposition were the same as for DLC deposition described in the previous section. After CrN deposition on SS substrate, NDLC coatings were deposited by introducing 1 sccm of N_2 gas during DLC deposition. The chemical analysis of NDLC thin coatings were done using Raman spectroscopy and XPS, the RMS surface roughness was measured using optical profilometry and the mechanical properties were determined using nanoindentation testing. The thickness of NDLC is approximately 500 nm. Rockwell C indentation tests were done on the NDLC coated samples and the imprints were observed using SEM to evaluate the coating adhesion.

4.3.3.1 Structural Characterization

The Raman spectrum obtained from the as-deposited NDLC on the CrN interlayered SS substrate is shown in Figure 4.20. The broad peaks confirm the amorphous nature of the coatings. I_D/I_G ratio of 0.98 was observed, indicating a reduction of sp^3 percentage in the NDLC coatings compared to the DLC coatings. This result demonstrates that N doping promotes sp^2 bonding in DLC coatings, consistent with a previous report [129].

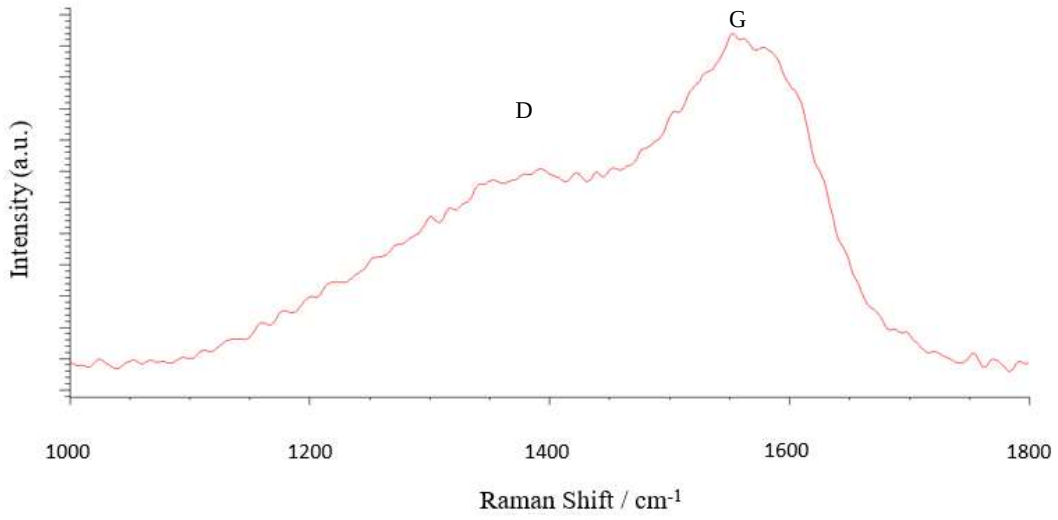

Figure 4.20. Raman spectrum of NDLC.

XPS was done to determine the chemical composition and the bonding state of the NDLC. Survey XPS conducted on the surface of the coating shows the presence of about 8.3 at.% nitrogen in the film and oxygen was identified as an impurity. Figure 4.21 shows a curve-fitted C1s XPS spectrum of the NDLC. The deconvolution was done by the Gausian-Lorentzian function using CasaXPS software. In contrast to DLC, the highest peak seen at 284.47 eV corresponds to C=C bonding, indicating a higher sp^2 concentration in the NDLC coating. The peak corresponding to sp^3 bonding was seen at 285 eV. Another peak at 286.20 eV appears, which can be attributed to C-N bonding. Considering the area ratio of the sp^3 to sp^2 peaks, the sp^2/sp^3 ratio of the NDLC coating is calculated to be 1.08. This further confirms that nitrogen doping decreases sp^3 C-C concentration. Similarly, a shoulder at 287.77 eV was observed because of the O contamination on the surface [151,152].

The root mean squared (RMS) roughness values of the NDLC thin coatings deposited on CrN interlayers with different thicknesses is shown in Figure 4.22. We can see the NDLC coatings have lower RMS roughness values as compared to DLC coatings deposited on CrN interlayers of the same thickness. This is because nitrogen doping reduces the C-H dangling bonds and consequently decreases surface roughness [158].

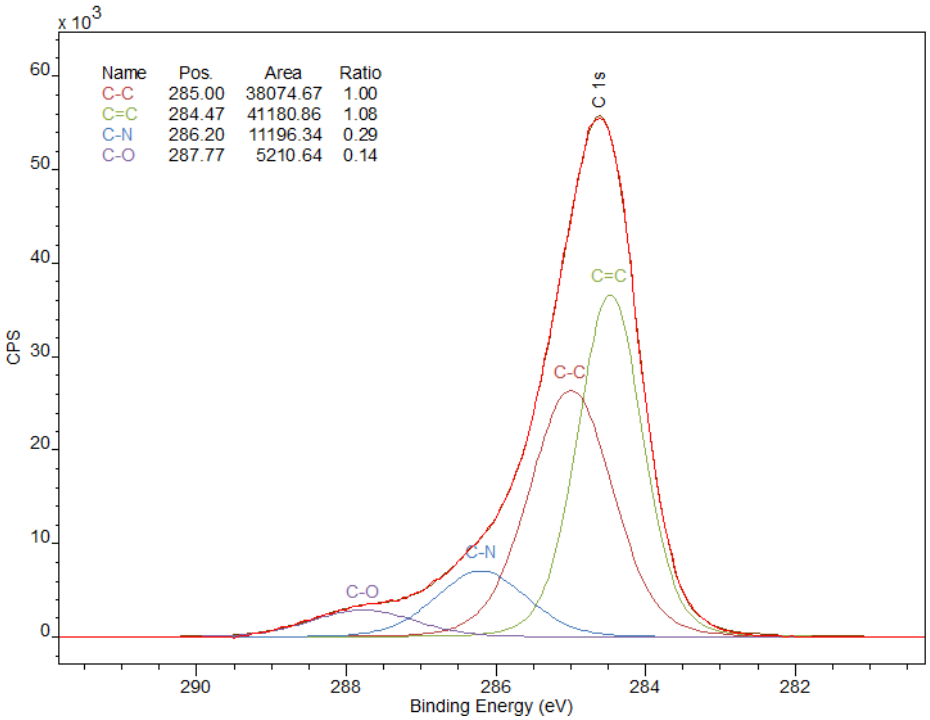

Figure 4.21. Deconvolution of C1s XPS spectrum of NDLC.

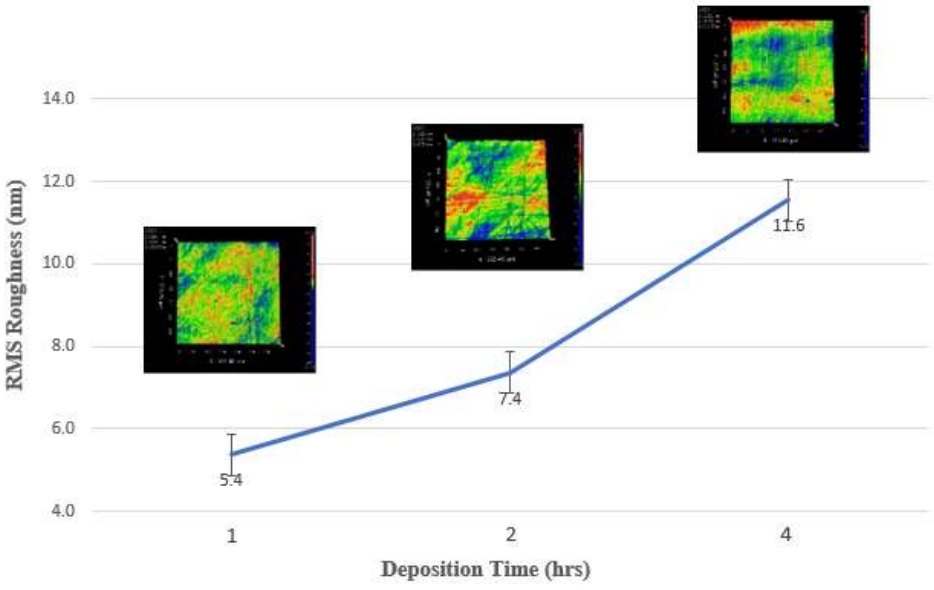

Figure 4.22. RMS surface roughness of NDLC coatings deposited on CrN interlayers with varying thicknesses.

The hardness and Young's modulus values of the NDLC are shown in Table 4.3. A drop in the hardness and its corresponding H/E* and H^3/E^{*2} values is because of the decreased sp^3 bonds due to the N doping as observed in its Raman and XPS spectra.

Table 4.3. Hardness and Young's modulus of NDLC coatings.

Sample	**Hardness-H (GPa)**	**Young's Modulus-E (GPa)**	**H/E***	**H^3/E^{*2} (GPa)**
NDLC	11.5 ± 0.1	141.7 ± 5.6	0.075	0.064

Figure 4.23 shows the SEM images of NDLC coatings after Rockwell C indentation testing. Little spallation or cracking of the films is observed surrounding the imprint. NDLC on 400 nm thick CrN interlayer (Fig. 4.23(a)) showed the poorest adhesion with local spallation observed. However, comparing the DLC adhesion with the same interlayer thickness, the NDLC shows much less delamination and thus much higher adhesion. The adhesion of NDLC improved significantly when increasing the thickness of CrN interlayer to 600 nm (Fig. 4.23(b)) as little delamination was observed. And for an interlayer of 1μm thick (Fig. 4.23(c)), no delamination or crack is observed. The results show that excellent adhesion of DLC coatings to the SS substrate is achievable with a much thinner CrN interlayer by doping the DLC coating with nitrogen. This is because nitrogen doping promotes sp^2 formation in the coating, which reduces the average coordination number of the amorphous carbon network and significantly reduces the internal stress in the DLC coating.

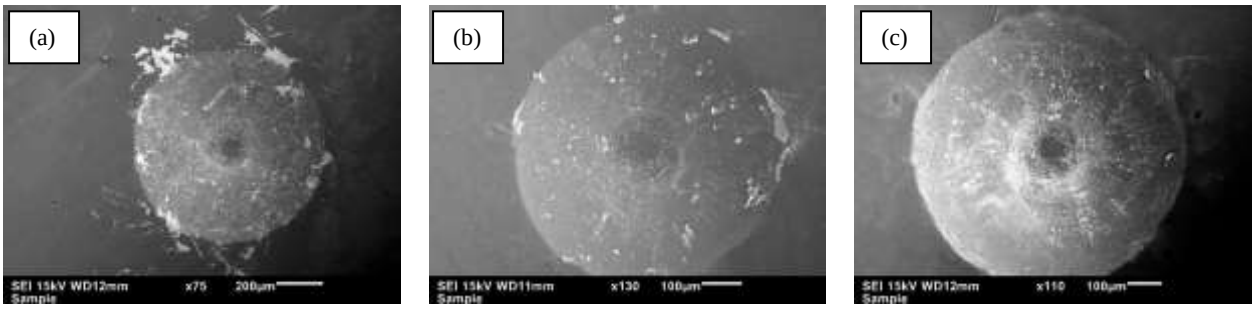

Figure 4.23. SEM images after Rockwell C indentation of NDLC coatings on SS substrate with CrN interlayer deposited for (a) 1, (b) 2 and (c) 4 hours.

The delamination of DLC coating is related to the stored elastic energy in the film. Failure occurs when this elastic energy reaches a critical value that is closely related to the critical film thickness. The adhesion enhancement with nitrogen doping can be explained using Griffith's law that is [154]:

$$\frac{h_f \sigma_f^2}{2E_f} \leq 2\gamma \tag{4.1}$$

where γ represents the surface fracture energy per unit area required to break the interface, the film thickness is represented by h_f, while σ_f and E_f are for compressive stress and elastic modulus in the film, respectively. Thin film delamination occurs when both sides of the equations are equal. The source of the compressive stress in the film is the energetic ion bombardment during the film deposition. With an increase in the stress, the elastic energy in the film also increases.

When the elastic energy exceeds the surface fracture energy, the shear force in the coating-substrate interface starts delamination of the coating. The improved adhesion of NDLC with thinner CrN interlayer comparing with DLC is because of the reduced internal stresses by nitrogen incorporation. Although the hardness of nitrogen doped DLC decreased, the increase in Young's modulus suggests that nitrogen doping allows elastic stretching of DLC coatings without exceeding the surface fracture energy.

This result indicates that the cooperation of CrN interlayer and nitrogen doping can significantly increase the DLC adhesion to 316L SS. The CrN interlayer provides a strong supporting base to DLC coatings while nitrogen doping reduces the internal stresses in DLC, both working together synergistically to enhance DLC adhesion.

4.4 Friction and Wear

A Ball-on-disk configuration was used to test the friction and wear of DLC and NDLC coatings which showed the best adhesion on SS substrate and using bare SS as the reference sample. All the samples were immersed in a saline solution (0.90% w/v of NaCl in distilled water) at room temperature. A constant load of 5 N was applied in a reciprocating motion at a constant speed of 5 mm/sec. A total of 5000 cycles was set to measure the coefficient of friction (COF) and the wear rate. 302 stainless steel balls of 4 mm diameter were used as the counter material and were moved

linearly with a wear track length of 2.5 mm. The wear area and the wear depth were measured by an optical profilometer to calculate the volume loss and wear rate of the specimens. The coating wear rate was calculated by the following equation [155]:

$$K=V/SF \quad (4.2)$$

where V is the wear volume in mm^3, S is the total sliding distance in meters and F is the load in Newtons. The wear rate depends on several factors, such as the structure and hardness of the coating, coating thickness and roughness, and the adhesion strength to the substrate. To make the results comparable, both the CrN interlayer thickness and the DLC and NDLC coating thickness were kept the same.

The measured COF values are shown in Table 4.4. Bare steel demonstrated the highest COF value of 1.30 and DLC coated steel had lowest COF value of 1.02. The NDLC had a COF value between the bare steel and DLC. A much lower COF value was expected for NDLC because of its increased sp^2 bonding, as reported in previous researches. The graph of COF value with time shows that at the start of the test the COF value for NDLC was as low as 0.8, that increased as the test proceeded. The reason for this increase in COF value for NDLC is the high wear rate of NDLC coating as the thin NDLC coating was worn out fast and the interlayer exposed after a while and finally the SS substrate exposed with a high value of COF. DLC coating, on the other hand, was not worn out during the testing and thus its COF value is relatively stable.

Table 4.4. The coefficient of friction of AISI 316L, DLC and NDLC coating against AISI 302 balls.

Sample	**COF**
Bare SS 316L	1.30 ± 0.05
DLC/CrN coated Steel	1.02 ± 0.05
NDLC/CrN coated Steel	1.10 ± 0.05

Figure 4.24 shows the images of the wear tracks observed by the optical profilometer. The wear depth of all three specimens is shown in Table 4.5. Bare steel specimen showed the highest volume loss and the wear depth was 10 μm. The second highest material loss was shown by NDLC with 3 μm wear depth and the DLC coated SS showed the lowest volume loss after the wear test with a wear depth of 0.9 μm. The wear rates calculated by equation 4.2 are shown in Table 4.6. As expected, the wear rates observed are inversely related to the measured hardness and H/E* and H^3/E^{*2} values of the specimens. DLC coated SS had the lowest wear rate because of its highest hardness of 16 GPa and the highest H/E* and H^3/E^{*2} values of 0.10 and 0.17, respectively.

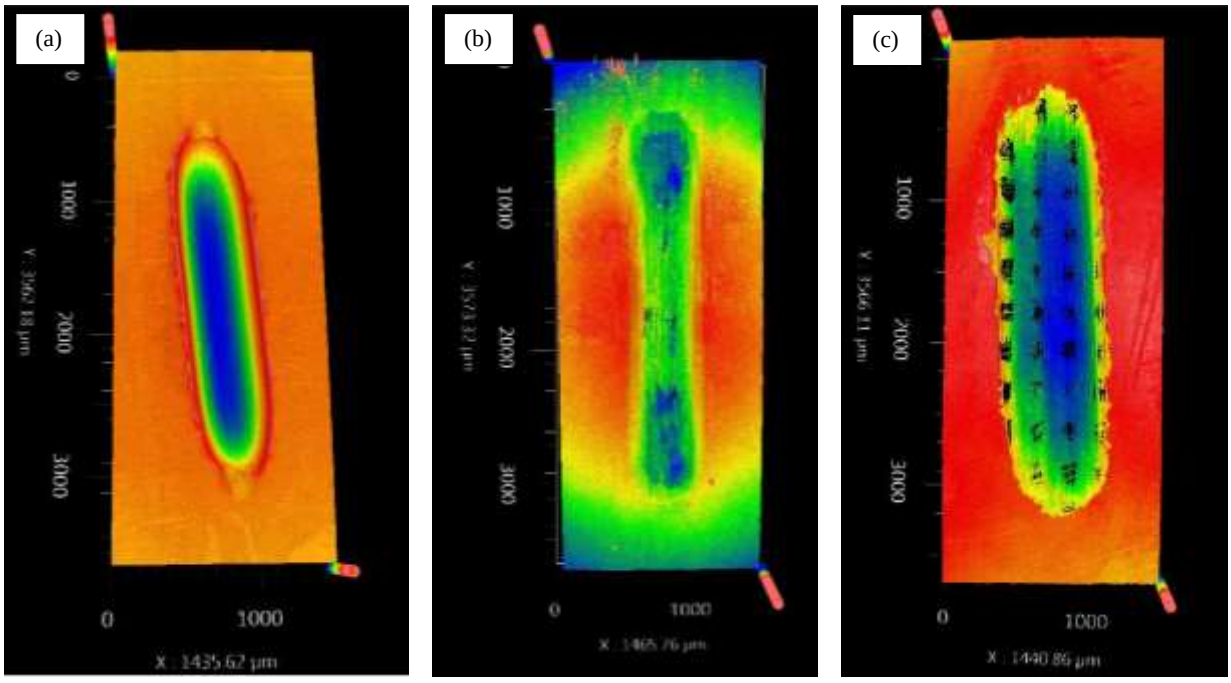

Figure 4.24. Optical profilometer images of the wear tracks of (a) bare steel, (b) DLC and (c) NDLC.

Table 4.5. Wear depth values for bare AISI 316L, DLC and NDLC coatings.

Sample	**Wear Depth / µm**
Bare SS 316L	10 ± 0.1
DLC/CrN coated Steel	0.9 ± 0.1
NDLC/CrN coated Steel	3 ± 0.1

Table 4.6. Average wear rate values for AISI 316L, DLC and NDLC against AISI 302 ball.

Sample	**Average Wear Rates ($x10^{-5}$ mm^3/Nm)**
Bare SS 316L	3.6 ± 0.2
DLC/CrN coated SS	0.4 ± 0.1
NDLC/CrN coated SS	2.1 ± 0.1

In order to understand this chapter and have a clear picture of the experiments and results, a summary of samples and the results are presented in Figure 4.25.

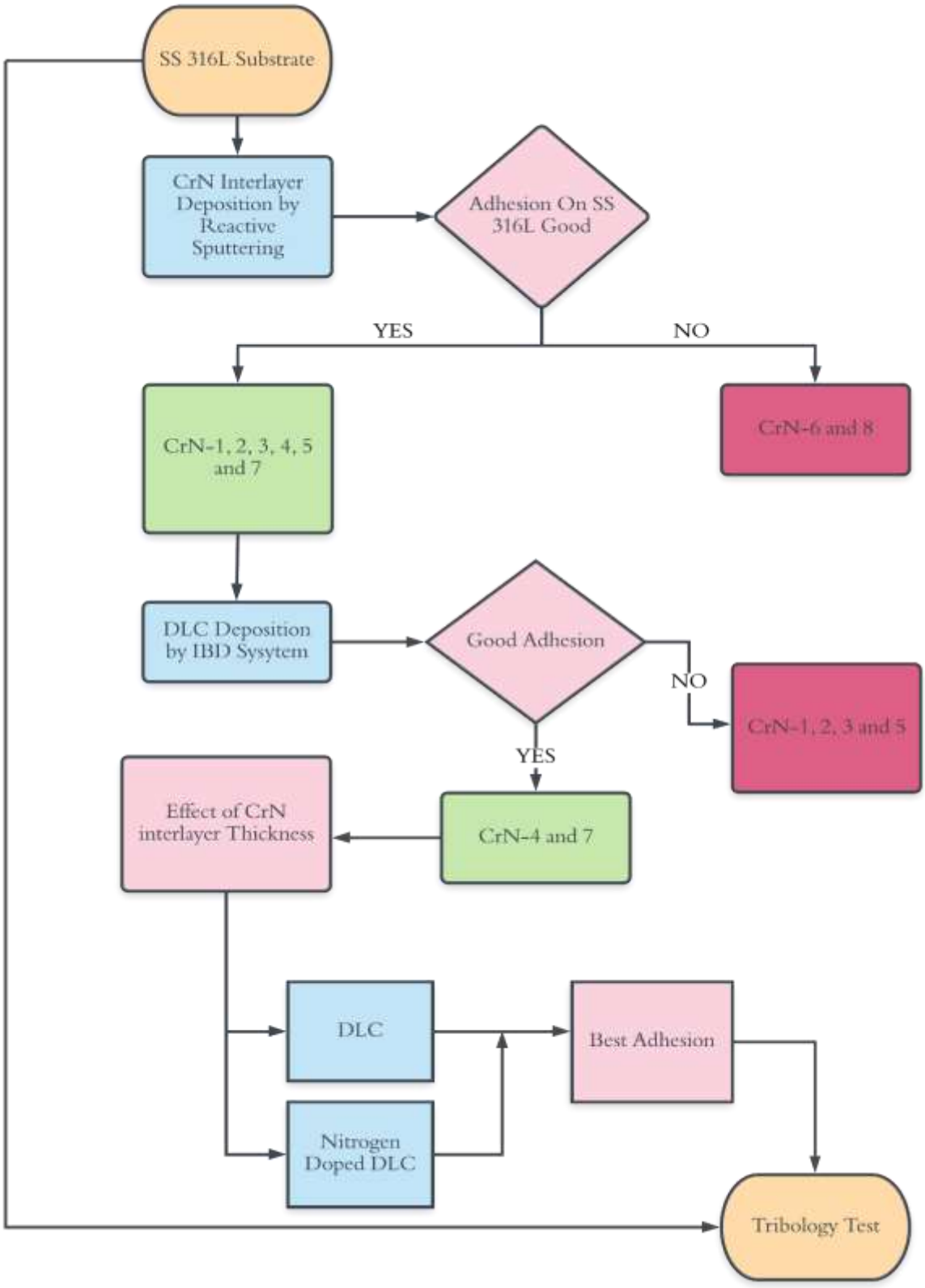

Figure 4.25. Summary of experiments and results.

CHAPTER 5
CONCLUSIONS AND FUTURE WORK RECOMMENDATIONS

5.1 Conclusions

CrN was used as an interlayer to enhance DLC adhesion to 316L stainless steel. CrN thin layers with different microstructure and thickness were firstly deposited on a 316L stainless steel substrate by RF magnetron sputtering with varied deposition parameters. DLC and nitrogen doped DLC coatings were then deposited on the CrN interlayered SS substrate by IBD. The structure and properties of the resulted coated samples were analyzed and evaluated by various characterization techniques. The results and conclusions are summarized as follows:

1. The microstructure and properties of CrN thin layers deposited by RF sputtering can be tailored by changing the deposition parameters. The CrN layers deposited at room temperature have a porous structure with low hardness values whereas the layers deposited at elevated temperature show a dense columnar structure with increased hardness. Moreover, decreasing deposition pressure increases the hardness of CrN layers.
2. DLC coatings demonstrate the best adhesion on SS substrate with CrN interlayer deposited at relatively high temperature and high pressure showing a net-like structure.
3. DLC adhesion increases with the increase of CrN interlayer thickness as a thicker interlayer would decrease soft substrate effect upon loading.
4. Doping DLC coatings with nitrogen reduce intrinsic stresses in DLC by decreasing sp^3 bonds which result in reduced hardness but good adhesion with a thinner CrN interlayer.
5. DLC coated SS samples demonstrates the lower value of COF and lower wear rates compared to the bare steel and therefore, are promising for enhancing tribological properties of the stainless steel.

5.2 Future Work

The present thesis studies have demonstrated that CrN interlayer can enhance DLC adhesion to 316L SS substrate and the DLC coated steel samples with a CrN interlayer show increased tribological properties. These promising results demand more systematic research. The following future work is suggested:

1. Investigate the effect of substrate bias on the microstructure and mechanical properties of CrN layers.
2. Study the interface between DLC and CrN interlayer by transmission electron microscope to understand the interfacial bonding mechanism.
3. Deposit both DLC and CrN interlayer in one single deposition process.
4. Evaluate and analyze the corrosion and tribicorrosion resistance of the coated samples by comparing with the uncoated ones.

REFERENCES

1. Jost H.P. (ed.). Lubrication (Tribology)–A report on the present position and industry's needs. Department of Education and Science, H. M. Stationary Office, London, UK, 1966.
2. Holmberg K., Erdemir A. Influence of tribology on global energy consumption, costs and emissions. 2017;5(3):263-284.
3. Lee P.M., Carpick R. (eds). Tribological opportunities for enhancing America's energy efficiency. A report to the Advanced Research Projects Agency-Energy (ARPA-E) at the U.S. Department of Energy, 14.2.2017.
4. IEA Energy Technology Persectives 2010. Scenarios & Strategies to 2050 IEA International Energy Agency, Paris, France 2010.
5. Holmberg K., Andersson P., Erdemir A. Global energy consumption due to friction in passenger cars. Tribology International 47: 221–234 (2012)
6. Dong, F.Y., Zhang P., Pang J.C., Chen D.M., Yang K., and Zhang Z.F. (2013). Optimizing strength and ductility of austenitic stainless steels through equal-channel angular pressing and adding nitrogen element. Materials Science and Engineering A, 587(C), 185-191.
7. Lin L., Chen S., Wu C., Hung J., Ou K. Applied Surface Science Microstructure and antibacterial properties of microwave plasma nitrided layers on biomedical stainless steels. Appl Surf Sci. 2011;257(17):7375-7380. doi:10.1016/j.apsusc.2011.01.065
8. Lo K., Shek C. and Lai J. "Recent Developments in Stainless Steels." Materials Science and Engineering R: Reports 65, no. 4-6 (2009): 39-104.
9. Yasumaru N. "Low Temperature Ion Nitriding of Austenitic Stainless Steels." Nippon Kinzoku Gakkaishi/Journal of the Japan Institute of Metals 61, no. 5 (1997): 424-29.
10. Bell T. "Surface Engineering of Austenitic Stainless Steel." Surface Engineering 18, no. 6 (2002): 415-22.
11. Xu J., Zhuo C., Tao J., Jiang S., and Liu L. (2009). Improving the corrosion wear resistance of AISI 316L stainless steel by particulate reinforced Ni matrix composite alloying layer. Journal of Physics D: Applied Physics, 42(1), 12.
12. Dong H., Qi P.Y., Li X.Y. and Llewellyn R.J. 2006 Improving the erosion–corrosion resistance of AISI 316 austenitic stainless steel by low-temperature plasma surface alloying with N and C Mater. Sci. Eng. A 431 137–45

13. Dogan H., Findik F., and Morgul O. Friction and wear behaviour of implanted AISI SS 316L and comparison with a substrate. Mater Des 2002;23(7):605–10.
14. Kurgan N. Effect of porosity and density on the mechanical and microstructural properties of sintered 316L stainless steel implant materials. Mater Des. 2014;55:235-241. doi:10.1016/j.matdes.2013.09.058
15. Muley S., Vidvans A., Chaudhari G., Udainiya S. An assessment of ultra fine grained 316L stainless steel for implant applications. Acta Biomater. 2016;30:408-419. doi:10.1016/j.actbio.2015.10.043
16. Guemmaz M., Mosser A., Grob J., Stuck R. Sub-surface modifications induced by nitrogen ion implantation in stainless steel (SS316L). Correlation between microstructure and nanoindentation results. Surface and Coatings Technology. 1998;100-101:353-357. doi:10.1016/s0257-8972(97)00647-6
17. Wei P., Lein S., Chin S., and Jinn S. Boron- a doped Si grown by ultra-high vacuum chemical vapor deposition. Mater Chem Phys 2002;77:426–9.
18. Zhang T.C. and Li D.Y. 2000 An experiment study on the erosion behavior of pseudoelastic TiNi alloy in dry sand and in aggressive media Mater. Sci. Eng. A 293 208–14.
19. Holmberg K. and Matthews A. Coatings Tribology–Properties, Mechanisms, Techniques and Applications in Surface Engineering. Elsevier Tribology and Interface Engineering Elsevier Series. Amsterdam, the Netherlands: Elsevier; 2009.
20. Skolek-Stefaniszyn E., Kaminski J., Sobczak J., Wierzchon T. Modifying the properties of AISI 316L steel by glow discharge assisted low-temperature nitriding and oxynitriding. Vacuum. 2010;85(2):164-169. doi:10.1016/j.vacuum.2010.05.006
21. Skolek-Stefaniszyn E., Burdynska S., Mroz W., Wierzchon T. Structure and wear resistance of the composite layers produced by glow discharge nitriding and PLD method on AISI 316L austenitic stainless steel. Vacuum. 2009;83(12):1442-1447. doi:10.1016/j.vacuum.2009.05.024
22. Sun, Y., X. Li, and T. Bell. "Structural Characteristics of Low Temperature Plasma Carburised Austenitic Stainless Steel." Materials Science and Technology 15, no. 10 (1999): 1171-178.

23. Ceschini L., Minak G. Fatigue behaviour of low temperature carburised AISI 316L austenitic stainless steel. Surface and Coatings Technology. 2008;202(9):1778-1784. doi:10.1016/j.surfcoat.2007.07.066
24. Kayali Y., Büyüksağiş A., Yalçin Y. Corrosion and wear behaviors of boronized AISI 316L stainless steel. Metals and Materials International. 2013;19(5):1053-1061. doi:10.1007/s12540-013-5019-x
25. Steckelmacher W. "Coatings Tribology: Properties, Techniques and Applications in Surface Engineering: Kenneth Holmberg and Allan Matthews Tribology Series, Vol 28 (edited by D Dowson). Elsevier Science, Amsterdam, 1994. ISBN 0-444-88870-5, 442 Pp. Price Dfl 285.00; $163.00." Vacuum 46, no. 1 (1995): 88.
26. Robertson J. "Diamond-like Amorphous Carbon." Materials Science & Engineering R 37, no. 4 (2002): 129-281.
27. Erdemir A., Donnet C. Tribology of diamond-like carbon films: recent progress and future prospects. J Phys D Appl Phys. 2006;39(18):R311-R327. doi:10.1088/0022-3727/39/18/r01
28. Michler T., and C. Siebert. "Abrasive Wear Testing of DLC Coatings Deposited on Plane and Cylindrical Parts." Surface & Coatings Technology 163 (2003): 546-51.
29. Donnet C., Erdemir A. editor, & SpringerLink. (2008). Tribology of Diamond-Like Carbon Films : Fundamentals and Applications.
30. Forsich C., Heim D., Mueller T. 2008. Influence of the deposition temperature on mechanical and tribological properties of a-C:H:Si coatings on nitride and postoxided steel deposited by DC-PACVD. Surface and Coating Technology 203, 521-525.
31. Erdemir A., Donnet C., 2006. Tribology of diamond-like carbon films: recent progress and future prospects. Journal of Physics D: Applied Physics 39, R311-R327.
32. Ueda N., Yamauchi N., Sone T., Okamoto A., Tsujikawa M. 2007. DLC film coating on plasma carburized austenitic stainless steel. Surface and Coating Technology 201, 5487-5492.
33. Li X. (2001). Joint Second Prize Low Temperature Plasma Nitriding of 316 Stainless Steel – Nature of S Phase and Its Thermal Stability. Surface Engineering, 17(2), 147-152.

34. Skolek-Stefaniszyn E., Kaminski J., Sobczak J., Wierzchon T. Modifying the properties of AISI 316L steel by glow discharge assisted low-temperature nitriding and oxynitriding. Vacuum. 2010;85(2):164-169. doi:10.1016/j.vacuum.2010.05.006
35. Li Y., Wang Z., Wang L. Surface properties of nitrided layer on AISI 316L austenitic stainless steel produced by high temperature plasma nitriding in short time. Appl Surf Sci. 2014;298:243-250. doi:10.1016/j.apsusc.2014.01.177
36. Cheng Y., Browne T., Heckerman B. Mechanical and tribological properties of CrN coatings deposited by large area filtered cathodic arc. Wear. 2011;271(5-6):775-782. doi:10.1016/j.wear.2011.03.011
37. Hones P., Sanjines R., Levy F. Characterization of sputter-deposited chromium nitride thin films for hard coatings. Surface and Coatings Technology. 1997;94-95:398-402. doi:10.1016/s0257-8972(97)00443-x
38. Ehiasarian. A, Hovsepian P., Hultman L., Helmersson U. Comparison of microstructure and mechanical properties of chromium nitride-based coatings deposited by high power impulse magnetron sputtering and by the combined steered cathodic arc/unbalanced magnetron technique. Thin Solid Films. 2004;457(2):270-277. doi:10.1016/j.tsf.2003.11.113
39. Wang Q., Kwon S., Kim K. Formation of nanocrystalline microstructure in arc ion plated CrN films. Transactions of Nonferrous Metals Society of China. 2011;21:s73-s77. doi:10.1016/s1003-6326(11)61064-9
40. Producers C of SS. Review of the wear and galling characteristics of stainless steels. A Des Handb Ser. 1978.
41. Hall E., Briant C. Chromium depletion in the vicinity of carbides in sensitized austenitic stainless steels. Metallurgical Transactions A. 1984;15(5):793-811. doi:10.1007/bf02644554
42. Watson S.W., Friedersdorf F.J., Madsen B.W., Cramer S.D. (1995). Methods of measuring wear-corrosion synergism. Wear, 181(2), 476-484.
43. ASM Metals Handbook, 10th edition. Materials Park, OH : ASM International, 1995.
44. Page T. (1993). Materials for tribology: William A. Glaeser. Tribology International, 26(3), 218-219.

45. Srinivasan A., and Rajendran N. (2015). Surface characteristics, corrosion resistance and MG63 osteoblast-like cells attachment behaviour of nano SiO2 ZrO2 coated 316L stainless steel. RSC Advances, 5(33), 26007-26016.
46. Savarino L. E., Stea S., Granchi D., Visentin M., Ciapetti G., Donati M., Toni A. (2000). Sister chromatid exchanges and ion release in patients wearing fracture fixation devices. Journal of Biomedical Materials Research, 50(1), 21-26.
47. Sheldon G. L., "Effects of Surface Hardness and Other Material Properties on Erosive Wear of Metals by Solid Particulates," Journal of Engineering Materials and Technology, April 1977, pp. 133-137.
48. Rieker C., D. G. Morris, and J. Steffen. "Formation of Hard Microcrystalline Layers on Stainless Steel by Laser Alloying." Materials Science and Technology 5, no. 6 (1989): 590-94.
49. Peterson M.B., "Wear Testing Objectives and Approaches," ASTM Symposium, New Orleans, LA., STP 615, November, 1975.
50. Anon, 1970. Bonding dry film lubricants: PAULUS, G. Machine Design, Vol 41, No 30 (Dec 1969) pp 68–73. Tribology, 3(2), p.122.
51. Tassin C., Laroudie F., Pons M., Lelait L. Improvement of the wear resistance of 316L stainless steel by laser surface alloying. Surf Coatings Technol. 1996;80(1-2):207-210. doi:10.1016/0257-8972(95)02713-0
52. Michal G.M., Ernst F., Kahn H., Cao Y., Oba F., Agarwal N., Heuer A.H. "Carbon Supersaturation Due to Paraequilibrium Carburization: Stainless Steels with Greatly Improved Mechanical Properties." Acta Materialia 54, no. 6 (2006): 1597-606.
53. Asgari M., Barnoush A., Johnsen R., Hoel R. Microstructural characterization of pulsed plasma nitrided 316L stainless steel. Mater Sci Eng A. 2011;529(1):425-434. doi:10.1016/j.msea.2011.09.055
54. Pichon L., Cormier J., Declemy A., Chollet S., Villechaise P., Dubois B., and Templier C. (2013). Plasma nitriding response at 400 °C of the single crystalline Ni-based superalloy MC2. Journal of Materials Science, 48(4), 1585-1592.
55. Bottoli F., Winther G., Christiansen T., and Somers L. (2015). Influence of Plastic Deformation on Low-Temperature Surface Hardening of Austenitic Stainless Steel by Gaseous Nitriding. Metallurgical and Materials Transactions A, 46(6), 2579-2590.

56. Oganov A., Hemley R., Hazen R., and Jones A. (2013). Structure, Bonding, and Mineralogy of Carbon at Extreme Conditions. Carbon In Earth, 75(1), 47-77.
57. Ban M. (2012). Internal stress of hydrogenated diamond-like carbon films. In Diamond-Like Carbon Films (pp. 95-118). Nova Science.
58. Wang P., Wang X., Xu T., Liu W., Zhang J. "Comparing Internal Stress in Diamond-like Carbon Films with Different Structure." Thin Solid Films 515, no. 17 (2007): 6899-903.
59. Schwander M., Partes K. "A Review of Diamond Synthesis by CVD Processes." Diamond & Related Materials 20, no. 9 (2011): 1287-301.
60. Robertson J. (1996). Amorphous carbon. Current Opinion in Solid State and Materials Science, 1(4), 557-561.
61. Stolarski T.A. (2003). Modern Tribology Handbook: Vol. 1-Principles of Tribology, Vol. 2- Materials, Coating, and Industrial Applications, Editor-in-Chief: Bharat Bhushan, CRC Press 2001. Tribology International. 36. 559–560. 10.1016/S0301-679X(02)00259-1.
62. Robertson J. (1998), Deposition mechanism of diamond-like carbon, in Amorphous Carbon: State of the Art, Silva, S.R.P., Robertson, J., Milne, W.I., and Amaratunga, G.A.J. (Eds.), World Scientific Publishing, Singapore, 32-45.
63. Robertson J. (1992). Mechanical properties and coordinations of amorphous carbons. Physical Review Letters, 68(2), 220-223.
64. Koidl P., Ch. Wild, B. Dischler, J. Wagner, and M. Ramsteiner. "Plasma Deposition, Properties and Structure of Amorphous Hydrogenated Carbon Films." Materials Science Forum 52-53 (1991): 41-70.
65. Robertson J. (1994). The deposition mechanism of diamond-like a-C and a-C: H. Diamond and Related Materials, 3(4), 361-368.
66. Lifshitz Y. (1999). Diamond-like carbon — present status. Diamond and Related Materials, 8(8 9), 1659–1676. doi:10.1016/S0925-9635(99)00087-4
67. Robertson J. (2005). Mechanism of sp3 bond formation in the growth of diamond-like carbon. Diamond and Related Materials, 14, 942–948. doi:10.1016/j.diamond.2004.11.028
68. Wei C., Wang Y.S., Tai F.C. "The Role of Metal Interlayer on Thermal Stress, Film Structure, Wettability and Hydrogen Content for Diamond like Carbon Films on Different Substrate." Diamond & Related Materials 18, no. 2 (2009): 407-12.

69. Pauleau Y. (2008). Residual stresses in DLC films and adhesion to various substrates. In Tribology of Diamond-Like Carbon Films: Fundamentals and Applications (pp. 102-136). Springer US.
70. D R McKenzie. (1996). Tetrahedral bonding in amorphous carbon. Reports on Progress in Physics, 59(12), 1611-1664.
71. Neto V.F., Vaz R., Oliveira M.S.A., Grácio J. "CVD Diamond-coated Steel Inserts for Thermoplastic Mould Tools—Characterization and Preliminary Performance Evaluation." Journal of Materials Processing Tech. 209, no. 2 (2009): 1085-091.
72. Borges C.F.M., Pfender E., Heberlein J. "Influence of Nitrided and Carbonitrided Interlayers on Enhanced Nucleation of Diamond on Stainless Steel 304." Diamond & Related Materials 10, no. 11 (2001): 1983-990.
73. Voevodin A., S. Walck, and J. Zabinski. "Architecture of Multilayer Nanocomposite Coatings with Super-hard Diamond-like Carbon Layers for Wear Protection at High Contact Loads." Wear 203-204 (1997): 516-27.
74. Statuti R.P.C.C., Radi P.A., Santos L.V., Trava-Airoldi V.J. "A Tribological Study of the Hybrid Lubrication of DLC Films with Oil and Water." Wear 267, no. 5 (2009): 1208-213.
75. Boromei I., Ceschini L., Marconi A. and Martini C. A duplex treatment to improve the sliding behavior of AISI 316L: Low-temperature carburizing with a DLC (a-C: H) topcoat. Wear. 2013;302(12):899 908. doi:10.1016/j.wear.2013.01.086.
76. Dalibón E.L., Heim D., Forsich C., Rosenkranz A., Agustina G.M., Brühl S.P. "Characterization of Thick and Soft DLC Coatings Deposited on Plasma Nitrided Austenitic Stainless Steel." Diamond & Related Materials 59, no. C (2015): 73-79.
77. Morshed M.M., Mcnamara B.P., Cameron D.C., Hashmi M.S.J. "Stress and Adhesion in DLC Coatings on 316L Stainless Steel Deposited by a Neutral Beam Source." Journal of Materials Processing Tech. 143, no. 1 (2003): 922-26.
78. Chen K.W., Lin J.F. "The Study of Adhesion and Nanomechanical Properties of DLC Films Deposited on Tool Steels." Thin Solid Films 517, no. 17 (2009): 4916-920.
79. Butter R., Allen M., Chandra L., Lettington A.H., Rushton N. (1995). In vitro studies of DLC coatings with silicon intermediate layer. Diamond & Related Materials, 4(5), 857-861.

80. Ronkainen H., S. Varjus and K. Holmberg, Tribological performance of different DLC coatings in water-lubricated conditions. Wear, 2001. 249(3-4): p. 267-271.
81. Gilmore R. and R. Hauert, Comparitive study of the tribological moisture sensitivity of Si-free and Si-containing diamond-lie carbon films. Surface & Coatings Technology, 2000. 133-134: p. 437-442.
82. Tallion T.E., On competing failure modes in rolling contact. ASLE Trans., 1967. 10: p. 418-439.
83. Podgornik B., D. Hren, J. Vižintin, S. Jacobson, N. Stavlid, and Hogmark. "Combination of DLC Coatings and EP Additives for Improved Tribological Behaviour of Boundary Lubricated Surfaces." Wear 261, no. 1 (2006): 32-40.
84. Holleck H. (1986). Material selection for hard coatings. Journal of Vacuum Science and Technology A: Vacuum, Surfaces and Films, 4(6), 2661-2669.
85. Milosev I., B. Navinsek and Hh Strehblow, Corrosion Properties of Hard PVD Nitride Coatings (with the Emphasis on TN), ScientiJic Se&s of the International &lrealc, Vol. 37, Forschungszentrum Jtilich, 1995, p. 1.
86. Martin K., Madan A., Hoffman D., Ji J., and Barnett S. (2005). Mechanical properties and thermal stability of TiN/TiB2 nanolayered thin films. Journal of Vacuum Science & Technology A: Vacuum, Surfaces, and Films, 23(1), 90-98.
87. Wang D., Oki T.(1990). The morphology and orientation of Cr_xN films deposited by reactive ion plating. Thin Solid Films, 185(2), 219-230.
88. Swadźba L., Maciejny A., Formanek B., Liberski P., Podolski P., Mendala B., Gabriel H., Poznańska A. "Influence of Coatings Obtained by PVD on the Properties of Aircraft Compressor Blades." Surface & Coatings Technology 78, no. 1 (1996): 137-43.
89. Panjan P., Navinšek B., Cvelbar A., Zalar A., Milošev I. "Oxidation of TiN, ZrN, TiZrN, CrN, TiCrN and TiN/CrN Multilayer Hard Coatings Reactively Sputtered at Low Temperature." Thin Solid Films 281, no. 1-2 (1996): 298-301.
90. Milosev I. and Navinsek B. (1993). The effect of postdeposition heat-treatment on reactively sputtered CrN[sub x] and Cr(N, O) coatings. Journal of the Electrochemical Society, 140(3), L30-L32.

91. Hones P., Sanjines R., Lévy F. Characterization of sputter-deposited chromium nitride thin films for hard coatings. Surf Coatings Technol. 1997;94-95:398-402. doi:10.1016/S0257-8972(97)00443-X
92. Kirchlechner C., Martinschitz K.J., Daniel R., Mitterer C., Keckes J.. "Residual Stresses in Thermally Cycled CrN Coatings on Steel." Thin Solid Films 517, no. 3 (2008): 1167-171.
93. Schell N., Petersen J.H., Bøttiger J., Mücklich A., Chevallier J., Andreasen K.P., Eichhorn F.. "On the Development of Texture during Growth of Magnetron-sputtered CrN." Thin Solid Films 426, no. 1 (2003): 100-10.
94. Mei H.J., Zhao S.S., Chen W., Wang Q.M., Liang H.F. "Microstructure and Residual Stress of TiN Films Deposited at Low Temperature by Arc Ion Plating." Transactions of Nonferrous Metals Society of China 28, no. 7 (2018): 1368-376.
95. Conde A., Navas C., Cristóbal A.B., Housden J., de Damborenea J.. "Characterisation of Corrosion and Wear Behaviour of Nanoscaled E-beam PVD CrN Coatings." Surface & Coatings Technology 201, no. 6 (2006): 2690-695.
96. Fu Y., Zhu X., Tang B., Hu X., He J., Xu K., Batchelor A.W.. "Development and Characterization of CrN Films by Ion Beam Enhanced Deposition for Improved Wear Resistance." Wear 217, no. 2 (1998): 159-66.
97. Wei G., Rar A., and Barnard J. (2001). Composition, structure, and nanomechanical properties of DC-sputtered CrNx (0 <= x <= 1) thin films. Thin Solid Films, 398, 460-464.
98. Shah H. N., Jayaganthan R., Kaur D., and Chandra R. (2010). Influence of sputtering parameters and nitrogen on the microstructure of chromium nitride thin films deposited on steel substrate by direct-current reactive magnetron sputtering. Thin Solid Films, 518(20), 5762-5768. doi:10.1016/j.tsf.2010.05.095
99. Kong Q., Ji L., Li H., Liu X., Wang Y., Chen J., Zhou H. "Composition, Microstructure, and Properties of CrN X Films Deposited Using Medium Frequency Magnetron Sputtering." Applied Surface Science 257, no. 6 (2011): 2269-274.
100. Xu J., Umehara H., Kojima I. Effect of deposition parameters on composition, structures, density and topography of CrN films deposited by r.f. magnetron sputtering. Appl Surf Sci. 2002;201(1-4):208-218. doi:10.1016/S0169-4332(02)00942-X

101. Tan S., Zhang X., Wu X., Fang F., Jiang J. Comparison of chromium nitride coatings deposited by DC and RF magnetron sputtering. Thin Solid Films. 2011;519(7):2116-2120. doi:10.1016/j.tsf.2010.10.067
102. S. Swann. "Magnetron Sputtering." Physics in Technology 19, no. 2 (1988): 67-75.
103. Braeuer G., Szyszka B., Vergoehl M., Bandorf R. "Magnetron Sputtering – Milestones of 30 Years." Vacuum 84, no. 12 (2010): 1354-359.
104. Alfonso E., Olaya J., Cubillos G. Thin Film Growth Through Sputtering Technique and Its Applications. 2011.
105. Movchan B.A., and Demchishin Av. (1969). Study of the structure and properties of thick vacuum condensates of nickel, titanium, tungsten, aluminum oxide and zirconium dioxide. Fiz Metallov I Metalloved, 28(4), 653-660.
106. Thornton J., Influence of apparatus geometry and deposition conditions on the structure and topography of thick sputtered coating, J. Vac. Sci. Technol., Vol. 11, (1974) 666-670.
107. Greene J.E. Nucleation, Film Growth, and Microstructural Evolution, Deposition Processes for Films and Coating, 2nd edition, (R. Bunshah,ed.), Ch. 13, Noyes Publications (1994).
108. Goldfarb I., Pelleg J., Zevin L., and Croitoru N. (1991). Lattice distortion in thin films of IVB metal (Ti, Zr, Hr) nitrides. Thin Solid Films, 200(1), 117-127.
109. Petrov I., Barna P., Hultman L., Greene J. Microstructural evolution during film growth. J. Vac. Sci. Technol. A, Vol 21, No 5, (September 2003), 117-128.
110. Karabacak T. Thin-film growth dynamics with shadowing and re-emission effects. doi:10.1117/1.3543822
111. Roy R. A., and R. Messier. "Evolutionary Growth Development in SiC Sputtered Films." MRS Proceedings 38 (1984): MRS Proceedings, 1/1984, Vol.38.
112. Roy R. A., and R. Messier. “Quantitative analysis of thin-film morphology evolution,” in High Performance Ceramic Films and Coatings, P. Vincenzini, Ed., Elsevier, Amsterdam, Netherlands (1991).
113. Karabacak T., Y. Zhao, G. Wang, and Lu. "Growth-front Roughening in Amorphous Silicon Films by Sputtering." Physical Review B - Condensed Matter and Materials Physics 64, no. 8 (2001): .

114. Karabacak T., Y. Zhao, G. Wang, and T. Lu. "Growth Front Roughening in Silicon Nitride Films by Plasma-enhanced Chemical Vapor Deposition." Physical Review B 66, no. 7 (2002): 753291-7532910.
115. Hamaguchi S., Rossnagel S.M.. "Simulations of Trench-filling Profiles under Ionized Magnetron Sputter Metal Deposition." Journal of Vacuum Science and Technology B: Microelectronics and Nanometer Structures 13, no. 2 (1995): 183-91.
116. Hamaguchi S., and S.M. Rossnagel. "Liner Conformality in Ionized Magnetron Sputter Metal Deposition Processes." Journal Of Vacuum Science & Technology B 14, no. 4 (1996): 2603-608.
117. Karabacak T., H. Guclu, and M. Yuksel. "Network Behavior in Thin Film Growth Dynamics." Physical Review B 79, no. 19 (2009): .
118. Sánchez-López J.C., Fernández A.. "Doping and Alloying Effects on DLC Coatings." In Tribology of Diamond-Like Carbon Films: Fundamentals and Applications, 311-28. Springer US, 2008.
119. Hauert R., Glisenti A., Metin S., Goitia J., Kaufman J.H., van Loosdrecht P.H.M., Kellock A.J., Hoffmann P., White R.L., Hermsmeier B.D. "Influence of Nitrogen Doping on Different Properties of A-C:H." Thin Solid Films 268, no. 1 (1995): 22-29.
120. Liu A.Y., and M.L. Cohen. "Structural Properties and Electronic Structure of Low-compressibility Materials:. Beta. -Si Sub 3 N Sub 4 and Hypothetical. Beta. -C Sub 3 N Sub 4." Physical Review, B: Condensed Matter 41, no. 15 (1990): 10727-10734.
121. Hellgren N., M. Johansson, E. Broitman, L. Hultman, and J. Sundgren. "Role of Nitrogen in the Formation of Hard and Elastic (formula Presented) Thin Films by Reactive Magnetron Sputtering." Physical Review B - Condensed Matter and Materials Physics 59, no. 7 (1999): 5162-169.
122. Pauleau Y. "Residual Stresses in DLC Films and Adhesion to Various Substrates." In Tribology of Diamond-Like Carbon Films: Fundamentals and Applications, 102-36. Springer US, 2008.
123. Bilek M.M.M., Mckenzie D.R.. "A Comprehensive Model of Stress Generation and Relief Processes in Thin Films Deposited with Energetic Ions." Surface & Coatings Technology 200, no. 14-15 (2006): 4345-354.

124. Ray S.C., Pong W.F., Papakonstantinou P.. "Iron, Nitrogen and Silicon Doped Diamond like Carbon (DLC) Thin Films: A Comparative Study." Thin Solid Films 610, no. C (2016): 42-47.
125. Angus J.C., Jansen F.. "Dense “diamondlike” Hydrocarbons as Random Covalent Networks." Journal of Vacuum Science and Technology A: Vacuum, Surfaces and Films 6, no. 3 (1988): 1778-782.
126. Kaufmann E.. Characterization of Materials. Hoboken, NJ: John Wiley and Sons, 2003.
127. John R. Ferraro 1918- Kazuo Nakamoto 1922-, Chris W Brown, ScienceDirect (Online service), Elsevier. Introductory Raman Spectroscopy. 2nd ed. Amsterdam ; Boston: Academic Press, 2003.
128. Wang S., Zhu J., Wang J., Yin X., Han X.. "Raman Spectroscopy and Mechanical Properties of Multilayer Tetrahedral Amorphous Carbon Films." Thin Solid Films 519, no. 15 (2011): 4906-909.
129. Zou Y.S., Wang Q.M., Du H., Song G.H., Xiao J.Q., Gong J., Sun C., Wen L.S.. "Structural Characterization of Nitrogen Doped Diamond-like Carbon Films Deposited by Arc Ion Plating." Applied Surface Science 241, no. 3-4 (2005): 295-302.
130. Grill A. "Tribology of Diamondlike Carbon and Related Materials: An Updated Review." Surface & Coatings Technology 94, no. 1-3 (1997): 507-13.
131. Tamor M.A., and W.C. Vassell. "RAMAN FINGERPRINTING OF AMORPHOUS-CARBON FILMS." Journal Of Applied Physics 76, no. 6 (1994): 3823-830.
132. Dutta P. "Grazing Incidence X-ray Diffraction." Current Science 78, no. 12 (2000): 1478-483.
133. Anon 1986. Metals handbook, ninth edition, volume 10—materials characterization: (American Society for Metals, Metals Park, OH.,1986), 760 pages, $92.00. Metallography, 19(4), pp.483–484.
134. DeVries JE. Surface characterization methods— XPS,TOF-SIMS, and SAM a complimentary ensemble of tools. J Mater Eng Perform. 1998;7(3):303-311. doi:10.1361/105994998770347729
135. Ferrari A. "Determination of Bonding in Diamond-like Carbon by Raman Spectroscopy." Diamond and Related Materials 11.3-6 (2002): 1053-061. Web.

136. Schwan J., Ulrich S., Batori V., Ehrhardt H., Silva S. R. P. "Raman Spectroscopy on Amorphous Carbon Films." Journal of Applied Physics 80.1 (1996): 440-47. Web.

137. Oliver W.C. "An Improved Technique for Determining Hardness and Elastic Modulus Using Load and Displacement Sensing Indentation Experiments." Journal of Materials Research 7.6 (1992): 1564-1583. Web.

138. Knapp J.A., D.M. Follstaedt, S.M. Myers, J.C. Barbour, and T.A. Friedmann. "Finite-element Modeling of Nanoindentation." Journal of Applied Physics 85.3 (1999): 1460-474. Web.

139. Weiler M., Sattel S., Giessen T., Jung K., Ehrhardt H., Veerasamy V. S., and Robertson J. (1996). Preparation and properties of highly tetrahedral hydrogenated amorphous carbon. Physical Review B, 53(3), 1594-1608. doi:10.1103/physrevb.53.1594

140. Quinn G. D., Gettings R. K., and Ives L. (2004). A standard reference material for vickers hardness of ceramics and Hardmetals. IMEKO TC5 Conference on Hardness Measurements Theory and Application in Laboratories and Industries, HARDMEKO 2004, 90-97.

141. Verein-Deutscher-Ingenieure, “Daimler Benz Adhesion Test, VDI 3198.” VDI-Verlag, Dusseldorf, p. 7, 1992.

142. Heinke W., Leyland A., Matthews A., Berg G., Friedrich C., Broszeit E.. "Evaluation of PVD Nitride Coatings, Using Impact, Scratch and Rockwell-C Adhesion Tests." Thin Solid Films 270.1 (1995): 431-38. Web.

143. Vidakis N., Antoniadis A., Bilalis N. The VDI 3198 indentation test evaluation of a reliable qualitative control for layered compounds. 2003;144:481-485. doi:10.1016/S0924 0136(03)00300-5

144. Kato K., Adachi K. Wear Mechanisms. Mod Tribol Handbook Vol 1. 2001:28. doi:10.1201/9780849377877.ch7

145. Tan S., Zhang X., Wu X., Fang F., Jiang J. Comparison of chromium nitride coatings deposited by DC and RF magnetron sputtering. Thin Solid Films. 2011;519(7):2116-2120. doi:10.1016/j.tsf.2010.10.067

146. Elangovan T., Kuppusami P., Thirumurugesan R., Ganesan V., Mohandas E., Mangalaraj D. Nanostructured CrN thin films prepared by reactive pulsed DC magnetron sputtering.

Mater Sci Eng B Solid-State Mater Adv Technol. 2010;167(1):17-25. doi:10.1016/j.mseb.2010.01.021

147. Lippitz A., Hübert T. XPS investigations of chromium nitride thin films. Surf Coatings Technol. 2005;200(1-4 SPEC. ISS.):250-253. doi:10.1016/j.surfcoat.2005.02.091

148. Leyland A. and Matthews A. "On the Significance of the H/ E Ratio in Wear Control: A Nanocomposite Coating Approach to Optimised Tribological Behaviour." Wear 246.1 (2000): 1-11. Web.

149. Cunha L., Andritschky M.. "Residual Stress, Surface Defects and Corrosion Resistance of CrN Hard Coatings 1 Presented at the ICAM '97/EMRS '97 Conference (Symposium K), Strasbourg, France, June 1997. 1." Surface & Coatings Technology 111.2 (1999): 158-62. Web.

150. Shah H. N., R. Jayaganthan, and D. Kaur. "Effect of Sputtering Pressure and Temperature on DC Magnetron Sputtered CrN Films." Surface Engineering 26.8 (2010): 629-37. Web.

151. Samano E.C., Soto G., Olivas A., Cota L. DLC thin films characterized by AES, XPS and EELS. Appl Surf Sci. 2002;202(1-2):1-7. doi:10.1016/S0169-4332(02)00891-7

152. Paik N. Raman and XPS studies of DLC films prepared by a magnetron sputter-type negative ion source. Surf Coatings Technol. 2005;200(7):2170-2174. doi:10.1016/j.surfcoat.2004.08.073

153. Jiang. (1991). Rayleigh mode in amorphous hydrogenated carbon films. Physical Review. B, Condensed Matter, 43(3), 2372-2377.

154. Mosaner P., Bonelli M., and Miotello A. (2003). Pulsed laser deposition of diamond-like carbon films: Reducing internal stress by thermal annealing. Applied Surface Science, 208-209, 561-565. doi:10.1016/s0169-4332(02)01383-1.

155. Li Z., Guan X., Wang Y., Li J., Cheng X., Lu X., Wang L., Xue Q. "Comparative Study on the Load Carrying Capacities of DLC, GLC and CrN Coatings under Sliding-friction Condition in Different Environments." Surface & Coatings Technology 321 (2017): 350-57. Web.

156. Brundle C.R., Charles A., Evans J, Shaun W. Encyclopedia of Materials Characterization. J Chem Inf Model. 2013;53(9):782. doi:10.1017/CBO9781107415324.004

157. Wang Z., Zhou W., ProQuest, ProQuest Ebook Central, & MyiLibrary. (2007). Scanning microscopy for nanotechnology : Techniques and applications (Springer ebooks). New York: Springer

158. Srinivasan S., Tang Y., Li Y.S., Yang Q., Hirose A. "Ion Beam Deposition of DLC and Nitrogen Doped DLC Thin Films for Enhanced Haemocompatibility on PTFE." Applied Surface Science 258, no. 20 (2012): 8094-099.

159. Müller F. A., Müller L., Hofmann I., Greil P., Wenzel M. M., and Staudenmaier R. (2006). Cellulose-based scaffold materials for cartilage tissue engineering. Biomaterials, 27(21), 3955-3963. doi:10.1016/j.biomaterials.2006.02.031

160. Resel R., Bainschab M., Pichler A., Dingemans T., Simbrunner C., Stangl J., and Salzmann I. (2016). Multiple scattering in grazing-incidence X-ray diffraction: Impact on lattice-constant determination in thin films. Journal of Synchrotron Radiation, 23(3), 729-734. doi:10.1107/s1600577516003672